

Image based characterization and geometric modeling of 3d materials microstructures

Vom Fachbereich Mathematik
der Technische Universität Kaiserslautern
zur Verleihung des akademischen Grades
Doktor der Naturwissenschaften
(Doctor rerum naturalium, Dr. rer. nat.)
genehmigte Dissertation von

Irene Vecchio

Gutachter:
Juniorprof. Dr. Claudia Redenbach
Prof. Dr. Dominique Jeulin

Disputation: 7. Juli 2014

D386

Acknowledgments

I am grateful to the Image Processing Department in the Fraunhofer ITWM and the Technische Universität Kaiserslautern for the fundings. Moreover, I'd like to acknowledge the support from the Deutsch-Französische Hochschule (DFH).

I would like to thank Markus J. Heneka from RJL Micro & Analytic for proposing the project on geometric characterization for technical cleanliness, projects KF 227 4801 RR9 and KF 228 2001 RR9 ParSiDi-3D. They were a cooperation between the Image Processing department of Fraunhofer ITWM and RJL Micro&Analytic, funded by the German Federal Ministry of Economics and Technology.

For the sample analyzed in Chapter 3, I acknowledge the AiF-Forschungsvorhaben IGF-Vorhaben-Nr. IGF 17644 N “Simulationsgestützte Entwicklung von mitteldichten Faserplatten für den Leichtbau (MDF-Simulation)”. CT scan by Frank Sieker, GE phoenix|x-ray, Wunstorf.

I acknowledge support from the German Federal Ministry of Economics and Technology via the German Federation of Industrial Research Associations, with the project number 16912 N “MAFoam”. Moreover, I'd like to thank Ralf Schlimper from Fraunhofer IWM, Halle, for the assistance with the analysis of foams.

Preface

I would like to thank

...doubtlessly at first place, Claudia Redenbach and Katja Schladitz for their constant support and guidance, and especially for all they taught me. Not only I had the chance to work on particularly interesting topics, but I also could take a closer look both into research and industrial projects. I am very grateful for the several opportunities to present my work in international conferences and workshops, where I felt part of the lively Stochastic Geometry community. I am grateful to Claudia for accepting me for an internship at the very beginning of this experience.

...Andy Kraynik for a few very motivating talks, for the precious advice, and for the readiness to comment on my questions, even from the other side of the ocean. Thank for introducing me to the Surface Evolver and helping me with some technical problems.

...the Image Processing Department in Fraunhofer ITWM and all the people, present and past, who made it a very pleasant experience to work here. It has been truly motivating to have been part of the Microstructure Group. I am particularly indebted to Oliver Wirjadi, Björn Wagner and especially to Michael Godehardt for the technical support.

...Heiko Andrä, Matthias Kabel, and Inga Shklyar for the assistance and for sharing their expertise with me.

...Joachim Ohser and Jürgen Kampf for some very stimulating discussions.

...AG Statistik at the TU Kaiserslautern, where I always found a very friendly atmosphere, thanks to everybody!

...all the extraordinary people I met in these years, many of which have something to do with the Institute. Thanks to all my office-mates, especially to Torben Prill with whom I shared some of the ups and downs of the PhD life. And also a special thanks to the co-organizers of nice evenings in and outside the institute with movies and Doktorandenstammtisch.

...my family for the continuous support, especially Marta, my mom, and my grandparents for being so understanding and always available when I need them. A special thank to Oliver, above all for always bringing back my good mood.

Contents

Introduction	1
1 Foundations	5
1.1 Image analysis	6
1.2 Stochastic geometry	7
1.2.1 Intrinsic volumes	8
1.2.2 Random closed sets	11
1.2.3 Point processes	14
2 Characterization of 3d objects	17
2.1 Object characterization	19
2.1.1 Basic measures	19
2.1.2 Isoperimetric shape factors	20
2.1.3 Convex hull features	21
2.1.4 Further size characterization	24
2.2 Analysis of the estimation error	28
2.3 Classification	30
2.4 Application to technical cleanliness	33
2.5 Discussion	37
3 Models for fiber systems	39
3.1 Orientation distribution	41
3.2 Models without interaction	42
3.2.1 Boolean model	42
3.2.2 Poisson cylinder process	45
3.3 Models with interaction	52
3.3.1 Random sequential adsorption (RSA)	52
3.3.2 Fiber packing	54
3.3.3 Sedimentation	56
3.4 Application to cellulose fiber systems	57
3.4.1 Model fitting and validation	58
3.5 Discussion	62
4 Models for foams	63
4.1 Random tessellations	64
4.1.1 Geometric characterization	65

4.2	Tessellation models	67
4.2.1	Voronoi tessellations	68
4.2.2	Laguerre tessellations	69
4.3	Model fitting for foams	71
4.3.1	Angles in Laguerre tessellations	73
4.3.2	Estimation of angles from images	77
4.3.3	Application to closed cell foams	85
4.4	Edge length distribution	90
4.4.1	Surface Evolver and relaxation	90
4.4.2	Analysis of solid foams	91
4.5	Discussion	97
	Conclusions	99
	List of symbols	101
A	Coefficients for angles in random Laguerre tessellations	103
B	Curriculum Vitae	105
	Bibliography	107

Introduction

It is well known that the structure at a microscopic scale strongly influences the macroscopic properties of materials. Moreover, the advancement in imaging technologies allows to capture the complexity of the structures at always decreasing scales. Therefore, more sophisticated image analysis techniques are needed. This thesis provides tools to facilitate the extraction of geometric features from images and the processing of the information with applications to industrial production and to materials science. We consider different types of three-dimensional structures: particles, fiber systems, and foams. We enhance methods to geometrically characterize these structures starting from three-dimensional images acquired with micro-computed tomography (μ CT). Moreover, we investigate which characteristics are sufficient and necessary to infer the desired information. In the analysis of particles, this consists in defining a collection of parameters to describe their size and shape. Just a few features are sufficient to yield the classification of particles required by the standards of technical cleanliness. Concerning the application to materials science, we aim at fitting stochastic models to the microstructures of materials. In particular, we develop techniques to broaden the possibilities of model fitting without user interaction, while enriching the features embedded in the models.

Chapter 2 deals with the problem of technical cleanliness in automotive industry. Safety and efficiency of assembled products can be reduced by the occurrence of residual dirt particles in single components. The damage that dirt particles can cause depends on their shape, size, and material composition. Therefore, a complete geometric description of the particles serves to evaluate how dangerous they are. International agreed standards provide rules for the analysis of samples of particles based on two-dimensional images. However, nowadays, it is possible to acquire images of the whole three-dimensional structures even with desktop devices. Therefore, also the characterization needs to be extended to 3d. Each particle is a connected compact set of which we observe a discrete representation in a binary three-dimensional image. Our contribution is the definition of a collection of unambiguous parameters that exhaustively describe three-dimensional shapes and can be efficiently estimated from the images. The parameters are obtained combining methods of classical geometry, mathematical morphology and integral geometry. In particular, we describe the size of an object via the length of the edges of the minimum volume bounding box, that is, the cuboid with arbitrary orientation and minimum volume bounding the object. This is the natural generalization of length and width based on two-dimensional images defined in the current norms. We propose an optimized algorithm based on the results of Barequet and Har-Peled (2001). An analysis of the estimation error due to discretization is provided for all characteristics. Moreover, the standards of technical cleanliness require to classify the particles into fibers and granules. The classification is performed by looking at microscopic images. Thus, it is left to the user to infer the class of a particle. We aim at generalizing the

definitions of the classes in the three-dimensional context and at providing objective rules for the classification based on the features estimated from the images. From the wide set of features defined, we show that only a few suffice to classify an object. Depending on the size of the particles, we suggest to base the classification either on the size of the minimum volume bounding box or on the isoperimetric shape factors. In both cases, the classification for technical cleanliness can be obtained automatically.

Afterwards, we focus on materials science (Chapters 3-4). Different approaches can be taken to investigate how the physical properties of materials are influenced by the geometry of their microstructure. One method consists in producing materials with different geometry at the microscale and then analyzing their physical properties. Another way is to proceed analogously, but *virtually*. The geometry of the microstructures is embedded in a model that has statistically the same characteristics. Simulations of the physical properties on the model and on its variations improve the understanding of how geometry and physics are related. Furthermore, this process allows to determine the geometric characteristics yielding the desired properties in the materials. Thus, new materials are produced according to the ideal geometry found through simulations only (*virtual material design*).

Even in high resolution images of materials' microstructures, segmentation of the components of interest is not a trivial task. For instance, in case of fiber systems, it is often impossible to separate the single fibers. Therefore, we cannot apply the same straightforward methods for geometric characterization employed for the application to technical cleanliness. Instead, one can only estimate either geometric features based on local information or consider characteristics of the system as a whole. Naturally, the choice of the model is also influenced by the amount of information that can be extracted from the images. The more sophisticated the model, the wider is the set of characteristics that need to be estimated from the image data.

Fitting a stochastic model to a sample means to find the parameters of the model that feature statistically the same geometric characteristics as those observed in the sample. Ideally, the parameters of a model are related to its geometric characteristics by analytical formulae. However, this is rarely the case and the selection of the parameters needs to be based on multiple realizations. The features of the realizations are compared with those of the sample and the set of parameters generating the best fit is chosen. Of course, this approach is time consuming and requires expert user interaction. Therefore, we examine which factors mainly influence the validity of analytical relations between the parameters and the characteristics of the model. When these rules are not available, we investigate alternative strategies to allow automatic model fitting.

When considering fiber systems (Chapter 3), classic models of cylinders, such as the Boolean model and the Poisson process of dilated lines, benefit from a complete analytical description. For isotropic fiber systems, the Miles' formulae relate the intrinsic volume densities of the union of fibers to the mean characteristics of the cylinders and to the intensity of the process. Thus, theoretically, estimating only four characteristics of the union of fibers from an image allows to deduce the parameters of the model. Nevertheless, to optimize mechanical properties of composites or simply due to the production process, we often observe anisotropic fiber orientations. We investigate this case in details, especially for Poisson processes of dilated lines. We extend the results of Spiess and Spodarev (2010) in order to have direct model fitting for polygonal cross sections. This method is applied to model a sample of medium density fiber board. Its microstructure is characterized by high

density packing of fibers with squared cross section typically lying in a plane. As fibers are only a few pixels thick, it is not possible to estimate fine characteristics of the single fibers. Nevertheless, estimating the intrinsic volume densities is sufficient to fit Boolean models and Poisson processes of cylinders with circular or squared cross sections. We observe that with this coarse resolution, the different cross sections cause only small differences in the quantitative analysis of the realizations.

Different problems arise when dealing with foams. We focus on characterizing and modeling the geometry of the pore system. Motivated by the literature (see Chapter 4), the model of choice is random Laguerre tessellation. Pores or cells are modeled as convex polytopes such that each facet is shared by two cells, each edge by three cells, and each vertex by four cells. This property, called *normality*, is physically motivated and at the same time it allows to reduce the number of parameters needed to describe the whole geometry of the tessellation. To gain control of the volume distribution, we consider tessellations generated by systems of non-overlapping spheres. However, this yields the loss of a full analytical description of the model. Nevertheless, automatic model fitting can still be obtained by approximating the characteristics of the tessellation depending on the parameters of the model (Redenbach, 2009). The first question we investigate is whether the model fitting procedure can be improved while still allowing the automatic selection of the model parameters. Angles between facets and between edges show low correlation with the features employed so far for model fitting, that is, moments of volume, surface area, mean width, and number of facets per cell. We show that the distributions of angles in Laguerre tessellations depend on the model parameters. Thus, automatic model fitting can include also this information. Moreover, we propose an algorithm to estimate angles from images of real foams. Considering samples of closed cell polymer foams, it turns out that angles in random Laguerre tessellations fit well to the samples even when not employed in the choice of the model parameters. Secondly, we concentrate on the edge length distribution. In Laguerre tessellations many more short edges than in real foams occur. To deal with this problem, the rich literature on models for soap froth suggests to consider *relaxed* models, see for instance Kraynik et al. (2003). Relaxation refers to topological and structural modifications of a given tessellation in order to make it comply with Plateau's laws of mechanical equilibrium. We consider samples of different types of foams, closed and open cell foams, polymeric and metallic. To each sample, we fit a random Laguerre tessellation and then relax some realizations. Then, we compare the geometric characteristics of the model and of the relaxed tessellations. Whether the relaxation improves the edge length distribution depends on the type and on the regularity of the foam.

Parts of this work are published in the following articles and conference proceedings:

- Irene Vecchio, Katja Schladitz, Michael Godehardt, Markus J. Heneka. Geometric characterization of particles in 3d with an application to technical cleanliness. *Bericht des Fraunhofer ITWM*, Nr. 207, 2011.
- Irene Vecchio, Katja Schladitz, Michael Godehardt, Markus J. Heneka. 3D geometric characterization of particle applied to technical cleanliness, *Image Analysis & Stereology*, 32(3), 2012.
- Irene Vecchio, Claudia Redenbach, Katja Schladitz. Fitting Laguerre Tessellations

to the Microstructure of Cellular Materials. In *1st International Conference on 3D Materials Science*, John Wiley & Sons, 2012.

- Irene Vecchio, Katja Schladitz, Claudia Redenbach. Laguerre tessellations: fitting a model to rigid closed-cell polymer foams. In *Proceedings Cellular Materials*, Deutsche Gesellschaft für Materialkunde, 2012.
- Irene Vecchio. Stochastic models in materials science. In *2nd Young Researcher Symposium (YRS)*, Fraunhofer Verlag, 2013.
- Irene Vecchio, Claudia Redenbach, Katja Schladitz. Angles in Laguerre tessellation models for solid foams. *Computational Materials Science*, 83:171–184, 2014.

Chapter 1

Foundations

In this chapter, we introduce the notation and recall some definitions which are fundamental for our whole work. First, we remind the definitions of properties of sets in the d -dimensional Euclidean space and summarize the basic concepts of image processing (Section 1.1). Then, we introduce some notions of stochastic and integral geometry (Section 1.2).

- Let \mathbb{N} , \mathbb{Z} and \mathbb{R} denote the natural, integer and real numbers, respectively. \mathbb{R}^d is the d -dimensional Euclidean space.
- For X, Y subsets of \mathbb{R}^d , the *Minkowski sum* is defined as

$$X \oplus Y = \{x + y : x \in X, y \in Y\} = \bigcup_{y \in Y} (X + y).$$

The *Minkowski difference* is defined as

$$X \ominus Y = \{X^C \oplus Y\}^C = \bigcap_{y \in Y} (X + y),$$

where $X^C = \mathbb{R}^d \setminus X$ is the complement of X . Note that $X \ominus Y \neq X \oplus (-Y)$. Moreover, if Y is constituted by only one element, $Y = \{y\}$, then the Minkowski sum $X \oplus Y$ is equivalent to the translation $X + y$. In this case, the Minkowski difference corresponds to the translation $X - y$.

- A set $X \in \mathbb{R}^d$ is *bounded* if there exists a ball B_r with radius $r > 0$ such that $X \subset B_r$, it is *(topologically) open* if for each $x \in X$ there exists $\varepsilon > 0$ such that $x + B_\varepsilon \subset X$. The *interior* $\text{int}(X)$ of X is the largest topologically open set contained in X . The *(topological) closure* of X is $\bar{X} = (\text{int}(X^C))^C$. A set X is *(topologically) closed* if $X = \bar{X}$, it is *topologically regular* if $\bar{X} = \overline{\text{int}(X)}$ and $\text{int}(X) = \text{int}(\bar{X})$. A bounded and topologically closed set in \mathbb{R}^d is called *compact*.
- A set $X \in \mathbb{R}^d$ is called *morphologically open* if it exists $\varepsilon > 0$ such that $X = (X \ominus B_\varepsilon) \oplus B_\varepsilon$, *morphologically closed* if $X = (X \oplus B_\varepsilon) \ominus B_\varepsilon$. Furthermore, X is *morphologically regular* if it exists $\varepsilon > 0$ such that X is morphologically open and morphologically closed with respect to B_ε .

- For X, Y subsets of \mathbb{R}^d , the *dilation of X with Y* is

$$X \oplus \check{Y} = \{x - y : x \in X, y \in Y\},$$

where \check{Y} is the reflection of Y . The *erosion of X with Y* is

$$X \ominus \check{Y} = \{x \in \mathbb{R}^d : Y + x \subseteq X\}.$$

If Y is symmetric then dilation corresponds to the Minkowski sum and erosion to the Minkowski difference.

1.1 Image analysis

We now recall some basics of image analysis. More details are found in Ohser and Schladitz (2009, Chapter 3) or Redenbach et al. (2012a). A d -dimensional image can be seen as a d -dimensional array. Its elements are called *pixels*, although sometimes the term *voxel* is preferred when $d = 3$. The distances between the pixels define the underlying point lattice. Usually, images are defined on the *primitive cubic lattice* $\mathbb{L}^d = a\mathbb{Z}^d$, where $a > 0$ is the *lattice distance* or *spacing*. It is also possible to define a lattice with different spacing in each direction: $\mathbb{L}_D^d = D\mathbb{Z}^d$, where D is a diagonal d -dimensional matrix. In fact, some imaging techniques yield a different lattice distance in each axis direction. Moreover, this freedom can be useful in some applications. For instance, an anisotropic structure observed on \mathbb{L}^d can be made isotropic by a suitable choice of D .

In order to rigorously define properties of discrete sets on \mathbb{L}^d , it is necessary to specify the connectivity rules among the lattice points. These rules are yielded by the *adjacency system*. In two dimensions, this is completely determined by defining the neighborhood of a pixel. In 3d, however, a neighborhood alone does not suffice to yield a consistent adjacency system. The adjacency system has to be defined as a set of convex hulls yielded by $2 \times 2 \times 2$ pixel configurations. Moreover, it is important that the connectivity chosen for the foreground is consistent with that of the background. More details and suitable adjacency systems for background and foreground in three-dimensional images are illustrated in Ohser and Schladitz (2009).

Let W be a compact window in \mathbb{R}^d and $V \subset \mathbb{R}$. Then, a d -dimensional *image* I is the mapping

$$I : \mathbb{L}^d \cap W \rightarrow V.$$

If V is a set of only two elements, typically $V = \{0, 1\}$, then I is a *binary image*. Normally, 0 stands for black and represents the *background*, whereas 1 stands for white and represents the *foreground*, i. e., the component of interest in the image. If the pixels can take more than two values, we talk about *grey-value images*. Usually, V is a subset of \mathbb{N}_0 , but images with real values are also permitted.

Let us consider binary images. The foreground \tilde{X} can be easily interpreted as the discretization of a set $X \subset \mathbb{R}^d$: $\tilde{X} = X \cap \mathbb{L}^d \cap W$. Image analysis aims at extracting information on X based on \tilde{X} . A way to obtain this, is by investigating the intersections of \tilde{X} with a set Y , which is called the *structuring element*. This is the principle of *filters*. In general, filters can be used for smoothing, denoising, or extraction of features, e. g., edge detection.

Morphological operations were defined and widely treated by Serra (1969) and Matheron (1975). Dilation and erosion recalled above are two morphological operations that can be combined to reconstruct the set X . In fact, although in general Minkowski sum and subtraction are not reverse operations, in case X and Y are both compact and convex sets, it holds:

$$\begin{aligned}(X \ominus \check{Y}) \oplus Y &= X, \\ (X \oplus \check{Y}) \ominus Y &= X.\end{aligned}$$

Therefore, for arbitrary X and Y we define the *morphological opening* of X with the set Y as

$$X \circ Y = (X \ominus \check{Y}) \oplus Y,$$

whereas the *morphological closing* of X with the set Y is

$$X \bullet Y = (X \oplus \check{Y}) \ominus Y.$$

Heuristically, morphological opening “cleans” the image of small components of the foreground which do not belong to X . Morphological closing, conversely, fills up small holes in the foreground.

So far, we discussed operations on binary images. Nevertheless, filters and morphological operations can be defined also on grey-value images. Usually, they are applied in the preprocessing step in order to denoise and smooth the structure before binarization. Furthermore, it is sometimes convenient to work with grey-value images, as for instance obtained with microscopy or computer tomography, as they contain more information about the original structures than binary images do. For details see Ohser and Schladitz (2009, Chapter 4).

Further examples of feature extractions, image based characterization, reconstruction of structures will be given throughout this work.

1.2 Stochastic geometry

Throughout our work, we focus on characterizing three-dimensional objects and complex structures. Moreover, complex structures such as fiber systems or foams, can be seen as realizations of stochastic models. These models are strongly based on the concept of random closed sets. The key idea behind random sets is to generalize the concept of random variable to a set-valued map. In this section, we first introduce a basic set of characteristics to describe sets (not necessarily random). Then, we will rigorously define random closed sets (RACS) and the special case of point processes. Extensive treatments of random closed sets and stochastic geometry can be found, for instance, in Schneider and Weil (2008) and Stoyan et al. (1995). The first formalisms are due to Matheron (1975).

We recall that a σ -algebra in a topological space E is a non-empty collection of subsets of E such that it is closed with respect to complementarity and to countable unions. Consequently, it is also closed with respect to countable intersections, the empty set \emptyset and the whole set E also belong to the σ -algebra. The Borel σ -algebra of E , $\mathcal{B}(E)$ is the smallest σ -algebra containing all the open (or closed) subsets of E . We will sometimes use the notation \mathcal{B} for $\mathcal{B}(\mathbb{R}^d)$.

We denote the sets of all closed, open, and compact subsets of \mathbb{R}^d as \mathcal{F} , \mathcal{G} , and \mathcal{C} , respectively. Moreover, \mathcal{K} is the set of all compact convex subsets of \mathbb{R}^d and \mathcal{R} is the convex ring:

$$\mathcal{R} = \{X \subset \mathbb{R}^d : X = \bigcup_{i=0}^m K_i, K_i \in \mathcal{K}, m \in \mathbb{N}, m < \infty\}.$$

The extended convex ring \mathcal{S} contains all the sets $X \subset \mathbb{R}^d$ such that $X \cap K \in \mathcal{R}$ for all $K \in \mathcal{K}$. Benefiting from all the above properties, the empty set belongs to \mathcal{F} , \mathcal{G} , \mathcal{C} , \mathcal{K} , \mathcal{R} and \mathcal{S} . Moreover, it holds $\mathcal{K} \subset \mathcal{R} \subset \mathcal{S} \subset \mathcal{F}$ and $\mathcal{R} \subset \mathcal{C} \subset \mathcal{F}$, where all the inclusions are strict.

For $A \subset \mathbb{R}^d$, define the sets

$$\mathcal{F}^A = \{F \in \mathcal{F} : F \cap A = \emptyset\}, \quad \mathcal{F}_A = \{F \in \mathcal{F} : F \cap A \neq \emptyset\}.$$

Then \mathcal{F} can be equipped with the topology generated by

$$\{\mathcal{F}^C : C \in \mathcal{C}\} \cup \{\mathcal{F}_G : G \in \mathcal{G}\}$$

and by the Borel σ -algebra $\mathcal{B}(\mathcal{F})$ generated by either $\{\mathcal{F}_C : C \in \mathcal{C}\}$, $\{\mathcal{F}_G : G \in \mathcal{G}\}$, $\{\mathcal{F}^C : C \in \mathcal{C}\}$ or $\{\mathcal{F}^G : G \in \mathcal{G}\}$.

1.2.1 Intrinsic volumes

We begin by defining characteristics for compact convex sets and then extend the definition to sets in \mathcal{R} . The *intrinsic volumes* of a convex body K are defined starting from the volume of its parallel set at a distance $r \geq 0$:

$$K \oplus B_r = \{x + y : x \in K, y \in B_r\}$$

where B_r is the ball of radius r centered in the origin and \oplus is called Minkowski sum. The d -dimensional volume V_d of the parallel set can be expressed as a polynomial in r with coefficients depending only on K . This is stated in the following theorem (see Schneider (1993, Chapter 4) for the proof):

Theorem 1.2.1 (Steiner formula)

Let K be a convex non-empty body in \mathcal{K} . For $r \in \mathbb{R}$, $r \geq 0$, it holds:

$$V_d(K \oplus B_r) = \sum_{k=0}^d r^{d-k} \kappa_{d-k} V_k(K), \quad (1.1)$$

where κ_k is the volume of a k -dimensional unit ball and $V_k(K)$ for $k = 0, \dots, d$ are the intrinsic volumes of K .

An alternative formulation of the Steiner formula defines quantities proportional to the intrinsic volumes called *Minkowski functionals* or *quermassintegrals* W_j with $j = 0, \dots, d$

$$V_d(K \oplus B_r) = \sum_{j=0}^d r^j \binom{d}{j} W_j(K). \quad (1.2)$$

Intrinsic volumes and Minkowski functionals differ by a normalization factor

$$\kappa_{d-k}V_k(K) = \binom{d}{d-k}W_{d-k}(K) \quad (1.3)$$

for $k = 0, \dots, d$, $K \in \mathcal{K}$. However, the advantage of using the intrinsic volumes is that when K has dimension smaller than d , $V_k(K)$ does not depend on d (Schneider and Weil, 2008).

Inheriting the properties of the Lebesgue measure, the intrinsic volumes have the following properties:

- (a) invariance under rigid motions: $V_k(\theta K + x) = V_k(K)$, for all $\theta \in SO(n)$, $x \in \mathbb{R}^n$, $K \in \mathcal{K}$;
- (b) additivity: $V_k(K_1 \cup K_2) = V_k(K_1) + V_k(K_2) - V_k(K_1 \cap K_2)$, for $K_1, K_2 \in \mathcal{K}$;
- (c) continuity: given a sequence $\{K_i\} \subset \mathcal{K}$ such that $K_i \rightarrow K$ for $i \rightarrow \infty$, $K \in \mathcal{K}$, then $V_k(K_i) \rightarrow V_k(K)$ for $i \rightarrow \infty$.

Moreover, it holds

Theorem 1.2.2 (Hadwiger)

Let φ be an additive, continuous functional on \mathcal{K} being invariant under rigid motions. Then there exist constants c_k with $k = 0, \dots, d$ such that

$$\varphi(K) = \sum_{k=0}^d c_k V_k(K)$$

for $K \in \mathcal{K}$.

Hadwiger's theorem states the importance of the intrinsic volumes. Any functional with the properties (a), (b), and (c) can be expressed as a linear combination of the intrinsic volumes. In other words, the intrinsic volumes are a basis for the space of additive, continuous functionals invariant under rigid motions.

Now, we extend the definition of intrinsic volumes to more general sets. This is possible thanks to the additivity and the inclusion-exclusion principle. For $X \in \mathcal{R}$, there exist convex sets $K_i \in \mathcal{K}$, $i = 0, \dots, m < \infty$ such that $X = \bigcup_{i=0}^m K_i$, then

$$V_k(X) = \sum_{i=0}^m V_k(K_i) - \sum_{i=0}^{m-1} \sum_{j=i+1}^m V_k(K_i \cap K_j) + \dots + (-1)^{m+1} V_k\left(\bigcap_{i=1}^m K_i\right) \quad (1.4)$$

for $k = 0, \dots, d$. A generalization of the Steiner formula for polyconvex sets is presented in Schneider (1993, Chapter 4). Furthermore, the extension for polyconvex sets yields that the intrinsic volumes of $X \in \mathcal{S}$ observed on a compact convex window W are well defined ($X \cap W \in \mathcal{R}$ by definition of \mathcal{S}).

Geometric interpretation

The intrinsic volumes as well as the Minkowski functionals of convex bodies benefit from a straightforward geometric interpretation:

- $V_d = W_0 = V$ volume,
- $2V_{d-1} = dW_1 = S$ surface area,
- $\frac{2\pi}{d-1}V_{d-2} = dW_2 = M$ integral of mean curvature,
- \dots
- $\frac{2\kappa_{d-1}}{\omega_d}V_1 = \frac{2}{\kappa_d}W_{d-1} = \bar{b}$ mean width,
- $V_0 = \frac{1}{\kappa_d}W_d = \chi$ Euler number.

where ω_k is the surface area of the unit ball in \mathbb{R}^k .

The width of a body in a direction is the length of the orthogonal projection of the body onto that direction. For a convex body $K \in \mathcal{K}$, it can be expressed through the *support function*:

$$h(K, x) = \sup\{xy : y \in K\}, \quad x \in \mathbb{R}^d. \quad (1.5)$$

Denoting a direction in S^{d-1} as θ , the width of K in direction θ is $h(K, \theta) + h(K, -\theta)$. The *mean width* is defined as

$$\bar{b}(K) = \frac{2}{\omega_d} \int_{S^{d-1}} h(K, \theta) d\mathcal{H}^{d-1}(\theta). \quad (1.6)$$

Moreover, for a convex polygon in \mathbb{R}^2 with perimeter p , the mean width is p/π . For a convex polytope P in \mathbb{R}^3 with m edges, the mean width can be computed based on the length of its edges ℓ_i and the angles between facets γ_i (Ohser and Schladitz, 2009):

$$\bar{b}(P) = \frac{1}{4\pi} \sum_{i=1}^m \ell_i \gamma_i. \quad (1.7)$$

The integral of mean curvature, in d -dimension proportional to V_{d-2} , in 3d is equal to the mean width up to a multiplicative constant. To simplify the geometric interpretation of curvature, let us temporarily restrict to X being a morphologically regular set in \mathbb{R}^3 , i. e., a set that is morphologically closed and morphologically open. Then the two principal curvatures $1/r_1(s)$ and $1/r_2(s)$ are well defined and finite at each surface element s . The *integral of mean curvature*, or *integral of Germain's curvature*, is

$$M(X) = \int_{\partial X} \frac{1}{2} \left(\frac{1}{r_1(s)} + \frac{1}{r_2(s)} \right) ds, \quad (1.8)$$

and the *integral of total curvature* or *integral of Gaussian curvature* is

$$K(X) = \int_{\partial X} \frac{1}{r_1(s)r_2(s)} ds. \quad (1.9)$$

For a ball B_r of radius r , both principal curvatures are constant and equal to $1/r$. Therefore

$$M(B_r) = 4\pi r \quad \text{and} \quad K(B_r) = 4\pi.$$

As done for the Steiner formula 1.2.1 in (1.4), the definitions of integral of mean and total curvature can be extended to bodies in the convex ring. Note that this definition holds also for bodies that do not have a smooth surface.

The integral of total curvature has dimension zero and is proportional to the *Euler number*, or *Euler-Poincaré characteristic*. All convex bodies have Euler number equal to 1. The Euler number is a topological parameter:

$$\chi(X) = \#\{\text{connected components}\} - \#\{\text{tunnels}\} + \#\{\text{holes}\}.$$

Holes and tunnels are two different types of concavities. In case the body has a hole, its complement is divided in two components, whereas in case of a tunnel, the complement is connected. Roughly speaking, a hollowness inside an object, that cannot be seen from the outside, is a hole, as for instance the inside of an empty eggshell. A tunnel, in contrast, refers to a passage as in a torus or the handle of a cup.

The intrinsic volumes can be combined to define factors that describe the shape of objects or complex sets, more details are given in Section 2.1.2.

1.2.2 Random closed sets

As for random variables, the definition of random closed sets is based on an abstract probability space $(\Omega, \mathcal{A}, \mathbb{P})$ where Ω is non-empty, \mathcal{A} is a σ -algebra on Ω and \mathbb{P} is a probability measure: $\mathbb{P} : \mathcal{A} \rightarrow [0, 1]$. The definitions in this section are referred to Matheron (1975).

Definition 1.2.3 (RACS)

A *random closed set* Ξ is a Borel-measurable map defined on a probability space $(\Omega, \mathcal{A}, \mathbb{P})$ with values in \mathcal{F} furnished with the σ -algebra $\mathcal{B}(\mathcal{F})$, that is, for all $F \in \mathcal{F}$ the inverse image under Ξ is measurable, $\Xi^{-1}(F) \in \mathcal{A}$. The image measure \mathbb{P}_Ξ of \mathbb{P} under Ξ is the *distribution* of Ξ .

The distribution characterizes the random closed set in the sense that two random closed sets Ξ_1 and Ξ_2 having the same distribution are said to be *stochastically equivalent* and we write $\Xi_1 \sim \Xi_2$. Note that Ξ_1 and Ξ_2 may be defined on different probability spaces. Moreover, a random closed set Ξ is characterized by the *capacity functional* $T : \mathcal{C} \mapsto [0, 1]$

$$T(C) = \mathbb{P}_\Xi(\mathcal{F}_C) = \mathbb{P}_\Xi(\Xi \cap C \neq \emptyset).$$

The importance of this functional is expressed by the Choquet theorem. It states that the distribution of a random closed set can be completely determined by a functional on compact sets, namely the capacity functional. We define by recurrence a set of functionals depending on T

$$\begin{aligned} S_0(C) &= 1 - T(C) \\ S_k(C_0; C_1, \dots, C_k) &= S_{k-1}(C_0; C_1, \dots, C_k) - S_{k-1}(C_0 \cup C_k; C_1, \dots, C_{k-1}) \end{aligned}$$

for $C_0, \dots, C_k \in \mathcal{C}$, $k \in \mathbb{N}$.

Theorem 1.2.4 (Choquet)

Let $T : \mathcal{C} \rightarrow \mathbb{R}$ be a function with the following properties

- (a) $0 \leq T \leq 1$, $T(\emptyset) = 0$,
- (b) if $C_1, C \in \mathcal{C}$ and $C_i \searrow C$, then $T(C_i) \rightarrow C$,
- (c) $S_k(C_0; C_1, \dots, C_k) \geq 0$ for $C_0, \dots, C_k \in \mathcal{C}$, $k \in \mathbb{N}_0$.

Then there exists a uniquely determined probability measure \mathbb{P} on \mathcal{F} with

$$T(C) = \mathbb{P}(\mathcal{F}_C)$$

for all $C \in \mathcal{C}$.

A function with the properties (a), (b) and (c) is called an alternating Choquet capacity of infinite order. Choquet's theorem yields that a function T with such properties is a capacity functional for some random closed set Ξ with distribution $\mathbb{P}_\Xi = \mathbb{P}$. For example, one can define Ξ as the identity map on $(\mathcal{F}, \mathcal{B}(\mathcal{F}), \mathbb{P})$. For the proof, we refer the reader to Schneider and Weil (2008, Section 2.2).

Further important properties that RACS might have are

- two random closed sets Ξ_1 and Ξ_2 are *independent* if

$$\mathbb{P}(\Xi_1 \in A_1, \Xi_2 \in A_2) = \mathbb{P}(\Xi_1 \in A_1)\mathbb{P}(\Xi_2 \in A_2)$$

for $A_1, A_2 \in \mathcal{A}$;

- a random closed set Ξ is *stationary* or *macroscopically homogeneous* if its distribution is invariant under translations, i. e.,

$$\Xi \sim \Xi + x, \quad x \in \mathbb{R}^d;$$

- a random closed set Ξ is *isotropic* if its distribution is invariant under rotations, i. e.,

$$\Xi \sim \theta\Xi, \quad \theta \in SO(\mathbb{R}^d).$$

Stationarity and isotropy can be equivalently expressed by means of the capacity functional T as

$$\begin{aligned} T(C) &= T(C - x), \quad x \in \mathbb{R}^d, \quad \text{and} \\ T(C) &= T(\theta^{-1}C), \quad \theta \in SO(\mathbb{R}^d), \end{aligned} \tag{1.10}$$

respectively, for all $C \in \mathcal{C}$.

The mean value function of a RACS Ξ is defined by replacing Ξ with the stochastic process generated by its indicator function $\mathbf{1}_\Xi$

$$m(x) = \mathbb{E}[\mathbf{1}_\Xi(x)] = \mathbb{P}(x \in \Xi) = \int_{\Omega} \mathbf{1}_{\Xi(\omega)}(x) \mathbb{P}(d\omega) = \int_{\mathcal{F}} \mathbf{1}_F(x) \mathbb{P}_\Xi(dF) \tag{1.11}$$

for $x \in \mathbb{R}^d$ (Schneider and Weil, 2008). If Ξ is stationary, then the mean value of Ξ is independent of x . If Ξ is stationary, the *covariance* of Ξ is defined as

$$C(x) = \mathbb{P}(0 \in \Xi, x \in \Xi) \tag{1.12}$$

for $x \in \mathbb{R}^d$. In case Ξ is also isotropic, the covariance depends only on the norm of x , $C(x) = C(\|x\|)$.

Intrinsic volume densities

Now, we extend intrinsic volumes to characterize random closed sets. Let us assume that Ξ is a stationary RACS with values almost surely in the extended convex ring \mathcal{S} . Then $X \cap K$ can be expressed as a finite union of convex sets. Let us denote $\#(\Xi \cap K)$ the minimum number of convex sets necessary to represent $\Xi \cap K$. We assume that $\mathbb{E}[2^{\#(\Xi \cap K)}] < \infty$ for all $K \in \mathcal{K}$. Let us suppose to observe Ξ in a compact convex window W with non empty interior and with positive volume $V_d(W)$. The intersection of Ξ with the window belongs to the convex ring, therefore the intrinsic volumes $V_k(\Xi \cap W)$ are well defined, for $k = 0, \dots, d$. Avaraging stochastically and spatially, the *intrinsic volume densities* of Ξ are defined as follows

$$V_{V,k}(\Xi) = \lim_{a \rightarrow \infty} \frac{\mathbb{E}[V_k(\Xi \cap aW)]}{V_d(W)} \quad (1.13)$$

for $k = 0, \dots, d-1$ and

$$V_{V,d}(\Xi) = \frac{\mathbb{E}[V_d(\Xi \cap W)]}{V_d(W)}, \quad (1.14)$$

that is the *volume density* or *volume fraction* of Ξ . The volume density can be interpreted as the expected volume of Ξ observed in a unit volume window. Moreover, thanks to stationarity, it holds

$$V_{V,d}(\Xi) = \mathbb{P}(0 \in \Xi) = T(\{0\}) = \mathbb{E}[\mathbf{1}_\Xi(0)].$$

We remark that the covariance $C(x)$ of Ξ can be interpreted as the volume density of the stationary random closed set intersected with its translations, for $x \in \mathbb{R}^d$

$$C(x) = V_{V,d}(\Xi \cap (\Xi - x)).$$

For the lower dimensional intrinsic volume densities, the existence of the limit is guaranteed by the properties of the intrinsic volumes and the integrability condition given above (Schneider and Weil, 2008). A geometric interpretation analogous to that given for the intrinsic volumes of polyconvex sets is valid. In 3d:

- $V_{V,3} = V_V$ volume density (or specific volume),
- $2V_{V,2} = S_V$ surface area density (or specific surface area),
- $\pi V_{V,1} = M_V$ density of the integral of mean curvature,
- $V_{V,0} = \chi_V$ density of the Euler number.

Intrinsic volume densities can be combined to obtain a shape factor that characterizes unions of closed sets. The *structure model index* (SMI) is defined as

$$f_{SMI} = 6 \frac{V_V S'_V}{S_V^2} = 12 \frac{V_V M_V}{S_V^2}. \quad (1.15)$$

It is considered a shape factor for systems of objects because it has different values for qualitatively different structures. For instance, it is equal to 0 for systems of planes, 4 for systems of non-overlapping balls, 3 for non-overlapping cylinders. It can be estimated on images of structures without the need to mesh the surface (Ohser et al., 2009b). More examples will be given in Chapter 3 and 4, where the SMI will be used to characterize fiber systems and foams.

1.2.3 Point processes

Point processes are a special case of random closed sets with the property that they are almost surely locally finite. To rigorously define point processes, we first recall the notion of counting measures. We refer to Schneider and Weil (2008, Chapter 3) for proofs and more details.

A measure η defined on the Borel sets of \mathbb{R}^d is locally finite if $\eta(C) < \infty$ for all compact sets $C \in \mathcal{C}$. We denote the space of all locally finite measures on \mathbb{R}^d as $\mathcal{M} = \mathcal{M}(\mathbb{R}^d)$. This space can be equipped with the σ -algebra \mathcal{M} for which all the maps Φ_A for $A \in \mathcal{B}$ are measurable, where

$$\begin{aligned}\Phi_A : \mathcal{M} &\rightarrow \mathbb{R} \cup \{\infty\} \\ \eta &\mapsto \eta(A).\end{aligned}$$

A measure $\eta \in \mathcal{M}$ such that $\eta(A) \in \mathbb{N}_0 \cup \{\infty\}$ for all $A \in \mathcal{B}$ is a counting measure on \mathbb{R}^d . Let \mathcal{N} be the set of all counting measures on \mathbb{R}^d . Then \mathcal{N} is a measurable subset of \mathcal{M} . We equip \mathcal{N} with the σ -algebra \mathcal{N} induced by \mathcal{M} .

Interpreting a point of \mathbb{R}^d as a measure allows to construct a counting measure. We identify $x \in \mathbb{R}^d$ with the Dirac measure δ_x

$$\delta_x(A) = \begin{cases} 1 & x \in A \\ 0 & x \notin A \end{cases}$$

for $A \in \mathcal{B}$. Then, the finite or countable sum

$$\eta = \sum_{i=1}^k \delta_{x_i}, \quad \text{for } k \in \mathbb{N}_0 \cup \{\infty\}, \quad x_i \in \mathbb{R}^d$$

is a counting measure on \mathbb{R}^d . If the points x_i are pairwise distinct, $\eta(\{x\}) \leq 1$ for all $x \in \mathbb{R}^d$ and η is called *simple*. The space of simple counting measures is referred to as \mathcal{N}_s . Moreover, every counting measure $\eta \in \mathcal{N}$ can be expressed as a finite or countable sum of Dirac measures (Schneider and Weil, 2008, Lemma 3.1.3). This allows to associate to each counting measure the set of points $x_i \in \mathbb{R}^d$ for $i = 1, \dots, k$ with $k \in \mathbb{N}_0 \cup \{\infty\}$, thence the intuitive interpretation of point processes as random collections of points in space.

Definition 1.2.5

A (*random*) *point process* Φ is a measurable map defined on a probability space $(\Omega, \mathcal{A}, \mathbb{P})$ with values in \mathcal{N} furnished with the σ -algebra \mathcal{N} . If Φ is defined on \mathcal{N}_s supplied with the induced σ -algebra \mathcal{N}_s , then Φ is a *simple* point process. The distribution of the point process is the image measure \mathbb{P}_Φ of \mathbb{P} under Φ . The measure $\Lambda(A) = \mathbb{E}[\Phi(A)]$ for $A \in \mathcal{B}$ is the *intensity measure* Λ of Φ .

If Φ is simple, the value of Λ on a set A is the mean number of points of Φ in A . If the point process Φ is stationary, then the intensity measure is absolutely continuous with respect to the Lebesgue measure, i. e., there exists a constant $\lambda > 0$ called the *intensity* of Φ such that

$$\Lambda(A) = \lambda V_d(A) \tag{1.16}$$

for $A \in \mathcal{B}$.

Theorem 1.2.6 (Campbell)

Let Φ be a point process on \mathbb{R}^d with intensity measure Λ and let $f : \mathbb{R}^d \rightarrow \mathbb{R}$ be a non-negative measurable function, then $\int_{\mathbb{R}^d} f d\Phi$ is measurable and

$$\mathbb{E} \left[\int_{\mathbb{R}^d} f d\Phi \right] = \int_{\mathbb{R}^d} f d\Lambda.$$

The proof is based on the definition of the intensity measure and on the fact that the statement holds for indicator functions on Borel sets (Schneider and Weil, 2008).

Another useful measure to characterize point processes is the Palm distribution. The idea is to consider the distribution of the process given that the origin belongs to the process.

Definition 1.2.7 (Palm distribution)

Let Φ be a point process with values in $(\mathcal{N}, \mathcal{N})$, then the *Palm distribution* \mathbb{P}^0 of Φ is given by

$$\mathbb{P}^0(A) = \frac{1}{\lambda} \mathbb{E} \left[\sum_{x \in \Phi} \mathbf{1}_{[0,1]^d}(x) \mathbf{1}_A(\Phi - x) \right]$$

for $A \in \mathcal{N}$.

For an arbitrary point $x \in \mathbb{R}^d$, the Palm distribution is defined as $\mathbb{P}^x(A) = \mathbb{P}^0(A - x)$, $A \in \mathcal{N}$.

In image processing applications, sometimes an alternative nomenclature for point processes is adopted (Ohser and Schloditz, 2009). Instead of the terms point process and intensity, *point field* and *density* are preferred as they more clearly indicate the space (and not time) dependence.

Poisson point process**Definition 1.2.8**

A simple point process Φ on \mathbb{R}^d with intensity measure Λ is a *Poisson point process* if

- for each $A \in \mathcal{B}$ with $\Lambda(A) < \infty$, $\Phi(A)$ has Poisson distribution with parameter $\mathbb{E}[\Phi(A)] = \Lambda(A)$ (Poisson counting variables), and
- for pairwise disjoint Borel sets $A_1, \dots, A_m \in \mathcal{B}$, $m \in \mathbb{N}$ the variables $\Phi(A_1), \dots, \Phi(A_m)$ are independent (independent increments).

Note that Φ has Poisson counting variables if and only if it holds

$$\mathbb{P}(\Phi(A) = k) = e^{-\Lambda(A)} \frac{\Lambda(A)^k}{k!}$$

for $k \in \mathbb{N}_0$ and $A \in \mathcal{B}$. Moreover, this property yields the property of independent increments (Schneider and Weil, 2008). If a Poisson point process is stationary, then it is also isotropic. In fact, stationarity implies that there exists $\lambda > 0$ such that $\Lambda = \lambda V$, with V the Lebesgue measure in \mathbb{R}^d . Then, if $\theta \in SO(\mathbb{R}^d)$ is a rotation, $\theta\Lambda = \Lambda$ due to the invariance under rigid motions of the Lebesgue measure. Poisson processes are the most analytically tractable point processes.

Generalized point processes

Point processes can be generalized by considering counting measures on a space E more general than \mathbb{R}^d . E is required to be a topological locally compact space with a countable base on which a Borel σ -algebra is defined. Poisson processes on E can be stationary but not isotropic. For example, E may be a subspace of \mathcal{F} with certain properties. A process of k -flats is a point process in the space of k -dimensional affine subspaces of \mathbb{R}^d for $k = 0, \dots, d-1$. With $k = 1$ and $k = d-1$, we talk about processes of lines and of flats or hyperplanes, respectively. By dilating a Poisson line process with a compact structuring element, a Poisson cylinder process, or Poisson process of dilated lines, is obtained. This process will be widely treated in Section 3.2.2.

Another class of generalized point processes are *marked point processes*. Heuristically, to each point we assign a random mark, or weight, in \mathbb{R} or in a general space.

Definition 1.2.9

Let M be a locally compact topological space with a countable base. A *marked point process* in \mathbb{R}^d with mark space M is a simple point process Φ in $\mathbb{R}^d \times M$ with intensity measure Λ such that

$$\Lambda(C \times M) < \infty$$

for all $C \in \mathcal{C}$.

Projecting the marked point process Φ via the map $(x, m) \mapsto x$, we obtain the *ground process* or *unmarked point process* Φ_0 . For example, one can define a marked point process with $M = \mathbb{N}$ such that the mark corresponds to the multiplicity of the point. In this way, an arbitrary point process, also a non simple one, can be interpreted as a marked point process.

Usually, translations and rotations of a marked point process only apply to the first component, i. e., to the ground process. Stationarity and isotropy of the marked process depend on both the properties of the ground process and of the marks. Given $\Lambda > 0$, the intensity measure of a marked point process Φ with stationary ground process has the following decomposition (Schneider and Weil, 2008)

$$\Lambda = \lambda V \otimes \mathbb{Q} \tag{1.17}$$

where $\lambda > 0$ is the intensity of Φ and \mathbb{Q} is a probability measure on M called *mark distribution*. Moreover, \mathbb{Q} is uniquely determined. Note that λ is also the intensity of the (stationary) ground process Φ_0 . Thanks to Campbell's theorem, it holds

$$\mathbb{Q}(A) = \frac{1}{\lambda} \sum_{(x,m) \in \Phi} \mathbf{1}_B(x) \mathbf{1}_A(m)$$

for $B \in \mathcal{B}(\mathbb{R}^d)$ with $V(B) = 1$ and $A \in \mathcal{B}(M)$.

When the marks are compact sets, we talk about *germ-grain processes*, then the distribution \mathbb{Q} is often referred to as *grain distribution* (Schneider and Weil, 2008). The Boolean model (Section 3.2.1) is an example of germ-grain process such that the ground process is a Poisson point process. The orientation distribution of the grains determines whether the process is isotropic. Other examples are given by interpreting cells, facets, edges, and vertices of a random tessellation as marked point processes with marks in the space of k -dimensional polyhedra, with $k = 0, \dots, 3$, see Section 4.1.

Chapter 2

Characterization of 3d objects

As imaging technologies improve, object characterization based on 2d images becomes less relevant. It is now possible to capture the whole spatial complexity of objects even with desktop devices. Consequently, the demand for fast and simple methods to characterize size and shape in 3d grows. Our contribution to the analysis of unconnected objects is to define a collection of unambiguous parameters that exhaustively describe three dimensional shapes and can be efficiently estimated from the images.

Shape is an essential information in many application fields. For instance, morphology of cellular or molecular particles offers an insight into the chemical reactions occurring in the originating process (Merson-Davies and Odds, 1989; Landry et al., 1999). Analyzing the shape of grains yields information on their material composition (Santamarina and Cho, 2004). Furthermore, in Ehrlich and Weinberg (1970) and Livsey et al. (2013) a morphological characterization is applied to deduce the environmental formation of grains and the history of sediments in Antarctica. The shape of graphite particles affects the thermal properties of cast iron (Velichko et al., 2008). In geology (Kaminski et al., 2008), hydrodynamic (Stückrath et al., 2006), mechanical engineering (Lin and Miller, 2005), and several other applied sciences, a thorough description of particle shapes improves the understanding of the physical behavior of rocks and granulate systems. Even in the implementation of robots' grasping abilities (Huebner et al., 2008), it is crucial to describe three-dimensional objects by only a few parameters.

Here, we will focus on an application to technical cleanliness. In the production line of automotive industry, dirt particles collect on the surface of mechanical components. Residual dirt might reduce the performance and durability of assembled products. The standards ASTM F1877 (2003) and ISO 16232 (2007) dictate the principles for cleanliness inspection, including techniques to collect and analyze samples of dirt particles. Geometric characterization of these particles allows to identify their potential danger. In fact, the size and shape of particles yield whether a filter would stop them or not. For instance, a long and thin fiber would slip through the holes of a filter while a flat chip would be stopped. So far, the characterization has been based on 2d microscopic images. In ASTM F1877 (2003), the geometric features of the particles to be measured are defined heuristically. From a theoretical point of view, an even richer list of parameters to characterize two-dimensional bodies is presented in Stoyan and Stoyan (1994). Mainly, the parameters are divided into *size parameters*, such as the diameters of the inscribed and circumscribed circle, and *shape factors*, e. g., roundness. Estimating geometric characteristics in 2d images is computationally easy. However,

a planar image of a three-dimensional object is only a projection on a given fixed plane. On the one hand, restricting to two dimensions yields a severe loss of information. On the other hand, the algorithmic complexity to estimate characteristics on 3d images drastically grows.

A detailed geometric characterization of 3d particles is presented in Parra-Denis et al. (2008). In addition to basic features (e. g., volume and surface area), shape indices and geodesic features are introduced. The mass distribution is characterized by the axes of inertia. With this work in mind, we supplemented the collection of geometric descriptors to adapt to the requirements of technical cleanliness. First of all, the possibility to exactly reproduce the measurements is particularly important. Secondly, efficient algorithms to estimate the characteristics on binary images of the objects are necessary. Furthermore, the features must suffice to objectively classify the objects. In fact, in addition to parameters to characterize planar objects, ASTM F1877 (2003) provides a qualitative guideline to classify particles according to their shape. Two classes of objects can be naturally distinguished by means of the aspect ratios. Granular shapes are those with comparable length and width, while fibers or needles have typically length much larger than the width. If the third dimension is also available, i. e., the thickness of the object, then another class can be recognized: “flat” objects, called chips or flakes. The classification tools we provide are thresholds of the parameters separating the classes. The possibility to compare classes of particles analyzed in different laboratories is very important, thus the definition of the classes has to be based on objective criteria. The classification is purely geometric and alone does not yield information on the potential danger of dirt particles. Indeed, the danger of the particles can only be determined from the whole geometric characterization combined with information about the material composition. Additionally, it depends on the specific context. For instance, at which point of the factory line was the sample collected? Which part is being produced? Which is the functionality and the expected life-time of the part? Note that the material composition can also be extracted from tomographic images of the samples depending on the mean grey value of the particle. More details are given in Section 2.4.

In the following, we will first define parameters to describe the geometry of three-dimensional objects. With the application to technical cleanliness in mind, shape is understood as the configuration of the portion of space filled by an object. Thus, identifying surface roughness or fine structures is out of our scope. For each feature, we also outline or give references to algorithms for fast computation on volume images. An analysis of the estimation errors is presented in Section 2.2. In Section 2.3, we discuss how to obtain the geometric classification of objects in the three classes fiber, chip, and granule. Finally, we characterize and classify a real sample of dirt particles in Section 2.4.

The main results presented in this chapter are published in Vecchio et al. (2012b). Moreover, the software MAVIparticle (Fraunhofer ITWM, Department of Image Processing, 2012) has been specifically developed to characterize samples of 3d objects based on μ CT images. We developed algorithms to estimate the characteristics introduced in this chapter to supplement some of the features already available in MAVI (Fraunhofer ITWM, Department of Image Processing, 2005).

2.1 Object characterization

First of all, it is necessary to distinguish between objects in the real world and their images. An object is understood as a simply connected compact body X in \mathbb{R}^3 with non empty interior. Parameters characterizing objects, i.e., bodies, are defined in the continuous Euclidean space. Nevertheless, what we observe is only the digitized image of the body. Such a digital object \tilde{X} is a collection of lattice points with respect to an adjacency system, see also Section 1.1. By definition, an object \tilde{X} is constituted by a finite number of points, i.e., pixels. It will be sometimes convenient to think of objects as point clouds. When treating the estimation of the features, we will assume to deal with a binary image containing one single object.

2.1.1 Basic measures

Volume V and **surface area** S are the simplest descriptors for the size of an object. These quantities correspond to the highest dimensional intrinsic volumes of a three dimensional compact body, $V = V_3(X)$ and $S = 2V_2(X)$. As discussed in Section 1.2.1, two other intrinsic volumes exist: $V_1(X)$, which is proportional to the integral of mean curvature M , and $V_0(X) = \chi$, the **Euler number**. Note that in image analysis this set of characteristics is often referred to as “object features”.

The mean width of a convex body in \mathbb{R}^3 is, up to a multiplicative constant, proportional to the integral of mean curvature. The width is also referred to as *Feret diameter* or *caliper diameter*. While the term caliper is usually applied when measuring the size of real objects with the instrument of the same name (ASTM D4791, 2010), Feret diameter is preferred in image analysis. It typically refers to the length of the projection of the body along a given direction, i.e., the largest distance between parallel planes with normals in that direction and enclosing the body.

The interpretation of the Euler number yields information on the topology of X . The number of tunnels can be deduced by comparing the Euler number of X with that of the complement X^C , which in images is the background. Moreover, in the digital representation of a body, it is possible to morphologically close holes (Soille, 1999). This is helpful for the computation of other features, as for instance the geodesic length (Section 2.1.4).

The volume of a digital object is simply obtained by pixel count. Estimating the other intrinsic volumes requires more sophisticated techniques. A well established class of methods applies a stereological approach based on the Crofton formula (Ohser and Mücklich, 2000; Ohser and Schladitz, 2009). The advantage is that the surface of the object does not need to be triangulated, in fact, the estimation of the intrinsic volumes is based on local information. For surface area and integral of mean curvature, it reduces to computing suitable weighted sums of occurrences of boundary pixel configurations. Typically, boundary configurations are $2 \times 2 \times 2$ lattice subsets which contain both background and foreground pixels. In a newer approach by Ohser et al. (2013), the estimation of the integral of mean curvature is improved by considering $3 \times 3 \times 3$ boundary configurations. These estimators are unbiased for compact bodies being morphologically regular with respect to all line segments connecting vertices of the lattice unit cell and are multigrid convergent (Ohser et al., 2002). See also (Ohser and Schladitz, 2009, Theorem 3.1). Nevertheless, for arbitrary objects, the goodness of the estimation strongly depends on the image resolution. The relative error of the surface area estimator based on $2 \times 2 \times 2$ pixel configurations is analyzed for decreasing lattice distance

in Section 2.2.

Hadwiger's Theorem (1.2.2) shows that the four intrinsic volumes are a basis in the space of regular functionals describing bodies. Hence, other regular functionals would be redundant.

2.1.2 Isoperimetric shape factors

The *isoperimetric* problem refers to the question of determining which shape enclosed in a given perimeter has the largest area. The solution on the plane, already known by the ancient Greeks, is the circle. Let P and A be perimeter and area of a two-dimensional body. For the circle $P^2 = 4\pi A$, whereas for general shapes the *isoperimetric inequality* holds:

$$P^2 \geq 4\pi A.$$

Analogously, in 3d it holds

$$S^3 \geq 36\pi V^2, \quad (2.1)$$

where equality is realized by the sphere.

The isoperimetric inequality can also be seen in a more general setting. Namely, as a special case of Minkowski's inequalities for mixed volumes of convex bodies ((Schneider, 1993, Theorem 6.2.1)). From this theorem, one can deduce the generalization of the isoperimetric inequality in dimension d :

$$\left(\frac{V_{d-1}}{\omega_d}\right)^d \geq \left(\frac{V_d}{\kappa_d}\right)^{d-1}, \quad (2.2)$$

which in $d = 3$ implies the following

$$M^2 \geq 4\pi S \text{ and } S^2 \geq 3VM \quad (2.3)$$

called the quadratic Minkowski inequalities. By raising these to the power of two and substituting, two cubic inequalities are derived, so that S and M are split:

$$S^3 \geq 36\pi V^2, \quad M^3 \geq 48\pi^2 V, \quad (2.4)$$

where the first one is exactly (2.1).

Based on these relations, a set of shape factors is deduced (Stoyan et al., 1995):

Definition 2.1.1

Let X be a compact simply connected body with non empty interior with intrinsic volumes $V = V(X)$, $S = S(X)$ and $M = M(X)$. The *isoperimetric shape factors* of X are

$$f_1 = 6\sqrt{\pi} \frac{V}{\sqrt{S^3}}, \quad f_2 = 48\pi^2 \frac{V}{M^3}, \quad f_3 = 4\pi \frac{S}{M^2}. \quad (2.5)$$

In all the inequalities introduced above, equality holds only for balls. Thence, these shape factors are equal to 1 for balls. They all have values between 0 and 1 for convex bodies, but f_2 and f_3 can be larger than 1 for polyconvex objects. Deviations from 1 describe deviations from the spherical shape. Often, f_1 is referred to as *sphericity* (Parra-Denis et al., 2008), where conversely the shape factor

$$I_C = 6^3 \frac{V^2}{S^3}$$

is called *compactity* and describes deviations from the cube. This is a combination of the isoperimetric shape factors and thus carries redundant information.

The precision in estimating the shape factors on images depends in first instance on the accuracy of the estimation of the intrinsic volumes. Furthermore, being ratios, these parameters are particularly prone to discretization errors. An overview of the most common problems arising in binary images are outlined in (Montero and Bribiesca, 2009), together with some possible solutions. An analysis of the error on cylinders with different aspect ratios is presented in Section 2.2. Note that in this chapter by cylinder we will always mean a compact cylinder with circular cross section.

2.1.3 Convex hull features

Volume and surface area do not describe how the object extends in space. To measure this, we consider features which ignore concavities and thus are upper bounds on the space filled by the object. More precisely, these features yield the same value if computed on the object or on its convex hull. Furthermore, considering the vertices of the convex hull instead of all the points (pixels) constituting the digitized object yields a remarkable reduction of the computational size of problem.

The computation of the convex hull is based on the QuickHull algorithm (de Berg et al., 2008). This is a divide and conquer method that consecutively excludes points lying inside the convex hull. The resulting set of vertices of the convex hull is a subset of the points forming the original object. We can keep track of the difference between the object X and its convex hull $\mathcal{CH}(X)$ via the

$$\text{convexity factor} = \frac{V(X)}{V(\mathcal{CH}(X))}.$$

It is equal to 1 for convex shapes and smaller the more concave the object is. When estimating it on digitized objects, however, it can be smaller than 1 also for convex objects. Possible reasons are surface roughness or discretization errors in fine structures. To reduce this effect, the image can be filtered (e. g., by a median filter, Section 1.1) to smooth the surface. One should also be sure to employ the same discretization for the object and for its convex hull. For instance, computing the volume of \tilde{X} by pixel count and the volume of $\mathcal{CH}(\tilde{X})$ based on the polyhedral approximation, the two measures cannot be correctly compared.

The *size* of an object can be described by measuring how much X extends in three significant orthogonal directions. We will refer to these measures by *length*, *width* and *thickness*, sorted in decreasing order. The standards ASTM F1877 (2003) and ASTM D4791 (2010) suggest to measure the size of objects in 2d and 3d, respectively, by Feret diameters. The largest is the **maximal Feret diameter** d_F , Figure 2.2(a), that is the largest Euclidean distance between pairs of points in the object. According to those standards, the maximal Feret diameter is the length of an object. Width is then defined as the maximal Feret diameter of the projection onto the plane perpendicular to the direction of d_F . The thickness is found projecting the object onto the line perpendicular to both the direction of d_F and of the width and taking the largest distance between the points. With this definition, the spatial diagonals of a cuboid determine its size. However, this does not meet the intuitive idea of size that for a cuboid corresponds to the measures of its edges. We can achieve this by the following definition:

Definition 2.1.2

Call $C \subset \mathbb{R}^3$ a cuboid with arbitrary orientation (w. a. o.) if there exist $x_i, y_i, z_i \in \mathbb{R}$ for $i = 1, 2$ and a rotation $\theta \in \text{SO}(\mathbb{R}^3)$ such that $C = \theta C_0$ with $C_0 = [x_1, x_2] \times [y_1, y_2] \times [z_1, z_2]$. The *minimum volume bounding box (MVBB)* of X as above, is a cuboid w. a. o. C such that:

- $X \subseteq C$,
- $\text{vol}(C) \leq \text{vol}(C')$ for all cuboids w. a. o. C' s. t. $X \subseteq C'$.

Then the *size* of X is given by the measures of the edges of C . Sorted in decreasing order, these are **length** l , **width** w and **thickness** t .

In Figure 2.1, the minimum volume bounding box and the size of a chip-like ellipsoid are represented. In general, the MVBB of an object is not unique. In fact, bodies with axial symmetries take infinitely many MVBB arbitrarily rotated about the axes of symmetry. Spheres and cylinders with circular cross section belong to this class. However, the size of the box remains constant. Moreover, we conjecture that the following claim holds

Claim 1 (Uniqueness of l , w , and t)

If C and C' are minimum volume bounding boxes of X with measures of the edges l, w, t and l', w', t' , respectively, then $l = l', w = w'$ and $t = t'$.

To our knowledge, this fact has not been proven nor counterexamples are known. We suppose that multiple orientations of the MVBB are possible only related to some symmetry in the objects. Thus, also the edge lengths remain constant. In fact, the claim asserts that if C and C' are MVBB for an object X , then there exists a rotation θ such that $C = \theta C'$. But then, it should hold that $X = \theta X$ and thus, X has an axis of symmetry.

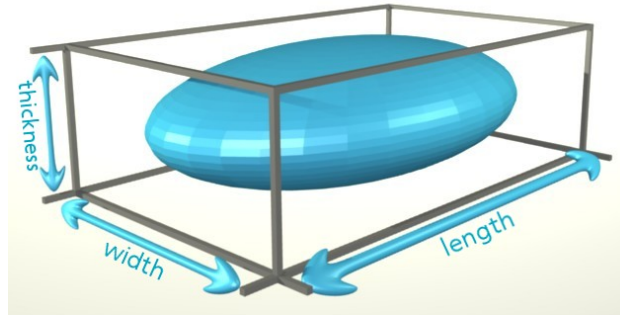


Figure 2.1: Ellipsoid and its minimum volume bounding box.

Parra-Denis et al. (2008) define the size of an object by the moments of inertia. This definition is based on rotational properties of bodies belonging to a physical space. Conversely, in our context, we aim at describing bodies only depending on the space they actually fill. In fact, it is important to establish whether a particle would be stopped by a filter of a given fineness or not. Despite the MVBB and inertia axes yield the same measure of size for objects with rotational symmetries, they differ for more complex shapes.

In some applications, e. g., crystallography, the orientation of the grains is very important. The rotations that move the MVBB into the axis aligned bounding box can be seen as

defining the orientation of the object, e. g., by Euler angles. The direction of the length corresponds to the direction of the main axis of the object. Alternatively, one can define the orientation according to the maximal Feret diameter. Note that for long and thin objects, e. g., straight fibers with small aspect ratio, length and maximal Feret diameter are realized on almost aligned directions.

Algorithm

Efficient algorithms are based on geometric properties of the MVBB. As mentioned, due to the convexity of cuboids, a box bounding an arbitrary object bounds its convex hull, too. Hence, the input for our algorithm is the point set S given by the vertices of the convex hull $\mathcal{CH}(\tilde{X})$. In the 2d case, a polygon has an edge lying on an edge of the minimum area bounding rectangle (Freeman and Shapira, 1975). Thus, it suffices to loop once on the edges of the polygon, construct the enclosing rectangle for each, and take the one with smallest area. Unfortunately, this property cannot be easily generalized to higher dimensions. In fact, a polyhedron has in general no face lying on a face of its minimum volume bounding box. Think for instance of a regular tetrahedron: only the edges lie on the faces of its MVBB. The best property found so far is that two edges of the polyhedron lie on two adjacent facets of the MVBB (O'Rourke, 1985). However, an exact algorithm based on this rule (O'Rourke, 1985) is of cubic complexity in the number of points – computational costs which are in general too high for applications. Therefore, we rather apply an algorithm approximating the real minimum volume bounding box in nearly linear time (Barequet and Har-Peled, 2001).

First, we construct a supporting bounding box B^* . Compute the maximal Feret diameter of the point set S . The segment d_0 connecting two points realizing the maximal Feret diameter is the first edge of B^* . Then the points in S are projected onto the plane perpendicular to d_0 . The maximal Feret diameter of the projection of S in this plane yields the second edge d_1 of the box. The direction of the third edge d_2 is now fixed due to orthogonality with d_0 and d_1 , its length is the maximal distance between pairs of points in S projected in this direction. Thus B^* is completely determined.

In general, the box B^* is not the bounding box of minimum volume. However, based on B^* , the MVBB can be effectively approximated (Barequet and Har-Peled, 2001). The idea is to use the axes of B^* as a new reference system. On each edge, define a unit measure equal to $1/N$ times the length of the corresponding edge. This yields a grid in B^* with N^3 points. Fix an arbitrary vertex O of B^* as the origin, connecting O to each grid point defines a direction v_i . Now, construct the box bounding S with an edge parallel to v_i for $i = 0, \dots, N^3 - 1$ (the segment that connects O with itself does not generate a direction). Once the direction of an edge is fixed, computing the minimum volume box reduces to projecting the points onto the plane perpendicular to the first edge, then computing the minimum area bounding rectangle in 2d.

The accuracy of the algorithm depends on N . In fact, the fineness of the grid on B^* determines the number of directions tested. However, note that not all the N^3 points in the grid yield different directions. For example, with $N = 10$, 840 different directions are generated. In practical applications, this proved to be enough. For instance, consider the ellipsoid displayed in Figure 2.1. Its axes measure $20 \times 60 \times 80$ pixels. While it is constituted of about 50 000 pixels, the number of vertices of its convex hull is only 655. The computation of the minimum volume bounding box takes about 3 seconds under Windows on an Intel Xeon

E550 (2.27 GHz core speed, 48 GB RAM, two processors). In this case, the real minimum volume bounding box is analytically known, so the accuracy can be easily calculated. The relative error is 0.2% and does not depend on the orientation of the object. The latter fact is not surprising as the tested directions are chosen from B^* , whose edges induce a reference system independent of the axes.

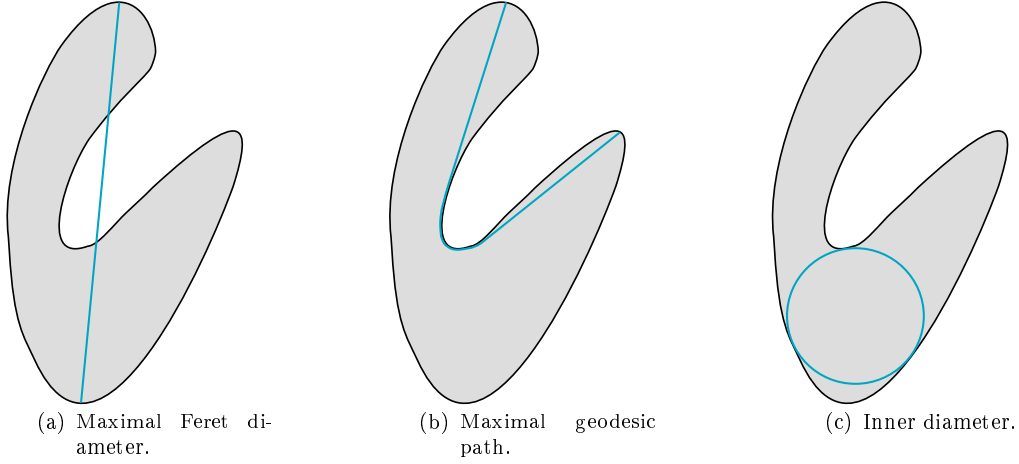


Figure 2.2: Particle cross section with size features.

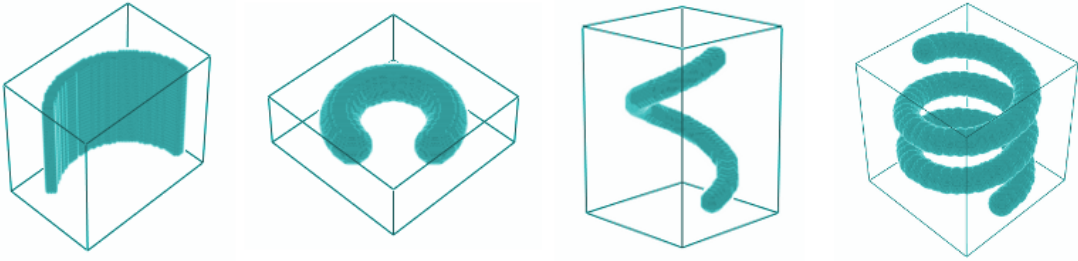


Figure 2.3: Examples of non-convex objects: a bended chip and three twisted fibers. Bounding boxes to enhance visualization, do not correspond to the MVBB.

2.1.4 Further size characterization

In the previous section, we worked on the convex hull of bodies. However, the convex hull is a rather bad approximation for bodies with concavities. Take for example the “bended” chip and the “twisted” fibers in Figure 2.3. The chip can be seen as a parallelepiped bend around a cylinder. Thus, one would want to measure the size of the object as the measure of the edges of the parallelepiped. Analogously for the fibers, natural length and thickness would be those of the corresponding “unwound” fibers (with axis lying on a line). The size as measured by the MVBB does not yield these measures. Therefore, in this section we define features able to measure length and thickness accounting for concavities of objects. We temporarily restrict to objects with neither holes nor tunnels (this case will be discussed in the end of the section).

First, we consider the thickness of bodies. We define a parameter that can be also interpreted as a measure of the largest core of X , as in Figure 2.2(c).

Definition 2.1.3

The measure of the diameter of the largest ball completely contained in X is the *inner diameter* or *maximal local thickness* of X .

The inner diameter of a digitized object is computed as the maximum of the Euclidean distance transform (EDT):

Definition 2.1.4

Let X be a body in \mathbb{R}^d , then the Euclidean distance transform EDT_X of X maps to each point of X its shortest distance to the complementary set:

$$\begin{aligned} EDT_X : \quad X &\rightarrow [0, \infty) \\ x &\mapsto \text{dist}(x, X^C). \end{aligned}$$

The EDT of the foreground \tilde{X} of a binary image can be estimated in linear time in the number of pixels of the image (Maurer et al., 2003).

Spherical granulometry gives a more detailed measure of the size of an object. The idea, first introduced by Matheron (1975), was inspired by a sieving procedure: letting grains through a sieve of increasing hole size separates the grains depending on their maximal thickness. In terms of mathematical morphology, it is a sequence of openings with balls of increasing radii (Section 1.1). Hence, the spherical granulometry yields the volume weighted thickness distribution of the particle. The maximum is the inner diameter as obtained by EDT.

In ASTM F1877 (2003), the length of an unwound fiber is measured by the length of its medial axis. However, the medial axis of a complex shape or an object with rough surface can be composed of many branches, thus making the interpretation of its length ambiguous. An alternative approach consists in considering the geodesic distance between points inside the object (Lantu  joul and Maisonneuve, 1984).

Definition 2.1.5

The *geodesic arc* between two points x and y in the body X is the shortest continuous path connecting x and y within X ; its length is the *geodesic distance* between x and y . The length of the longest path for all pairs x and y from X is the *geodesic length* or *elongation* L_g of X .

In Figure 2.2(b), the path realizing the elongation is represented. As motivated in (Lantu  joul and Maisonneuve, 1984), the advantages of this definition are manifold. First, despite the fact that we gave the interpretation for fibrous shapes, it is well defined for all kinds of objects. Furthermore, the elongation is a global minimum of a continuous function on a compact domain, its value is unique. Likewise the MVBB, there can exist multiple paths realizing the elongation for star-shaped objects, as cubes or spheres, but with the same length. Finally, the definition of the elongation is robust: if the object is slightly deformed, its elongation also varies minimally. Also, it is not affected by surface roughness.

The estimation on digitized objects is efficient. It is based on a two-step procedure. Given a suitable starting point $P \in \tilde{X}$, the geodesic distances to all other points in the

object are computed. A point realizing the maximum is taken as the new starting point. Again, the distances to all other points are computed. Then, the value of the maximum geodesic distance is also the maximum geodesic length among all possible couples of points. In each step, the computation of the geodesic distance is based on the algorithm presented in Petres et al. (2005). Although in most cases an arbitrary starting point yields the correct result, there are counterexamples: for instance a rhombus such that the shortest diagonal d is longer than the edge, Figure 2.4(a). The elongation of the rhombus is the length of the largest diagonal D (segment AB in the figure). However, if P is a vertex adjacent to d , the maximum of the geodesic map is found on the opposite vertex, also adjacent to d , so that the second step yields again the maximum on d . This example can be easily extended in 3d by adding a small thickness to such a rhombus. To guarantee the correctness of the two-step procedure, it is necessary to start with a point “far enough” from the boundary. A good choice of P is the center of the ball (or of one of the balls) realizing the inner diameter. This is by definition inside the object, also for non-convex objects, and is at least the length of the inner diameter of \tilde{X} away from the boundary.

Let L_g be the elongation, then, to compare objects, we can define as in Parra-Denis et al. (2008), the **elongation index**

$$IG_g = \frac{\pi L_g^3}{6V}.$$

It equals 1 for balls and gets larger, the more elongated a particle is, where by elongated we understand thin and long, no matter how arranged in space. Note that it is a generalization of the length factor proposed in (Lantuéjoul and Maisonneuve, 1984) for 2d objects.

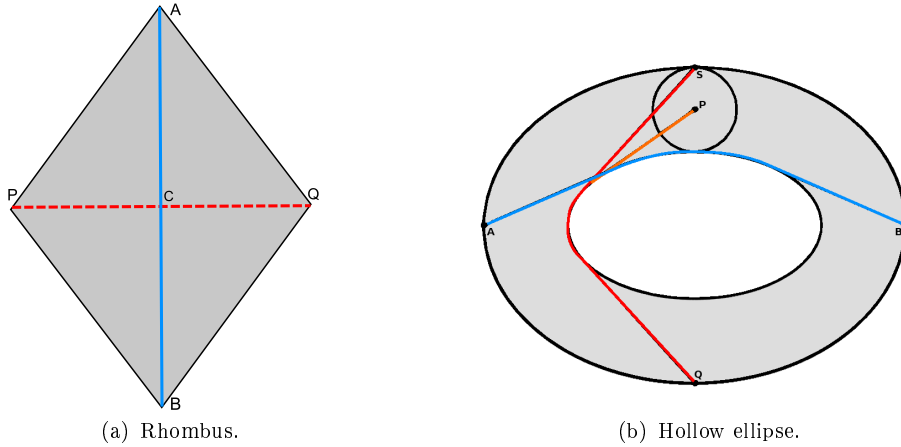


Figure 2.4: Examples of objects for which the two step procedure to estimate the elongation would fail when started from the point P .

For the sake of completeness, speaking of geodesic length it is necessary to mention *tortuosity*. This is particularly interesting for complex systems, especially porous media. The idea is to measure how twisted the object (or the medium) is by comparing geodesic and Euclidean distances. Despite its importance in many application fields, there is not a globally agreed definition. One possibility is to define the tortuosity of an object X as the ratio:

$$\text{tortuosity}(X) = \frac{L_g}{d_{\text{Feret}}},$$

where d_{Feret} is the maximal Feret diameter of X . An alternative definition is based on the ratio between elongation and the Euclidean distance between the extremes of the path realizing the elongation (Peyrega and Jeulin, 2013). For the object in Figure 2.2, these two measures have different values, nevertheless qualitatively represent the same information.

The geometric interpretation of inner diameter differs if the particle has a hole. One can take an object obtained rotating the hollow ellipse drawn in Figure 2.4(b) around one of the main axes. The resulting object can be interpreted as a hollow eggshell. Its inner diameter is the maximal thickness of the shell, which does not yield information on the core of the particle as a whole, heuristically, the size of the egg. The application of a fill-hole algorithm allows to obviate this issue filling up all the regions not connected to the background. For what concerns the elongation, the two-steps procedure might fail to return the correct value for objects with holes or tunnels. Again, we can think of the shell obtained rotating the ellipse in Figure 2.4(b) or a stretched torus such that its section is the hollow ellipse. Depending on the position of P with respect to the concavity, only a local maximum is found. Even starting with the center of a sphere realizing the maximal thickness does not suffice to find the longest path within the object. A solution is to test multiple randomized starting points in case the Euler number of the object is not 1. Furthermore, a measure of the extension of the hole in an object can be obtained by comparing inner diameter and elongation estimated on the object before and after applying a fill-hole algorithm.

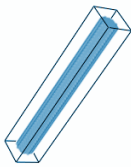
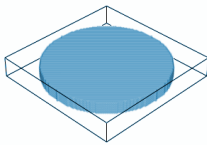
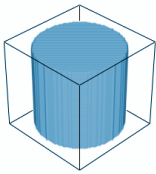
			
volume [px]	$1889 \pm 11.35\%$	$2053 \pm 3.18\%$	$2155 \pm 0.001\%$
surface area [px]	$1209.69 \pm 1.87\%$	$1582.06 \pm 6.74\%$	$895.81 \pm 3.01\%$
shape factor f_1	$0.48 \pm 0.08\%$	$0.35 \pm 7.50\%$	$0.85 \pm 4.71\%$
shape factor f_2	$0.10 \pm 3.48\%$	$0.26 \pm 8.46\%$	$0.71 \pm 5.07\%$
shape factor f_3	$0.35 \pm 2.36\%$	$0.83 \pm 8.91\%$	$0.88 \pm 4.92\%$
length [px]	$60.82 \pm 1.36\%$	$30.64 \pm 2.15\%$	$15.42 \pm 10.15\%$
width [px]	$8.59 \pm 43.17\%$	$30.18 \pm 0.58\%$	$14.87 \pm 6.18\%$
thickness [px]	$5.81 \pm 3.17\%$	$4.12 \pm 37.34\%$	$14.12 \pm 0.83\%$
max Feret diam [px]	$60.88 \pm 0.98\%$	$30.87 \pm 2.40\%$	$20.87 \pm 5.43\%$
elongation [px]	$62.55 \pm 4.25\%$	$33.79 \pm 12.07\%$	$20.60 \pm 4.04\%$
elongation index	$74.55 \pm 9.22\%$	$9.84 \pm 4.54\%$	$2.13 \pm 12.74\%$
inner diameter [px]	$6.63 \pm 10.55\%$	$3.46 \pm 15.47\%$	$13.30 \pm 4.99\%$

Table 2.1: Features of reference cylinders. The values are means of estimations on 100 randomly orientated cylinders shifted in the lattice distance. Relative error computed w. r. t. the theoretical values for radius and height (r , h), which are (3, 60), (15, 3), and (7, 14) pixels, respectively.

2.2 Analysis of the estimation error

Estimating geometric characteristics on digital images of objects bears in itself a significant approximation. For example, the sphericity of a sphere with radius 35 pixels is estimated as 0.992, while the theoretical value is 1. For this reason, it is important to systematically analyze the estimation error. In this section, we show empirically that the estimators are asymptotically unbiased for lattice distance going to zero.

As reference object, we consider a cylinder. This is a morphologically regular body which can be seen as a basic brick occurring in complex shapes, too. We sample three different aspect ratios, a prolate (diameter:height = 1:10), an oblate (5:1) and a cuboidal (1:1) cylinder, that is a fiber, a chip and a granule, respectively. In order to have cylinders in general position with respect to the lattice in the sense of (Ohser and Mücklich, 2000), we sample random rotations of the axis and random shifts in the lattice distance. In this way, the error due to the discretization chosen for the circular section of the cylinders is balanced. Table 2.1 displays the mean values of the features estimated on the cylinders with the relative error to the values computed analytically. The volume of these cylinders is about 2000 pixels. The relative error of the volume is the highest for the prolate cylinder, being about 11%. This is caused by the discretization of a circle with a radius of only 3 pixels. Further, not only the oblate and granular cylinders have larger radii, but they also have smaller height with respect to the diameter, so that the error of discretization of the circle adds up in less percent to the volume. The estimation errors for the shape factors are always under 10%. The size of the minimum volume bounding box for the fiber and the chip shows rather large relative errors, once for the width and once for the length (above 35%). This is due to the fact that the MVBB is calculated minimizing the volume and not the edge lengths of the box. Therefore, a large error in one direction might be compensated by a smaller error in another direction. Moreover, the algorithm only finds an approximation of the real MVBB. The relative errors of the volumes of the MVBB are about 29% for fiber and chip, and 15% for the granule. We calculated these errors assuming that the size of the minimum bounding box is the same as the size of the cylinders. However, if we increase the theoretical edge lengths of one pixel in each direction, the relative errors drop down to about 1% for fiber and chip, and 4% for the granular cylinder. This suggests that the lengths of the edges of the MVBB are overestimated of about one pixel in each direction. The maximal Feret diameter is estimated better than the elongation for the fiber and the chip. For these objects, moreover, the inner diameter is on average overestimated and the relative error is rather large. This shows that there is some variability in the discretizations of the cylinders depending on the orientation of the axis.

To analyze the convergence of the error we sample a wide range of volumes, namely sampling 40 sizes per class from about 50 to 20 000 pixels volume. More precisely, we sampled fibers with radius from 1 pixel (height 20 pixels) to 12 pixels (height 240); chips with radius from 3 pixels (height 1.2 pixels) to 27.5 pixels (height 11 pixels); granules with diameter equal to the height, from 4 to 22 pixels. In this way, we can reproduce the behavior of the estimators when the lattice distance goes to zero. Asymptotic convergence of the estimators of the intrinsic volumes is guaranteed by the rotations and translations within the lattice of the cylinders with increasing resolution (Ohser et al., 2002). Therefore, each cylinder was successively shifted by a random fraction of a pixel in random directions and rotated about 100 random rotations uniformly distributed in the semisphere. The characteristics estimated

on the images of each cylinder are averaged for each size and compared with the theoretical values. The results are shown in Figure 2.5. The scale on the y -axis cannot be kept constant because the maximal errors vary for each class. Adapting the scale for each cylinder type and characteristic, we can better observe how the relative errors converge.

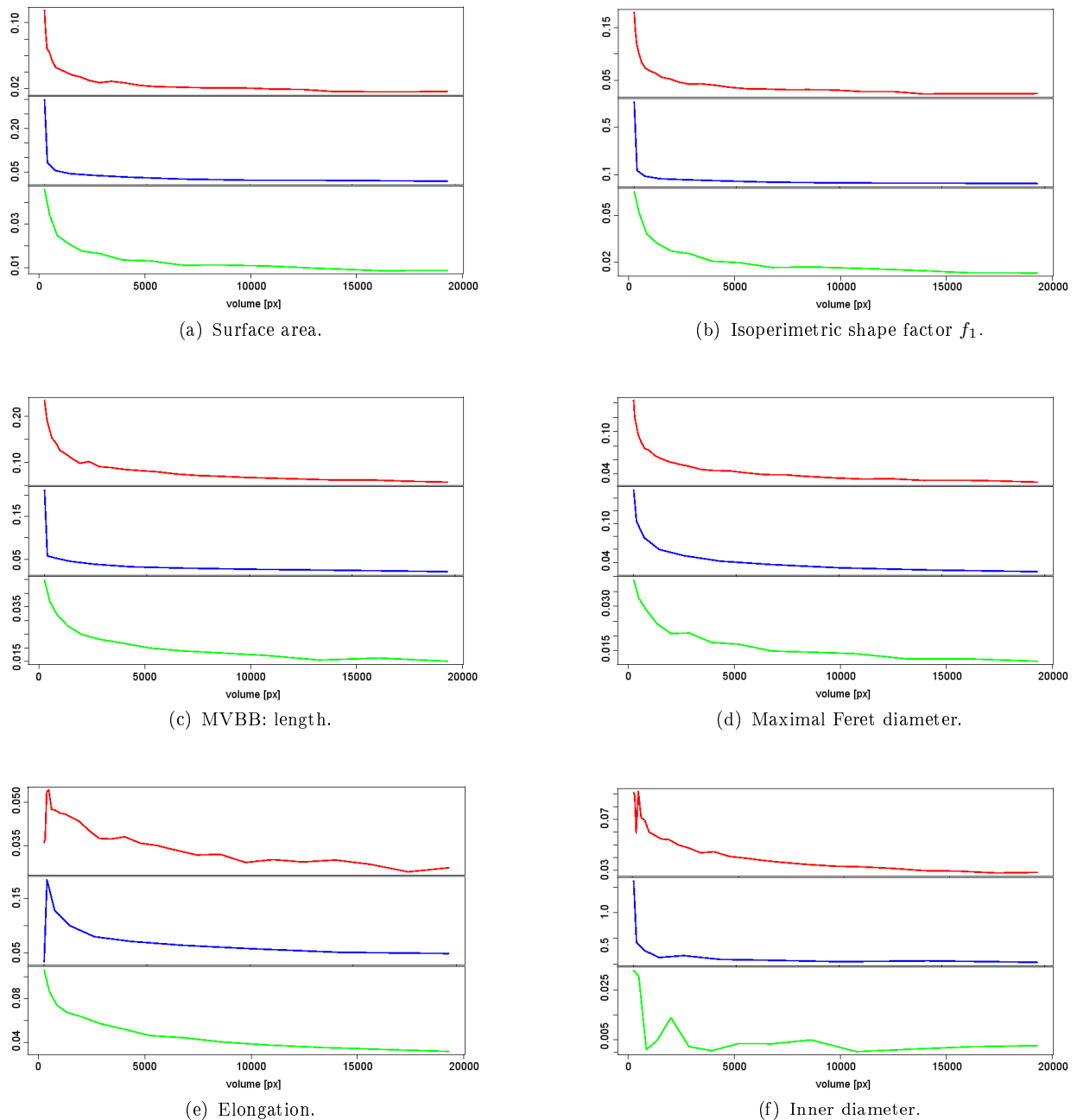


Figure 2.5: Relative error for the features estimation on three sets of cylinder with aspect ratios 1:1 (red), 10:1 (blue) and 10:1 (green), from top to bottom respectively, randomly rotated and shifted w. r. t. the lattice. The x -axis represents the volume in pixels. The scale of the y -axis is adapted to each line to allow visualization.

The relative error of theoretical and estimated surface area is shown in Figure 2.5(a).

It converges to zero as expected. The relative error for the first isoperimetric shape factor, Figure 2.5(b), shows the same trend, but with larger values. This is due to the ratio of volume and surface area, which yields a numerical error. Moreover, as Table 2.1 reveals, the error due to the estimation of the volume must be taken into account, too.

For what concerns the MVBB, only the error regarding the length is represented, Figure 2.5(c), which is on average the largest compared to width and thickness. For small objects, it is rather large (around 20% for granules and chips), but decreases significantly as resolution increases. Length, width and thickness are in most cases overestimated. This comes from the definition of the MVBB, i. e., a box containing the object completely. In the algorithm, we used a grid of 1000 nodes, yielding 840 different test directions. By increasing the fineness of the grid, the estimation can be further improved.

Maximal Feret diameter and elongation are both equal to the spatial diagonal of the cylinder. Despite being estimated with very different methods, their values differ by less than 2 pixels in the worst case. In general, the elongation is larger and the corresponding relative error, Figure 2.5(e), converges more slowly than the one of the maximal Feret diameter, Figure 2.5(d). Furthermore, it depends more strongly on the local discretization of the object, as can be seen by the oscillations of relative error.

The best estimation of the inner diameter is obtained for fibers, see Figure 2.5(f). In fact, for these long and thin cylinders, the inner diameter is the diameter of the cylinder, much smaller than the height, allowing an exact estimation for some values of the cylinder radius. Even if oscillating around zero, it is smaller than 0.5% for large enough objects (volume $> 11\,000$ pixels). For granular and chip-like cylinders, instead, the relative error is on average larger, but converging to zero as the volumes increase.

2.3 Classification

The classification proposed in ASTM F1877 (2003) distinguishes between objects with small aspect ratio, i. e., long and thin, and those with comparable dimensions. As the classification is performed by looking at the microscopic images of the particles, length and width are not rigorously defined. For a human eye, it is easy to infer the class of twisted fibers by interpreting perspective and shading effects in the images. Our goals are to generalize the classes to objects observed in three-dimensional images and to investigate strategies for automatic classification based on the features introduced in the previous section.

Let us first consider convex objects. Then, the classes in 3d can be defined as follows:

Definition 2.3.1

Let X be a convex compact body with length l , width w , and thickness t , with $l \geq w \geq t$, then

- if $l \sim w \sim t$ then X is a granule,
- if $l \sim w \neq t$ or $l \neq w \neq t$ then X is a chip,
- if $l \neq w \sim t$ then X is a fiber.

The measures of length, width and thickness correspond to those defined in Definition 2.1.2. The reference cylinders simulated for the analysis of the estimation error, Table 2.1, are representatives of these classes.

This classification was first proposed by Zingg (1935) to classify rocks. It can be easily visualized in the Zingg-diagram, Figure 2.6. In mineralogy, two measures differ if the ratio of the smaller over the bigger one is larger than $2/3$. However, this threshold may vary depending on the application field. Typically in technical cleanliness, particles are considered fibrous if their aspect ratio is 1:10.

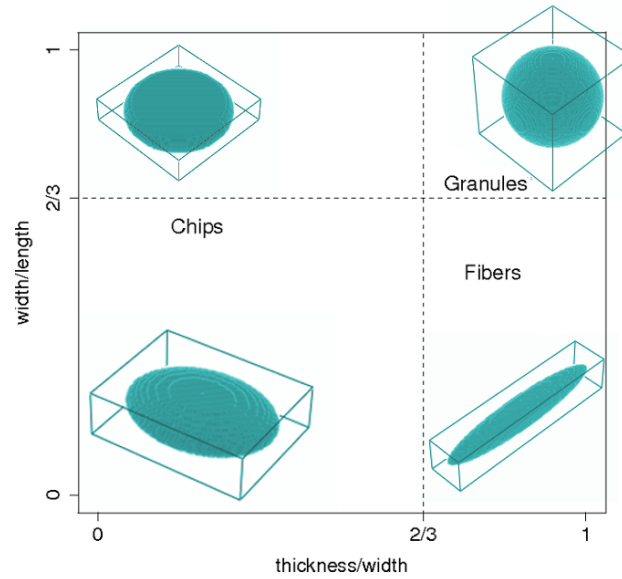


Figure 2.6: Zingg-diagram for classification based on the size and some reference particles with MVBB.

For non-convex bodies, however, the measures of the edges of the MVBB are not informative for the classification. The definition of the classes needs to be generalized to not only depend on measures based on the convex hull of the bodies. Although we do not provide formal definitions of the classes, we heuristically use the terms “granule”, “chip”, and “fiber” for arbitrary objects. The idea is to distinguish the class of an object depending on its “real” length and thickness as discussed in Section 2.1.4. Consider again the objects represented in Figure 2.3, the first particle is a chip, followed by twisted fibers. In fact, if unwound, these fibers have length ten times larger than width and thickness. It seems reasonable to use the measures of elongation and inner diameter to achieve a classification for these particles analogous to the Zingg-diagram. Define the aspect ratio as inner diameter over elongation, thus it is a number smaller or equal 1. The values for the three cylinders used as reference for fibers, chips, and granules, are 0.09, 0.20, and 0.71, respectively. They are sufficiently different. However, these are simple shapes in which the elongation is the space diagonal and two dimensions are identical. The limit of a criterion based on this index is that it only considers two dimensions to describe the three-dimensional size of particles, thus it cannot suffice to classify complex shapes.

The isoperimetric shape factors yield information on the sphericity of the objects by combining volume, surface area, and integral of mean curvature. To investigate if they can induce a reliable classification, a sample of reference particles with random size and random orientation is simulated. The sample includes about 750 objects, namely ellipsoids, cuboids,

cylinders, rounded chips, arcs of tori, and arcs of helices. Rounded chips are defined as cuboids bend around a cylinder, with various radii. Examples of these particles are those in Figure 2.3, but with different size, orientation, and more or less rounded. To classify these particles, we refer to the size of the cuboid. Arcs of tori and helices are defined as an arc of a circumference or arc of a helix, respectively, each cut at various random angles, dilated with a sphere of random radius. The length is thus computed as the curve length of the arc, while width and thickness correspond to the radius. The aspect ratios vary randomly according to the standards in technical cleanliness:

- granules: $w/l \in [0.7, 1]$, $t/w \in [0.7, 1]$;
- chips: $w/l \in [0.15, 0.6]$, $t/w \in [0.05, 1]$;
- fibers: $w/l \in [0.05, 0.09]$, $t/w \in [0.7, 1]$.

While the classes are known from the analytical description of the shapes, the features are estimated from the particles' digitized images. In Figure 2.7, graphs for the estimated isoperimetric shape factors are plotted against the increasing volume of the objects, with different colors for each class. For sufficiently large volumes, the values of the shape factors significantly differ for the classes. Based on this sample, the classification can be accomplished as follows:

- (i) $f_3 \leq 0.5$ and $f_2 \leq 0.1$ then fiber,
- (ii) if not fiber and $f_1 \leq 0.7$ and $f_2 \leq 0.4$ then chip,
- (iii) if not fiber and not chip, then granule.

For each class, we consider two shape factors so that the errors due to the estimation on digitized images can be compensated. In fact, real particles are not as smooth as the reference ones we simulated. However, since we restrict to large particles that typically do not have an inner structure, this type of error is not expected to affect the classification, as discussed in Section 2.1.2. Note that these thresholds are chosen with respect to the application to technical cleanliness. In other fields, the ratio length over width that defines a fiber, for example, could change, hence also the thresholds determining this classification should be adapted.

If the resolution is too low, the discretization errors are too high to reliably identify the shape of the object. Thus, it is not possible to correctly classify digital objects constituted by a few pixels, namely less than 64 pixels. This threshold is chosen because a cube consisting of 64 pixels has edges only 4 pixels long, thence, on average, there is not enough freedom to arrange the pixels in a wide variety of shapes. On the other hand, to rely on the estimations of the shape factors many more than 64 pixels in an object are needed. Motivated by Figure 2.7, the classification based on the isoperimetric shape factors is used only for objects with more than 400 pixels. Objects with more than 64 and less than 400 pixels are classified according to the Zingg-diagram. Indeed, in this range of resolution, concavities cannot be distinguished from errors due to discretization.

With all the features we collected, it would be possible to perform a hierarchical classification. This method is applied in Parra-Denis et al. (2008) to classify the complex shapes of

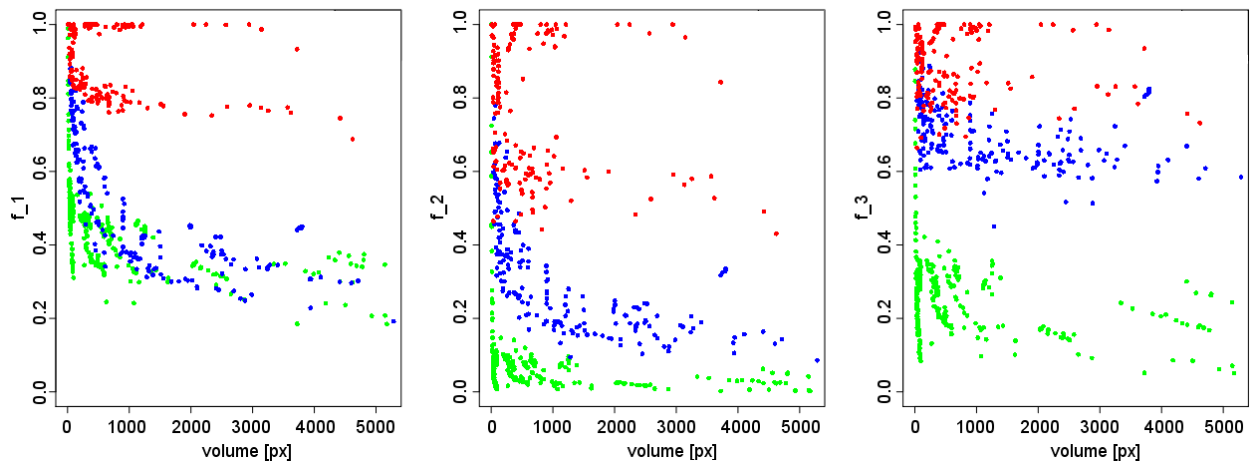


Figure 2.7: Isoperimetric shape factors, f_1 , f_2 , and f_3 , plotted against volume of the simulated particles. Each color represents a class: green for fibers, blue for chips, and red for granules.

intermetallic particles originating from the solidification process of aluminum alloys. Nevertheless, in the context of technical cleanliness we do not aim at classifying one sample. The requirements are to classify the particles according to fixed thresholds, so that samples analyzed in different laboratories can be compared.

2.4 Application to technical cleanliness

In manufacturing industry, a certain level of cleanliness is guaranteed by inspecting residual particles on the surface of mechanical components during production. Internationally agreed standards as ASTM F1877 (2003) and ISO 16232 (2007) provide the basic rules for quantitative and qualitative inspection of contaminants. The dirt particles are collected from the surface of the components on a filter membrane. While the standards require to visualize the particles with a microscope, now the membrane is rolled and imaged with micro computed tomography (μ CT). Thus, a three-dimensional image of the particles is obtained. Thresholding yields a good binarization, in fact, the membrane has a grey value very different from the particles which are usually metallic. Furthermore, the particles are typically very sparse. Often, it is convenient to include a long steel thread in the sample or to fold the filter membrane inside a steel cylinder. The luminosity of steel in the μ CT helps calibrating the grey values to determine the material composition of the dirt particles. A volume rendering of a membrane with some particles is displayed in Figure 2.8.

We analyze a sample of dirt particles collected from the surface of a car engine part. It consists of 1061 particles. The mean volume is $2.49 \cdot 10^6 \mu\text{m}^3$ (259 pixels). Applying the thresholds suggested in the previous section, the particles are labeled as 'small', 'medium', and 'large' depending on their number of pixels, this results in 469 small, 406 medium, and 186 large particles. The small particles will not be analyzed further. We classify medium particles according to the minimum volume bounding box, whereas large ones are classified according to the isoperimetric shape factors. Table 2.2 displays the characteristics of three

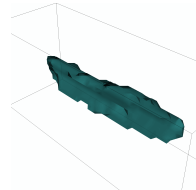
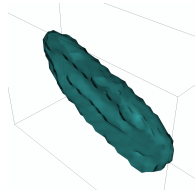
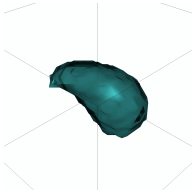
			
pixel size = 9.88 μm	fiber	chip	granule
volume [px]	823	2968	1023
volume [μm^3]	793 726	2 862 429	986 612
Euler number	1	1	1
shape factor f_1	0.48	0.56	0.86
shape factor f_2	0.19	0.33	0.73
shape factor f_3	0.44	0.69	0.89
length [μm]	341.18	393.81	149.05
width [μm]	86.44	160.56	132.93
thickness [μm]	49.14	74.44	91.45
elongation [μm]	340.86	398.56	166.38
elongation index	26.12	11.58	2.44
inner diameter [μm]	4.47	7.21	9.17
convexity factor	0.91	0.95	0.97

Table 2.2: Features of three large particles from the sample analyzed in Section 2.4. Images and computation of characteristics with MAVIparticle (Fraunhofer ITWM, Department of Image Processing, 2012).

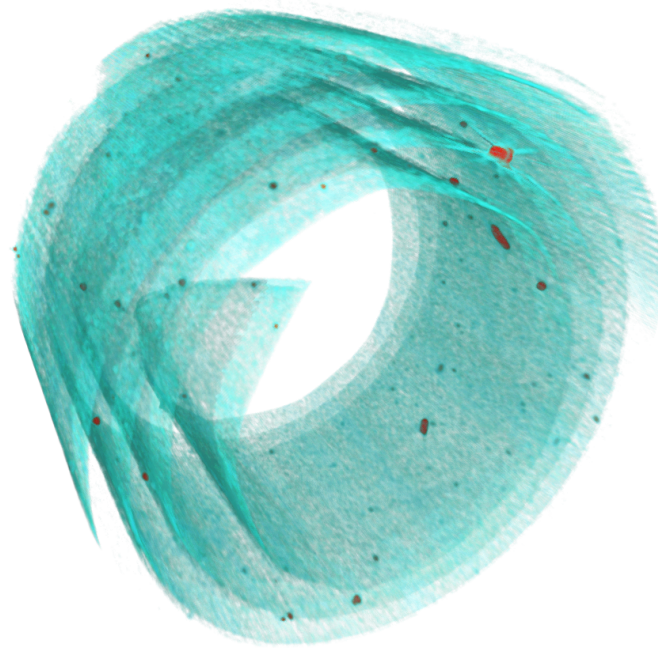


Figure 2.8: 3d rendering of a sample of dirt particles (red) on the rolled filter membrane (blue). Tomographic image realized by RJI Micro&Analytic with a SkyScan device. Pixel size = $9.88\mu\text{m}$. Image size $10.86\times 10.86\times 2.96$ mm. Visualization by MAVI (Fraunhofer ITWM, Department of Image Processing, 2012).

of the largest particles in the sample, one for each class.

Provided that for technical cleanliness all the features convey useful information, it is however interesting to analyze if they are correlated. The correlation is analyzed for the features estimated on large particles of the current sample and from other samples, so that 486 particles are investigated. The pairwise covariance matrix is displayed in Figure 2.9. Volume and surface area are linearly correlated, implying the correlation of the isoperimetric shape factors f_2 and f_3 . Also the correlation of length and elongation is linear, as well as thickness and inner diameter. This suggests that most of the particles have a rather regular shape: the size of the MVBB suffices to determine the real length and thickness of the particles. Among the other features, no significant correlation occurs.

In Figure 2.10(a), the aspect ratios of the MVBB of the medium particles are represented in the Zingg-diagram. The thresholds are imposed by technical cleanliness requirements: thickness over width smaller than $2/3$ means comparable dimensions and length over width smaller than $1/10$ defines fibers. With these thresholds, there are 216 granular particles, 190 chips and no fibers among the medium particles in the sample. For what concerns the large particles, instead, we consider the isoperimetric shape factors. In Figure 2.10(b), f_1 is plotted against the volume. The classification, which takes into account all three isoperimetric shape factors, is represented by the colors. There are 9 fibers, 66 chips and 111 granules. The largest particles in the sample are fibers, as typical in residual dirt.

Gathering all the data regarding medium and large particles, we see that the sample is composed of 55.2% granules, 43.3% chips, and only 1.5% fibers. Though fewer, fibers constitute 13.7% of the total volume.

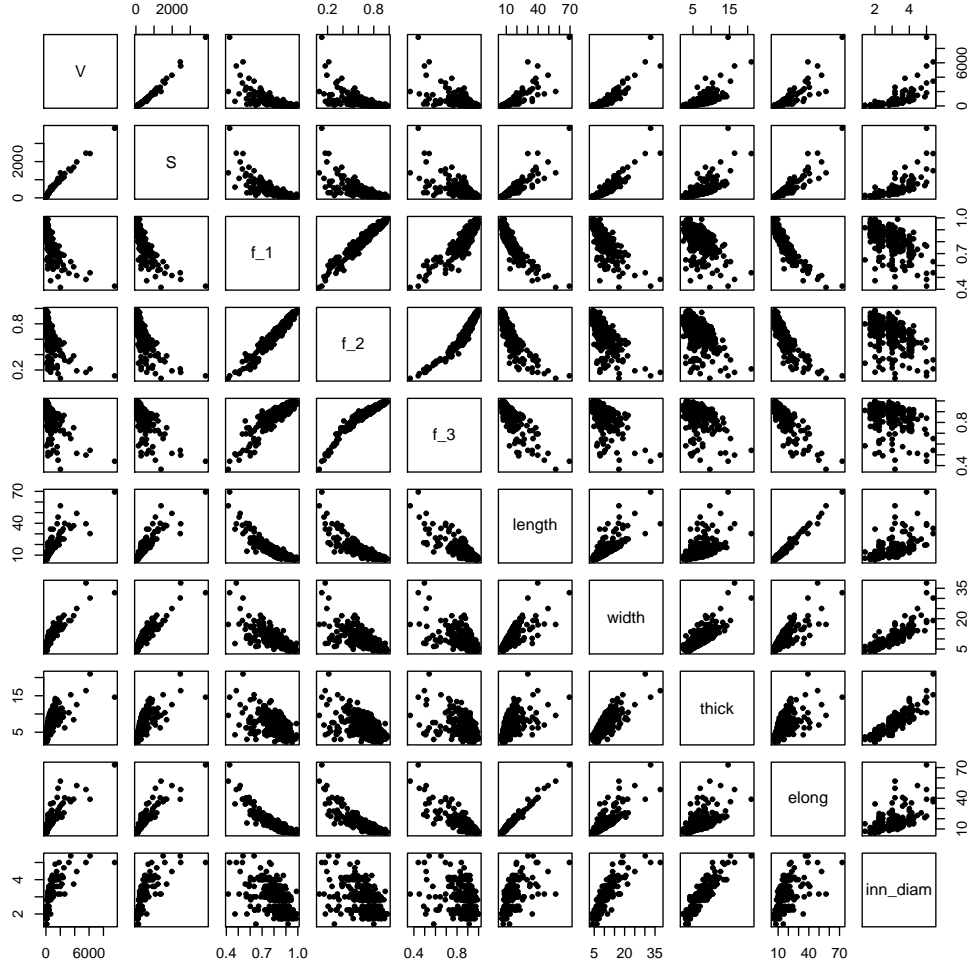
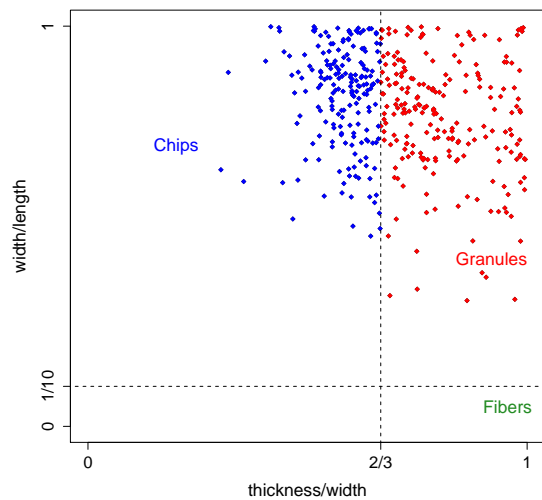


Figure 2.9: Correlation matrix of volume V , surface area S , isoperimetric shape factors f_1 , f_2 , and f_3 , MVBB length, width, and thickness, elongation, and inner diameter on 486 large particles from samples of dirt particles. All measurements in pixels assuming lattice spacing = 1.

Once the classification is achieved, the sample can be further characterized by means of the other features. All particles have Euler number equal to 1, before and after applying a fill-holes algorithm. This means that no particle has holes or tunnels. Moreover, it is interesting to investigate the degree of straightness of the large fibers in the sample: length and elongation or thickness and maximal local thickness can be compared to see if the fibers are twisted. If the convexity factor is much smaller than 1, then the fiber is curved, the more it is, the larger the elongation index will be.

Observing Table 2.2, we see values for three representatives of the classes. The classification is based on the isoperimetric shape factors. The elongation index is typically different for each particle, being 10 times larger for the fiber than for the granule. None of the particles presents a significant concavity. Indeed, though the fiber has a rather rough surface, the convexity factor is equal to 0.91.



(a) Zingg-diagram of the medium particles.

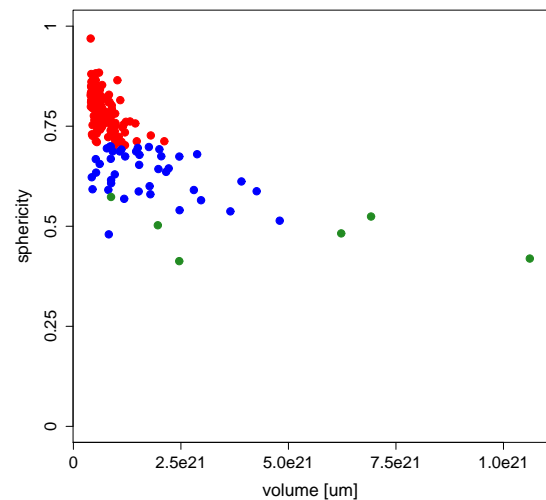
(b) Isoperimetric shape factor f_1 of large particles plotted over the volume.

Figure 2.10: Classification of dirt particles in the sample. Each color represents a class: green for fibers, blue for chips and red for granules.

2.5 Discussion

We defined a rich set of parameters describing size and shape of objects in 3d. Moreover, we provided methods to estimate these features based on a digital representation of the objects. The analysis of errors showed that discretization and resolution play crucial roles in the goodness of estimation. We proposed a method to classify objects into fibers, chips and granules according to the requirements of technical cleanliness. We showed that only few parameters suffice to identify the class of an object. Besides, the classification can be obtained automatically with respect to the thresholds we suggested.

In the following chapters, we will deal with more complex structures. Nevertheless, the focus will be on the geometric characterization based on 3d images. Therefore, we will still make use of the parameters defined in this chapter.

Chapter 3

Models for fiber systems

Fiber systems occur in a diverse range of materials, both natural and manufactured. Composite materials, as fiber reinforced polymers or reinforced concrete, are specifically engineered to maximize the performance. As the highest stiffness corresponds to the axis direction, fibers are inserted in the matrix material with an anisotropic orientation distribution (Mayer, 1993; Köpplmayr et al., 2013). Cellulose pulp composites as paper or medium density fiber boards (MDF) are particularly challenging materials to analyze and model. The relatively thin sheets are obtained by pressing together the pulp of cellulose fibers. This process results in a high density structure composed of broken fibers, which typically lie in the plane perpendicular to the direction of pressing. We will inspect a sample of MDF in detail in Section 3.4. Broadly speaking, we can identify two main steps in the analysis and modeling of fiber systems: the characterization of the structures based on image data and the selection of the parameters of the best-fitting model.

First of all, estimation of geometric characteristics based on image analysis is hampered by the difficulty to segment the single fibers, even in high resolution images. Thus, the methods developed in the previous chapter cannot be applied for complex fiber systems. In this context, the geometric characterization of the fibers have to rely only on local information (Altendorf and Jeulin, 2011a; Lux et al., 2006). Techniques to estimate thickness and length distribution, and curvature are developed for both binary and grey value images. Additional to shape and size characterization, the orientation distribution is an important feature to estimate from image data. Details to fit the orientation distribution to anisotropic fiber systems are given in Section 3.1. Furthermore, anisotropy can affect the possibility of full analytical description of the model. Typically, fibers are modeled either as cylinders with finite or infinite length (Peyrega, 2010; Redenbach and Vecchio, 2011; Schladitz et al., 2006), as dilated curved lines (Faessel et al., 2005; Gaiselmann et al., 2013), or as chains of balls (Altendorf, 2011). In all these cases, the cross section is modeled with a circle, thus it is isotropic. Nonetheless, some fibers feature polygonal cross sections. For instance, wood fibers in plywood have typically a rectangular cross section, whereas triangular cross sections in polyester fibers improve the thermal absorption of textiles (Karaca et al., 2012). As polygons are not isotropic, changing the shape of the cross section in the models requires the fitting of another orientation distribution. However, very high resolution is needed to reliably estimate which shape fits better to the cross section of the fibers. Methods to estimate the orientation distribution of the cross sections from images still need to be investigated.

Fiber models can be divided into two classes: models without interaction and models

with interaction among the fibers. Interaction yields, for instance, the possibility of generating systems of non-overlapping fibers. Although non-overlapping and interaction are physically motivated, they cannot be observed nor measured in images with low resolution. This is one of the reasons to consider models without interaction. Another reason is the limited number of free parameters defining models in this class. We mainly focus on models without interaction and consider two classic ones already investigated by Matheron (1975): the *Boolean model* (Section 3.2.1) and the *Poisson cylinder process*, or *Poisson process of dilated lines* (Section 3.2.2). With suitable assumptions, only few characteristics of the fiber system suffice to infer the model parameters. These characteristics are the intrinsic volume densities, see Section 1.2.2. They can be estimated from a binarized image of the fiber system adapting the techniques mentioned in Section 2.1.1. We will illustrate under which assumptions the model parameters are analytically linked to these quantities. We are particularly interested in anisotropic Poisson cylinder processes. For this model, we will extend results valid only for circular cross sections to polygonal cross sections. Concerning models with interaction (Section 3.3), we will shortly introduce the main characteristics of *random sequential adsorption* (RSA), *fiber packing*, and *sedimentation*. While RSA is usually applied with cylinders, the other two models are based on a more sophisticated model for the fibers (Altendorf, 2011). This yields the growth of both the set of parameters of the model and of the number of characteristics to be estimated from the images. References for further details are given.

Difficulties of the analysis and modeling of fibers are well shown by the sample of MDF investigated in Section 3.4. The fibers are highly anisotropic and with a thickness of about $32\ \mu\text{m}$, which are represented by only a few pixels in the image. Boolean models and Poisson cylinder processes with circular and squared cross sections are fitted to the sample. Comparing the characteristics of some realizations, we will discuss which is the best choice according to the information we can extract from the image data.

We now recall the intrinsic volumes of compact cylinders with circular, triangular, and squared cross section. Let V be the volume, S the surface area, and \bar{b} the mean width, then if Z is a cylinder with circular cross section with radius r and length h , we get

$$V(Z) = \pi r^2 h, \quad S(Z) = 2\pi r(r + h), \quad \bar{b}(Z) = \frac{1}{2}(\pi r + h). \quad (3.1)$$

If Z is a cylinder having an equilateral triangle of edge length a as cross section, it holds that

$$V(Z) = \frac{\sqrt{3}}{4}a^2 h, \quad S(Z) = \frac{\sqrt{3}}{2}a^2 + 3ah, \quad \bar{b}(Z) = \frac{3}{4}a + \frac{1}{4}h, \quad (3.2)$$

whereas for a squared cross section of edge a , it holds

$$V(Z) = a^2 h, \quad S(Z) = 2a(a + 2h), \quad \bar{b}(Z) = a + \frac{1}{2}h. \quad (3.3)$$

In all cases, the Euler characteristic is equal to one. In the sense of Hadwiger's Theorem 1.2.2, the intrinsic volumes constitute a complete set of functionals describing cylinders. Moreover, from their knowledge, the mean height and thickness of the cylinders can be calculated.

3.1 Orientation distribution

A coarse estimation of the orientation distribution of a fiber system is obtained by measuring the projections on the 13 directions induced by the lattice in 3d (Section 1.1). More sophisticated methods have been developed to account for the information in grey value images. The idea of Gaussian filters is based on sampling a set of directions in each pixel: the direction that gives the highest filter response is the estimate of the local orientation (Robb et al., 2007; Wirjadi et al., 2008). As it is a local method, it is also well defined for curved fibers. However, it has the drawback of a limited number of directions tested. This problem is overcome by estimating the main fiber direction in a pixel with the minimum eigenvector of the Hessian matrix (Redenbach et al., 2012a). The second order partial derivatives of the smoothed grey value image are calculated in each pixel. The local fiber orientation is then estimated as the eigenvector corresponding to the smallest eigenvalue. In fact, this corresponds to the direction of least grey value variation. A method based on mathematical morphology is proposed in Altendorf and Jeulin (2011a). The main axis direction is locally estimated via the axis of inertia. With both methods, a volume-weighted continuous orientation distribution is estimated from the image data.

Once an empirical orientation distribution is available, the next step is to model it. The *von Mises-Fisher* (or *Fisher*) *distribution* (vMF) can be interpreted as the generalization to the sphere of the Gaussian distribution on the line (Fisher et al., 1987). It depends on two parameters: the mean μ , i. e., the preferred direction, and the concentration parameter $\kappa > 0$, which determines the width of the distribution around μ . It is unimodal and rotationally symmetric. For $\kappa \rightarrow 0$, the distribution tends to be uniform on the sphere, i. e., isotropic, whereas for $\kappa \rightarrow \infty$ it converges to the point distribution in μ . Multimodal asymmetric distributions can be achieved by mixtures of von Mises-Fisher distributions. While the preferred direction can be estimated as the mean of the empirical distribution, it is not possible to derive an analytical expression for the estimator of the concentration parameter of vMF. Alternative approaches to estimate the parameters of unimodal and multimodal vMF distributions are outlined in Banerjee et al. (2005) based on maximum-likelihood estimates. In the multimodal case, the number of mixtures must be chosen by the user. Comparing the goodness of fit of the distributions found with different numbers of clusters yields a validation for the model.

Another orientation distribution particularly helpful in materials science applications is the so-called β -distribution (Schladitz et al., 2006). Its benefit is that, depending on only one parameter $\beta > 0$, it can represent three qualitatively different distributions: isotropic ($\beta = 1$), girdle ($\beta > 1$), i. e., fibers oriented around the equator, or fibers oriented around an axis ($\beta < 1$). The value of β also determines the concentration of the distribution around the equator or around the axis. The probability density function of the β -distribution with axis of symmetry μ corresponding to the z -axis is

$$f(\theta, \phi) = \frac{\beta \sin \theta}{4\pi(1 + (\beta^2 - 1) \cos^2 \theta)^{3/2}}, \quad \theta \in [0, \pi), \quad \phi \in [0, 2\pi),$$

where θ, ϕ are the polar coordinates representing a direction. Of course, the axis of symmetry can be rotated arbitrarily. As for the von Mises-Fisher distribution, it is possible to consider mixtures of β -distributions. Different types of distributions can be combined, for instance summing a girdle distribution, with a distribution with one preferred direction, or considering

mixtures of girdle distributions with different axes of symmetry. Even in the unimodal case, an analytical estimator for β could not be found. Again, maximum-likelihood estimates are investigated to estimate β and μ from empirical data (Zhang, 2013). In the case of mixtures, previous knowledge on the number and types of distributions improves the estimation of the axes μ_i and of the parameters β_i . The number of distributions must be given as input.

Additional spherical probability distributions are treated in Fisher et al. (1987) and Zhang (2013), which provides a comparison between the β -distribution and other classic ones.

3.2 Models without interaction

This class of models is based on fibers which are independent from each other. When generating realizations of these models in compact windows, the order in which they are inserted does not affect the final configuration. The absence of interaction among fibers yields systems of overlapping fibers which are computationally fast to simulate. In particular, we introduce two models which strongly rely on the independence property of Poisson point processes: the Boolean model and the Poisson cylinder process. They both benefit from an analytical description that facilitates model fitting, at least under some assumptions. As it is often impossible to precisely estimate the real interaction among fibers, these classic models are still widely used in applications.

We will give definitions in general dimension, sometimes exploit 2d for illustration and investigate the main results only in 3d, as we aim to model materials in the real world. Detailed theoretical analysis of the general case can be found in (Schneider and Weil, 2008).

3.2.1 Boolean model

The Boolean model is the most famous representative of *germ-grain processes*. Models in this family can be interpreted as marked point processes (Definition 1.2.9), where the ground process is the germ process and the mark space M is contained in \mathcal{F} . The marks are called grains. Germ-grain processes are a natural model for systems of random independent objects. Several examples of materials modeled with Boolean models are presented in Jeulin (2011) and references therein. Beside serving as models for granular structures, Boolean models can be exploited to simulate complex patterns in multiphase materials (Savary et al., 1999). Although the interpretation is different, the same analytical results can be applied. A Boolean cylinder model is fitted to samples of medium density fiber board in Peyrega (2010). The insulation properties of the material are analyzed based on realizations of the model. Also the model presented in Faessel et al. (2005) can be interpreted as a Boolean model with compact non-convex grains. Fibers in that case are not cylinders but are obtained by dilating a curved line with a given random radius. The construction of the medial axis of a fiber depends on length, curvature and random orientation distribution. Each fiber is inserted in the observation window independently of the others. The model is fitted only to low density materials, thus overlappings are rare. This model is used to test the thermal conductivity of low density fiber boards. In simulations, a special mechanical behavior is assigned to the surface of contact.

We will restrict to compact grains. Some realizations of Boolean models of cylinders with varying parameters of the orientation distribution and circular and polygonal cross sections

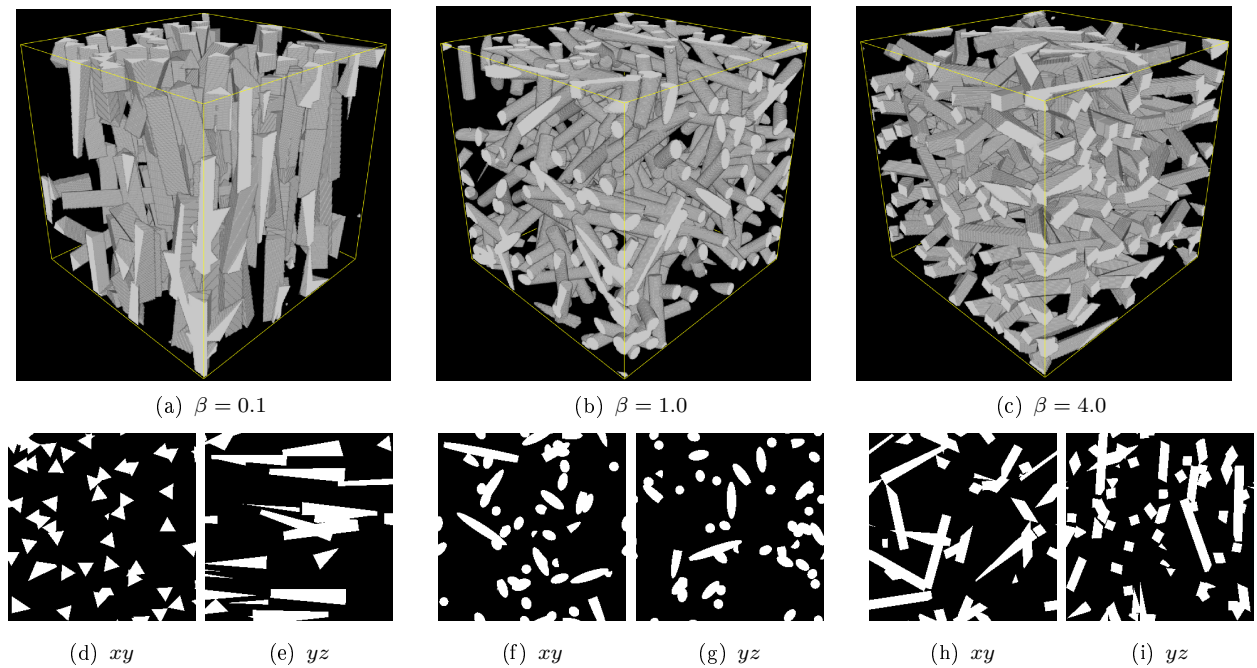


Figure 3.1: Realizations of Boolean models with different cross sections and parameters of the β -orientation distributions. Isotropic distribution of the cross sections. Volume fraction about 15%, length 120 pixels, Left: $\beta = 0.1$, triangular cross section with diameter of the equivalent area circle 15 pixels. Center: $\beta = 1$, circular cross section with diameter 15 pixels. Right: $\beta = 8$, squared cross section with edge length 15 pixels. Image size $300 \times 300 \times 300$ pixels.

are displayed in Figure 3.1.

Definition 3.2.1 (Boolean model)

Let $\Phi = \{x_1, x_2, \dots\}$ be a Poisson point process in \mathbb{R}^d (*germ process*). Let the *grains* X_1, X_2, \dots be a sequence of random compact sets with center of the circumscribed sphere in the origin, with non empty interior, mutually independent and identically distributed as X_0 and independent of Φ . Then the *Boolean model* Ξ with *typical grain* X_0 is

$$\Xi = \bigcup_{i=1}^{\infty} (X_i + x_i).$$

The properties of the union of grains strongly depend on the properties of the underlying germ process. For instance, the Boolean model is stationary if the underlying point process is stationary. In this case, the intensity measure of the Poisson point process is absolutely continuous with respect to the Lebesgue measure. Moreover, the intensity of the underlying point process λ is also the intensity of the Boolean model.

As discussed in Section 1.2.2, the intrinsic volume densities are a complete set of functionals to describe unions of bodies. Furthermore, under some conditions, the intrinsic volume densities of the union of grains in Boolean models can be expressed in terms of the geometric properties of the typical grain.

Theorem 3.2.2 (Miles' formulae)

Let Ξ be a stationary isotropic Boolean model with intensity $\lambda > 0$ and typical convex grain X_0 and with intrinsic volume densities $V_V = V_{V,3}(\Xi)$, $S_V = 2V_{V,2}(\Xi)$, $M_V = \pi V_{V,1}(\Xi)$, and $\chi_V = V_{V,0}(\Xi)$. Let $\bar{V} = \mathbb{E}[V_3(X_0)]$, $\bar{S} = 2\mathbb{E}[V_2(X_0)]$, and $\bar{b} = \frac{1}{2}\mathbb{E}[V_1(X_0)]$ be the mean values of the intrinsic volumes of X_0 . Then it holds

$$V_V = 1 - e^{-\lambda\bar{V}}, \quad (3.4)$$

$$S_V = e^{-\lambda\bar{V}}\lambda\bar{S}, \quad (3.5)$$

$$M_V = e^{-\lambda\bar{V}}(2\pi\lambda\bar{b} - \frac{\pi^2\lambda^2}{32}\bar{S}^2), \quad (3.6)$$

$$\chi_V = e^{-\lambda\bar{V}}(\lambda - \frac{\lambda^2}{2}\bar{b}\bar{S} + \frac{\pi\lambda^3}{384}\bar{S}^3). \quad (3.7)$$

Suppose we are observing a realization of a Boolean model Ξ in a compact convex window W , then $V_{V,k}$ are well defined for $k = 0, \dots, 3$. Moreover, it is possible to estimate the intrinsic volume densities of Ξ by means of image analysis techniques. Thus, the lefthand sides of Equations (3.4)–(3.7) are known. The system can be solved to find the intensity of the model and the mean characteristics of the typical grain. However, we are solving a non-linear system, thus the solutions are affected by numerical errors. Besides, the estimations of the intrinsic volume densities from images yield an error due to the discretization. Therefore, in applications it is preferable to use a set of analogous equations which contain numerical corrections (Ohser et al., 2009a).

The Miles formulae allow to automatically deduce the intensity of the process and the mean characteristics of the grains starting from quantities estimated from the images. These formulae are a special case of Theorem 9.1.3 of Schneider and Weil (2008) for additive and continuous functionals. Due to Hadwiger's theorem, regular functionals other than the intrinsic volumes only carry redundant information. Therefore, the Miles formulae also yield that the first moments of the characteristics of the grains are the only information that can be extracted from the intrinsic volume densities of the process. Yet, we can determine only moments of the first order and not deduce information about the whole distributions of the geometric characteristics.

There are three assumptions for the validity of the Miles' formulae: stationarity, isotropy and convexity of the grains. The weakest is the convexity of the grains, in fact, the same results hold for polyconvex grains, given they comply with an additional integrability condition (Schneider and Weil, 2008). Dropping solely the isotropy condition, then only Equations (3.4) and (3.5) hold. However, even in the case of circular cross section, these two do not suffice to extract both the intensity of the germ process and the characteristics of the grains. In Section 3.4, we will apply them to fit Boolean models of cylinders with circular and squared cross section to a strongly anisotropic fiber system. To estimate the intensity of the models from the Miles' formulae, we will extract the mean fiber thickness by other means.

For generalized versions of the Miles' formulae in dimension d for anisotropic systems, we refer the interested reader to Schneider and Weil (2008, Theorem 9.1.5). Moreover, Weil (2001) analyzes in details lower dimensions. In the three-dimensional case, formulae based on mixed volume densities of the typical grain are stated. Nevertheless, not only they are more difficult to handle in real applications, but they introduce more unknowns and thus do not suffice to determine the mean characteristics of the grains either. Weil (2001) treats also the case of non-stationary Boolean models. Although some theoretical results are found, it

is not possible to employ them for estimating the model parameters directly from quantities estimated in images.

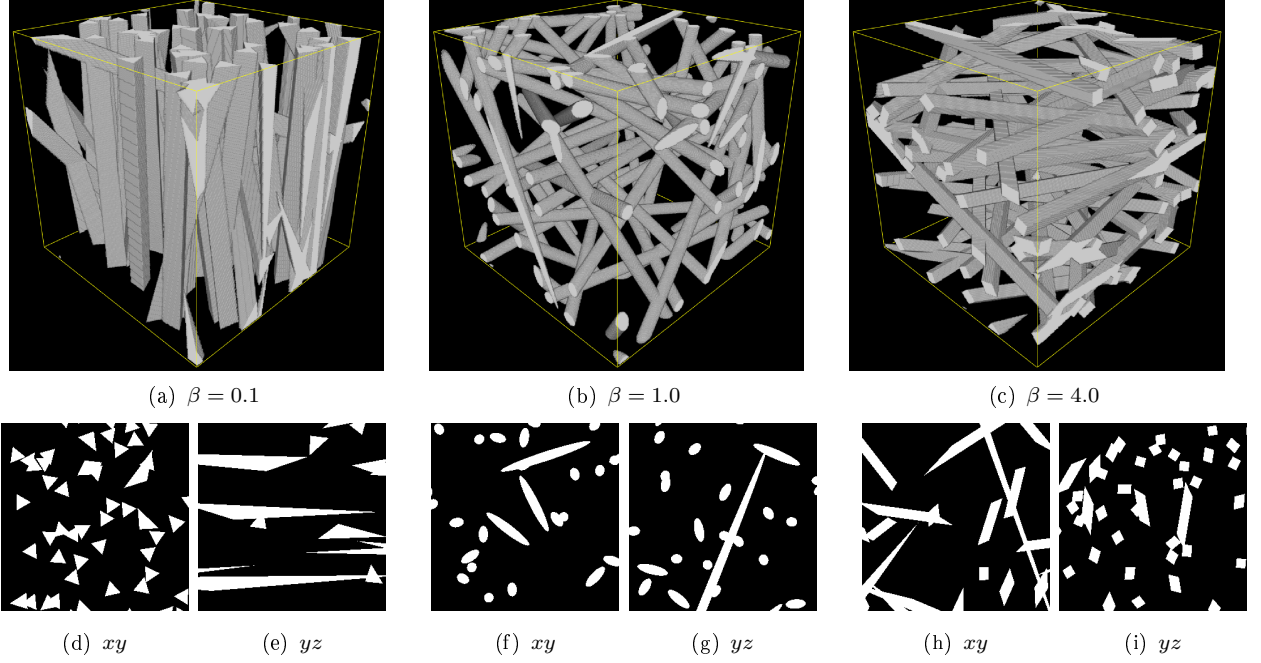


Figure 3.2: Realizations of Poisson processes of cylinders with different cross sections and parameters of the β -orientation distributions. Isotropic distribution of the cross sections. Volume fraction about 12%. Left: $\beta = 0.1$, triangular cross section with diameter of the equivalent area circle 15 pixels. Center: $\beta = 1$, circular cross section with diameter 15 pixels. Right: $\beta = 8$, squared cross section with edge length 15 pixels. Image size $300 \times 300 \times 300$ pixels.

3.2.2 Poisson cylinder process

We now abandon compact sets and consider generalized cylinders. Such a cylinder is defined as a line dilated with a compact structuring element, hence the name process of dilated lines (Weil, 1987). Poisson cylinder processes are defined as Poisson point processes with value in the space of generalized cylinders. They are a natural model for systems of long fibers. Schladitz et al. (2006) fitted a Poisson cylinder process to a highly anisotropic non-woven fiber material to analyze the acoustic properties of the material. Examples of realizations of stationary Poisson cylinder processes with different cross sections and orientation distributions are displayed in Figure 3.2.

Definition 3.2.3

Let $G(k, d)$ be the Grassmannian manifold of all non-oriented k -dimensional linear subspaces of \mathbb{R}^d . If $L \in G(k, d)$ and $K \subset L^\perp$, $K \in \mathcal{R}$, the convex ring, such that the center of the circumscribed sphere is in the origin, then the Minkowski sum

$$Z = L \oplus K$$

is a *cylinder* with direction space $L(Z) = L$ and cross section (or base) $K(Z) = K$. Moreover, \mathcal{Z}_k^0 is the set of all cylinders with k -dimensional direction space and with cross section centered in the origin. The set of all cylinders with k -dimensional direction space in \mathbb{R}^d is $\mathcal{Z}_k = \{Z + x : Z \in \mathcal{Z}_k^0, x \in \mathbb{R}^d\} \subset \mathcal{F}$.

Analogously to the definitions given on \mathbb{R}^d in Section 1.2.3, a measure φ on \mathcal{Z}_k is locally finite if

$$\varphi(\{Z \in \mathcal{Z}_k : Z \cap C \neq \emptyset\}) < \infty$$

for compact sets $C \in \mathbb{R}^d$. A locally finite measure φ such that $\varphi(Z) \in \mathbb{N}_0 \cup \{\infty\}$ for all $Z \subseteq \mathcal{Z}_k$ is a counting measure on \mathcal{Z}_k . We call $\mathcal{N}(\mathcal{Z}_k)$ the set of locally finite counting measures on the space of cylinders \mathcal{Z}_k . $\mathcal{N}(\mathcal{Z}_k)$ is supplied with the induced σ -algebra $\mathcal{N}(\mathcal{Z}_k)$. Now, we have all the elements needed to rigorously define a generalized point process:

Definition 3.2.4 (Poisson cylinder process)

Let Φ be a point process in the space \mathcal{Z}_k , that is, a Borel-measurable map on a probability space $(\Omega, \mathcal{A}, \mathbb{P})$ with values in $\mathcal{N}(\mathcal{Z}_k)$ furnished with the σ -algebra $\mathcal{N}(\mathcal{Z}_k)$. Then Φ is a *cylinder process* with intensity measure Λ such that $\Lambda(B) < \infty$ for all Borel sets $B \subset \mathcal{Z}_k$. If Φ is a Poisson point process on \mathcal{Z}_k , then $\Phi(B)$ has Poisson distribution with mean $\Lambda(B)$ for all Borel sets $B \subset \mathcal{Z}_k$ and Φ is called *Poisson cylinder process*.

We will restrict to $d = 3$ and $k = 1$, that is, classic cylinders with infinite length. For simplicity, we will write \mathcal{Z} for \mathcal{Z}_k and so on. Moreover, we will only consider simple Poisson processes. If Φ is stationary, then also Λ is invariant to translations, whereas if Λ is stationary, the Poisson cylinder process is said to be weakly stationary. The same holds for isotropy. If Φ is stationary, the intensity measure can be decomposed (Weil, 1987). Let $i : (x, Z) \mapsto x + Z$ for $x \in \mathbb{R}^3$ and $Z \in \mathcal{Z}^0$, then there exist $\lambda > 0$ and a probability measure θ on \mathcal{Z}^0 such that

$$\Lambda(i(A \times C)) = \lambda \int_C V_2^{L(Z)}(A) \theta(dZ) \quad (3.8)$$

for all Borel sets $A \subset \mathbb{R}^3$ and all $C \subset \mathcal{Z}^0$, with $V_2^{L(Z)}$ being the Lebesgue measure restricted to $L(Z)^\perp \subset \mathbb{R}^2$. λ is the *intensity* and θ is the *shape distribution* of Φ .

The union set of a Poisson cylinder process can also be interpreted as a generalization of the Boolean model with non-compact grains (Ohser and Schladitz, 2009). The union of the cylinders $\Xi = \cup_{Z \in \Phi} Z$ is a random closed set which is almost surely locally finite. Therefore, the intrinsic volume densities of a Poisson cylinder process observed in a compact window are well defined. As for Boolean models, also in this case it is possible to express these densities via the mean values of the cylinder characteristics (Ohser and Mücklich, 2000; Weil, 1987; Miles, 1976). Additional assumptions are necessary.

Theorem 3.2.5 (Miles' formulae)

Let Ξ be the union set of a stationary isotropic Poisson cylinder process with intensity λ and constituted by cylinders with one dimensional direction space in \mathbb{R}^3 and circular cross section. Define V_V , S_V , M_V and χ_V the intrinsic volume densities of Ξ . Let \bar{A} be the mean

cylinder cross section area and \bar{C} the mean circumference. Then it holds

$$V_V = 1 - e^{-\lambda \bar{A}}, \quad (3.9)$$

$$S_V = e^{-\lambda \bar{A}} \lambda \bar{C}, \quad (3.10)$$

$$M_V = e^{-\lambda \bar{A}} \left(\pi \lambda - \frac{\pi^2 \lambda^2}{32} \bar{C}^2 \right), \quad (3.11)$$

$$\chi_V = e^{-\lambda \bar{A}} \left(-\frac{\lambda^2}{4} \bar{C} + \frac{\pi^2 \lambda^3}{96} \bar{C}^3 \right). \quad (3.12)$$

Assuming that the observed sample is a realization of a stationary isotropic Poisson process of cylinders allows to estimate the mean geometric characteristics of the cylinders and the intensity of the process.

An extensive treatment of Poisson processes of dilated flats in \mathbb{R}^d is presented in Weil (1987). More recently, Hoffmann (2007a,b) focused on anisotropic non-stationary Poisson processes. He expresses the intrinsic volume densities depending on mixed volumes of the process observed on intersections with lower dimensional hyperplanes. His results are highly theoretical and cannot be employed in model fitting. Stationary anisotropic Poisson cylinder processes are the subject of the work of Spiess and Spodarev (2010). Formulae for the capacity functional, the covariance, and the specific surface area for stationary anisotropic cylinder processes with polyconvex cross sections are presented. In particular, we can adapt the formula for the density of the surface area to facilitate model fitting.

From now on, we follow the notation of Spiess and Spodarev (2010). We denote by γ_A the *set covariance* or *covariogram* or *covariance function* (Ohser and Mücklich, 2000) of a measurable set $A \subset \mathbb{R}^d$, which is defined as

$$\gamma_A(x) = V_d(A \cap (A - x)),$$

for $x \in \mathbb{R}^d$. The directional derivative in the origin is defined as

$$\begin{aligned} \gamma'_A(0, u) &= \lim_{t \rightarrow 0} \frac{\gamma_A(tu) - \gamma_A(0)}{t} \\ &= \lim_{t \rightarrow 0} \frac{V_d(A \cap (A - tu)) - V_d(A)}{t}. \end{aligned} \quad (3.13)$$

where u is a unit vector, $t \in \mathbb{R}$. It depends on the direction of derivation.

We recall that a *regular* closed set is such that it is equal to the closure of its interior. With V_{d-k}^L we denote the Lebesgue measure restricted to the $(d-k)$ -dimensional space L^\perp . Corollary 1 in Spiess and Spodarev (2010) asserts:

Theorem 3.2.6

Let Ξ be the union set of a stationary Poisson process of cylinders with intensity λ , shape distribution θ and regular cross section $K(Z) \in \mathcal{R}$ for θ -almost all $Z \in \mathcal{Z}_k$, direction $L(Z)$ and finite surface area density S_V . Then

$$\begin{aligned} S_V &= -\lambda \frac{d\kappa_d}{\kappa_{d-1}} \int_{\mathcal{Z}_k^0} \int_{G(1,d)} \gamma'_{K(Z)}(0, \pi_{L(Z)}(r_\xi)) [\xi, L(Z)] d\xi \theta(dZ) \cdot \\ &\quad \cdot \exp \left\{ -\lambda \int_{\mathcal{Z}_k^0} V_{d-k}^{L(Z)}(K(Z)) \theta(dZ) \right\}, \end{aligned}$$

where r_ξ is the unit direction vector of $\xi \in G(1, d)$, $\pi_{L(Z)}(r_\xi)$ is its orthogonal projection onto $L(Z)^\perp$, and $[\xi, L(Z)]$ is the volume of the parallelepiped spanned by the direction vectors of $L(Z)$ and ξ . The integration on $G(1, d)$ is with respect to the Haar probability measure.

Then for $d = 3$ and $k = 1$, it holds:

$$\begin{aligned} S_V &= -4\lambda \int_{\mathcal{Z}^0} \int_{G(1,3)} \gamma'_{K(Z)}(0, \pi_{L(Z)}(r_\xi)) [\xi, L(Z)] d\xi \theta(dZ) \cdot \\ &\quad \cdot \exp\{-\lambda \int_{\mathcal{Z}^0} V_2^{L(Z)}(K(Z)) \theta(dZ)\}. \end{aligned} \quad (3.14)$$

Moreover, it holds that

$$\int_{\mathcal{Z}^0} V_2^{L(Z)}(K(Z)) \theta(dZ) = \bar{A}$$

where \bar{A} is the mean area of $K(Z)$, i. e., is the expected value of the two-dimensional measure of the cross section of the cylinders.

The case of circular cross section with constant radius r is presented as an example in Spiess and Spodarev (2010). Formula (3.14) simplifies in

$$S_V = 2\pi r \lambda e^{-\lambda \pi r^2}$$

which corresponds to Equation (3.10). Thus, assuming isotropic cross section, the first two Miles' formulae are valid also in case of anisotropic orientation distribution, as for Boolean models. Nevertheless, in this case the shape of the cylinders depends only on one parameter, thus two equations are sufficient to determine the mean radius and the intensity of the process. We will apply this for fitting a model to a sample of cellulose fibers in Section 3.4.

Convex polygonal cross section

We now calculate the density of the surface area for processes of cylinders with convex polygonal cross section K . As these shapes are not isotropic, we need to consider also their orientation distribution. The information about the shape and orientation distribution of K is contained in the shape distribution $\theta(Z)$ of the cylinders, see Equation (3.8). This can be further decomposed (Spiess and Spodarev, 2010). Let $j : \mathcal{R} \times G(1, 3) \rightarrow \mathcal{Z}^0$ such that $j(K, L) = K \oplus L$ for $K \in \mathcal{R}$ with center of the circumscribed sphere in the origin, and $L \in G(1, 3)$. Then there exists a probability measure α , called the directional distribution of Ξ , and a probability kernel $\beta : \mathcal{B}(\mathcal{R}) \times G(1, 3) \rightarrow [0, 1]$ such that $\beta(\cdot, L)$ is concentrated on subsets of L^\perp and it holds

$$\theta(j(K \times G)) = \int_G \beta(K, L) \alpha(dL). \quad (3.15)$$

Note that α corresponds to the orientation distribution of the cylinder axes. We assume that α is independent of β . Moreover, we assume that for each cylinder the orientation and the shape of the cross section are independent of the cylinder axis.

Thanks to Corollary 5.2 in Spodarev (2002), the volume of the parallelepiped $[\xi, L(Z)]$ in $G(1, 3)$ is equal to $1/2$. Moreover, the derivative of the set covariance

$$\gamma'_{K(Z)}(0, \pi_{L(Z)}(r_\xi))$$

is restricted to the plane $L(Z)^\perp$. It depends only on $K(Z)$ and on the projection of the direction vector r_ξ onto this plane. We can express r_ξ in spherical coordinates as $r_\xi = (\sin \theta \cos \phi, \sin \theta \sin \phi, \cos \theta)$. We assume that Z is a cylinder with axis on the z -axis. Then, the projection of r_ξ onto $L(Z)^\perp$ is $\pi_{L(Z)}(r_\xi) = (\sin \theta \cos \phi, \sin \theta \sin \phi, 0)$, that is a vector of module $\sin \theta$ rotated of an angle ϕ from the x -axis. The derivative of the set covariance in the origin depends only on the angle ϕ which is uniformly distributed in $[0, 2\pi)$. Therefore, we can simplify the notation by writing u_ϕ for $\pi_{L(Z)}(r_\xi)$. Furthermore, the following holds:

Lemma 3.2.7

Let $K \subset \mathbb{R}^2$ be a convex polygon, then

$$\int_0^{2\pi} \gamma'_K(0, u_\phi) d\phi = -2p(K), \quad (3.16)$$

where u_ϕ is a unit vector with coordinates $(\cos \phi, \sin \phi)$ and $p(K)$ is the perimeter of K .

Proof The derivative of the set covariance in direction u_ϕ is -1 times the length of the orthogonal projection of the polygon K onto the line spanned by u_ϕ , see Lemma 2.1 in Nagel (1993) or Matheron (1975). This is the width of the polygon in the direction u_ϕ . Using the notation $h(K, \phi)$ for the support function (see Equation (1.5)), we have

$$\gamma'_K(0, u_\phi) = -(h(K, \phi) + h(K, -\phi)).$$

Then,

$$\begin{aligned} \int_0^{2\pi} \gamma'_K(0, u_\phi) d\phi &= - \int_0^{2\pi} (h(K, \phi) + h(K, -\phi)) d\phi = \\ &= -2 \int_0^{2\pi} h(K, \phi) d\phi = -2\pi \bar{b}(K), \end{aligned}$$

where we employed the definition of the mean width \bar{b} of K (Equation (1.6)). The mean width of a convex polygon is $p(K)/\pi$ and thus the lemma is proved. \square

We recall that the integral over $G(1, 3)$ is with respect to the Haar probability measure, which is normalized on $G(1, 3)$. Thus, expressing the integral in spherical coordinates, we have to divide by the surface area of the semisphere. Substituting Lemma 3.2.7 in Equation

(3.14), it holds that

$$\begin{aligned}
S_V &= -4\lambda e^{-\lambda\bar{A}} \int_{\mathcal{Z}^0} \frac{1}{2\pi} \int_0^{2\pi} \int_0^{\frac{\pi}{2}} \frac{1}{2} \gamma'_{K(Z)}(0, u_\phi) d\theta d\phi \theta(dZ) \\
&= -\frac{1}{\pi} \lambda e^{-\lambda\bar{A}} \int_{\mathcal{Z}^0} \frac{\pi}{2} (-2p(K(Z))) \theta(dZ) = \\
&= \lambda e^{-\lambda\bar{A}} \int_{\mathcal{Z}^0} p(K(Z)) \theta(dZ),
\end{aligned} \tag{3.17}$$

where

$$\int_{\mathcal{Z}^0} p(K(Z)) \theta(dZ) = \bar{p}$$

is the mean perimeter of the cross section. Then the surface area density of a Poisson process of cylinders with a convex polygon as the cross section, is

$$S_V = \lambda \bar{p} e^{-\lambda\bar{A}} \tag{3.18}$$

This holds for arbitrary orientation distribution of the cylinder axis and of the cross section.

We now verify Lemma 3.2.7 for squares and equilateral triangles where the set covariance can be calculated explicitly.

Let us assume that K is a square with fixed edge length a . We can assume $K = [0, a]^2$. In polar coordinates, we have $v = (\rho \cos \phi, \rho \sin \phi)$, with $\rho > 0$ and $\phi \in [0, 2\pi)$. Then, ϕ is the angle between the vector of translation v and one of the edges of the square, Figure 3.3(a). We suppose that the intersection of K and $(K - v)$ is non-empty, i. e., $\rho < a\sqrt{2}$. Furthermore, we can consider $\alpha \in [0, \pi/2]$, as the other cases are symmetric. The area is

$$\begin{aligned}
\gamma_K(v) &= (a - \rho \cos \phi)(a - \rho \sin \phi) \\
&= a^2 - a\rho(\cos \phi + \sin \phi) + \rho^2 \cos \phi \sin \phi.
\end{aligned}$$

Thus,

$$\gamma'_K(0, v) = -a(\cos \phi + \sin \phi),$$

which in absolute value is the length of the projection of K onto the direction spanned by v . Then the integral over $\phi \in [0, 2\pi)$ is

$$\begin{aligned}
\int_0^{2\pi} \gamma'_K(0, v_\phi) d\phi &= \int_0^{2\pi} (-a(\cos \phi + \sin \phi)) d\phi = \\
&= -4a \int_0^{\frac{\pi}{2}} (\cos \phi + \sin \phi) d\phi = \\
&= -4a(\sin \frac{\pi}{2} - \sin 0 - \cos \frac{\pi}{2} + \cos 0) = -8a,
\end{aligned}$$

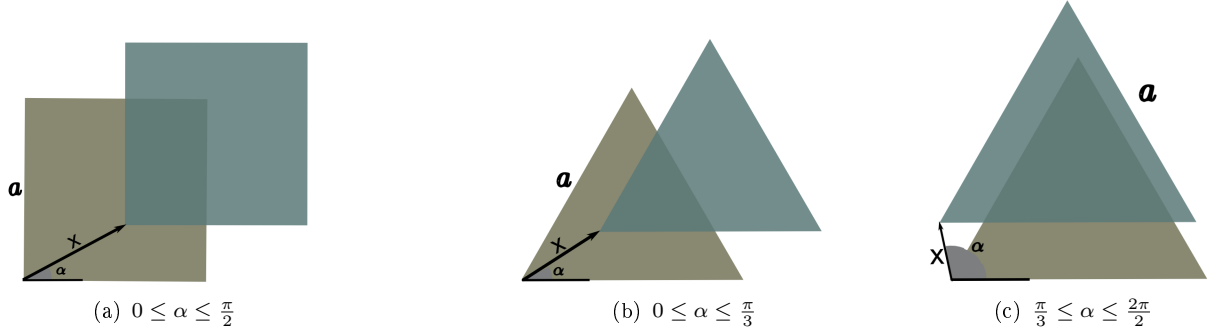


Figure 3.3: Square and triangle translated of a vector x . $\gamma_K(x)$ is the area of the intersection.

that is twice the perimeter of the square as claimed in Lemma 3.2.7.

Let us now proceed analogously for triangular cross sections. Let us assume that K is an equilateral triangle with edge length a and vertices $(0, 0)$, $(0, a)$ and $(a/2, \frac{\sqrt{3}}{2}a)$. Let us consider again $v = (\rho \cos \phi, \rho \sin \phi)$, with ρ small enough to guarantee a non-empty intersection. Due to symmetry, it is enough to calculate the set covariance in $\phi \in [0, 2\pi/3]$. Furthermore, the intersection $(K \cap K - v)$ is an equilateral triangle. For $\phi \in [0, \pi/3]$, the edge length is $a - \rho \cos \phi - \rho \sin \phi / \sqrt{3}$ (Figure 3.3(b)) and the area is

$$\begin{aligned} \gamma_K(v) &= \frac{\sqrt{3}}{4} \left(a - \rho \cos \phi - \frac{\rho \sin \phi}{\sqrt{3}} \right)^2 = \\ &= \frac{\sqrt{3}}{4} \left(a^2 - 2a\rho \left(\cos \phi + \frac{\sin \phi}{\sqrt{3}} \right) + \rho^2 \left(\cos \phi + \frac{\sin \phi}{\sqrt{3}} \right)^2 \right). \end{aligned}$$

For $\phi \in [\pi/3, 2\pi/3]$, the edge length of the intersection is $a - 2\rho \sin \phi / \sqrt{3}$ (Figure 3.3(c)) and the area is

$$\begin{aligned} \gamma_K(v) &= \frac{\sqrt{3}}{4} \left(a - \frac{2\rho \sin \phi}{\sqrt{3}} \right)^2 = \\ &= \frac{\sqrt{3}}{4} \left(a^2 - \frac{4}{\sqrt{3}}a\rho \sin \phi + \frac{4}{3}\rho^2 \sin^2 \phi \right). \end{aligned}$$

The directional derivative in the origin is

$$\gamma'_K(0, v) = \begin{cases} -\frac{1}{2}a(\sqrt{3}\cos \phi + \sin \phi) & \phi \in [0, \pi/3] \\ -a \sin \phi & \phi \in [\pi/3, 2\pi/3] \end{cases} \quad (3.19)$$

Due to symmetry, the integral over $[0, 2\pi]$ is three times the integral over $[0, 2\pi/3]$, which we can further split according to the value of γ' :

$$\begin{aligned} \int_0^{2\pi} \gamma'_K(0, v_\phi) d\phi &= 3 \left(\int_0^{\pi/3} -\frac{1}{2}a(\sqrt{3}\cos \phi + \sin \phi) d\phi + \int_{\pi/3}^{2\pi/3} -a \sin \phi d\phi \right) = \\ &= -3a \left(\frac{1}{2} \left(\sqrt{3} \sin \left(\frac{\pi}{3} \right) - \cos \left(\frac{\pi}{3} \right) + \cos(0) \right) - \cos \left(\frac{2\pi}{3} \right) + \cos \left(\frac{\pi}{3} \right) \right) = \\ &= -6a. \end{aligned}$$

This corresponds to Lemma 3.2.7.

3.3 Models with interaction

Although models with overlapping fibers are often capable to embed the significative features of the materials and can be used for simulations of physical properties, rigid fibers, such as steel or glass fibers, do not overlap. Thus, it is natural to look for models encompassing this feature. Avoiding intersections precludes the possibility of purely analytical definitions of the models. Instead, the models in this section are defined algorithmically. We will introduce the main features of three models and give references for further details. The first model we treat is the random sequential adsorption (RSA). It can be seen as the easiest way to insert cylinders in a compact window without overlapping. The definition yields a straightforward implementation. Then, we will deal with a different model for the fibers that comprises curvature. The fibers are represented by chains of overlapping balls, such that each ball is free to move within a certain constraint towards the neighboring balls (Altendorf, 2011). This model for fibers is applied to generate high density systems of fibers in a force-biased approach (fiber packing, Section 3.3.2) and in a sedimentation model (Section 3.3.3).

Systems in which intersections between objects are completely forbidden are called *hard-core*. However, interaction among fibers does not necessarily mean non-overlapping objects. Indeed, if only a small overlapping is allowed, the objects are not independent of each other as they are in Boolean models or in Poisson cylinder processes. If a certain overlapping is allowed, we talk about *soft-core* systems. The idea of Rikvold and Stell (1985) is that the object has a hard impenetrable core, like the pit of a cherry, whereas its shell is “soft”, i. e., penetrable. For example, one can construct a system of spheres, which can overlap up to some percentage of their radii. Alternatively, the soft-core ratio can be defined depending on the volume of the region of intersection. Both these criteria can be easily adapted to cylinders. Note that a soft-core ratio going to zero (a core of zero volume) yields total overlapping. Let us suppose to modify the RSA model so that the objects have a soft-core. The limit of an RSA model for the soft-core ratio going to zero is a Boolean model. Properties of soft-core systems of spheres have been analyzed in Rikvold and Stell (1985); Elsner et al. (2009). To our knowledge, analogous analyses for cylinders are still an open problem.

3.3.1 Random sequential adsorption (RSA)

The easiest way to obtain systems of non-overlapping arbitrary objects is by the algorithm known as *random sequential adsorption* (Feder, 1980; Hinrichsen et al., 1986). As for the Boolean model, the objects can be arbitrary compact convex bodies. In biology, RSA models of spheres are used, for instance, to model protein adsorption (Feder, 1980). Redenbach and Vecchio (2011) applied the model to a fiber system: an RSA model of cylinders is fitted to a glass fiber reinforced polymer and to a steel fiber reinforced high performance concrete. A realization can be seen in Figure 3.4(a).

Definition 3.3.1 (RSA)

Let X_1, X_2, \dots be a sequence of random convex compact sets with the center of the circumscribed sphere in the origin, independent and identically distributed as X_0 . Let $W \subset \mathbb{R}^3$ be a convex compact set (observation window). Then a realization of the random sequential adsorption model is the system $\{Y_i\}_{i=1}^N$ obtained by the following procedure:

do

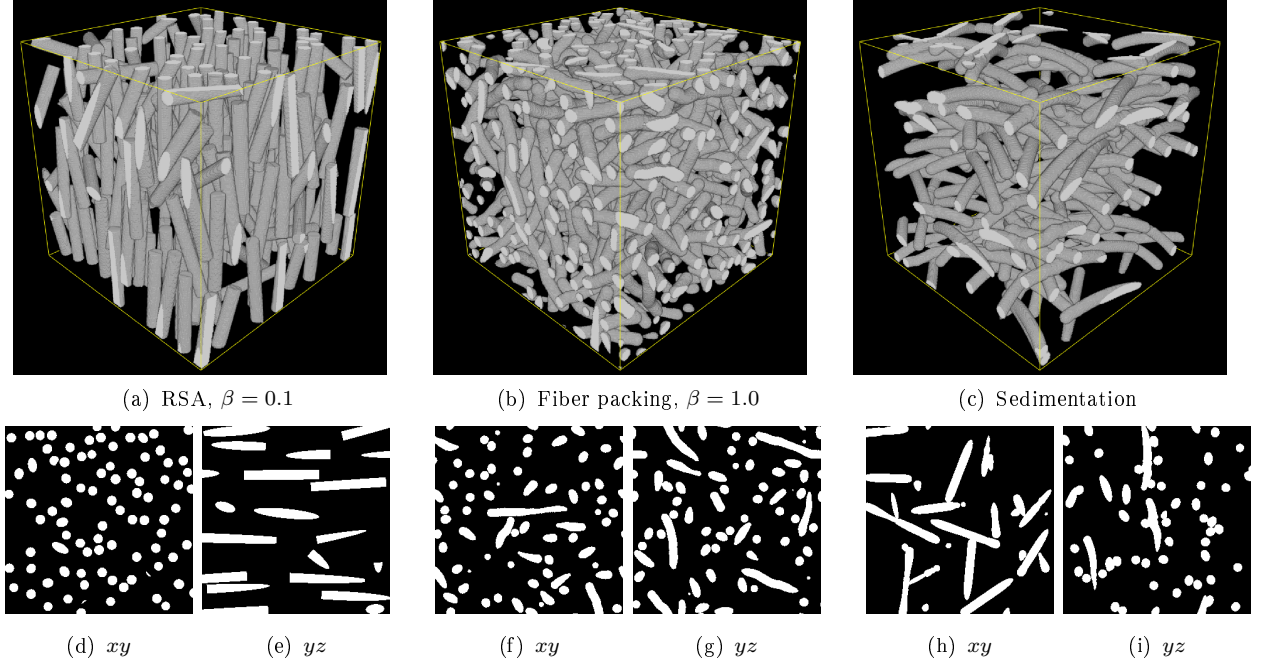


Figure 3.4: Realizations of models with interaction, volume renderings on top and cross sections. Radius 15 pixels, height 120 pixels. From left to right: RSA with $\beta = 0.1$, isotropic fiber packing, and sedimentation. Image size $300 \times 300 \times 300$ pixels.

1. draw X_{m+1} ,
2. draw a point x uniformly distributed in W ,
3. does $Y_{m+1} = X_{m+1} + x$ overlap with any of the already inserted bodies $\{Y_i\}_{i=1}^m$?
 - No: insert Y_{m+1} in $\{Y_i\}_{i=1}^m$, $m \mapsto m + 1$, and go to step 1.
 - Yes: go to step 2.

until

- (a) m equal to N (desired number of bodies), or
- (b) desired volume fraction V_V is reached, or
- (c) maximum number of trials is reached.

Note that in order to guarantee a uniform filling of W a suitable edge treatment must be used in simulations. For the collision test, it is necessary to keep track also of objects lying outside the observation window. The idea is to employ a plus-sampling of the observation window: the process is simulated in $W \oplus K$ with a suitable compact and convex K , and then cut into W . The estimation of V_V during the generation of the process should account only for the parts of cylinders inside W . Employing periodic boundary conditions yields that all the objects completely lie in W . Therefore, all the inserted objects completely contribute to the volume fraction reached at each step of the insertion process, thus the second stopping

criterion can be simply expressed as $\sum_{i=1}^m V(Y_i) \geq V_V V(W)$. For simplicity, from now on we will always work with periodic boundary conditions.

If X_0 is a random cylinder, then radius, length and orientation are drawn in the first step according to given distributions. These distributions are preserved by not repeating the first step in case a collision is detected. In fact, repeating step 1 would introduce a deviation from the desired distribution. For instance, small objects or objects with certain orientations are more likely to find a fitting position. A very large number of positions needs to be tested to show that it is not possible to insert a new cylinder in a given configuration. In this case, it is said that the *jamming limit* is reached. The jamming limit strongly depends on the distributions of the shape parameters and of the orientation. Also for the simpler case of spheres, the jamming limit cannot be computed analytically for arbitrary distributions of the radii, but has been studied by Monte-Carlo simulations (Feder, 1980; Meakin and Jullien, 1992). According to Altendorf (2011), systems of cylinders with aspect ratio 1:10 and isotropic orientation distribution have jamming limit between 10% and 15%.

Analogously to Boolean models, the parameters of the RSA model are those determining the distribution of the radius and of the length of the typical cylinder, its orientation distribution and the intensity of the process λ , i. e., the expected number of objects in a unit volume. Thanks to the absence of intersections among the objects and the additivity property of the intrinsic volumes, we have

$$V_{V,k} = \frac{1}{V(W)} \sum_{i=1}^N V_k(Y_i)$$

for $k = 0, \dots, 3$ and N the number of objects inserted in W . In particular, the density of the Euler number is the expected number of objects in a unit window $\chi_V = \mathbb{E}[N_W]/V(W)$ that is equal to λ . Moreover, it holds (Ohser and Mücklich, 2000)

$$\begin{aligned} V_V &= \lambda \bar{V}, \\ S_V &= \lambda \bar{S}, \\ M_V &= 2\pi \lambda \bar{b}, \\ \chi_V &= \lambda, \end{aligned}$$

where $\bar{V} = \mathbb{E}[V_3(X_0)]$, $\bar{S} = 2\mathbb{E}[V_2(X_0)]$ and $\bar{b} = \frac{1}{2}\mathbb{E}[V_1(X_0)]$ are the mean values of the intrinsic volumes of X_0 . Note that the advantage of these formulae with respect to the Miles formulae is that these are independent of the orientation distribution and of the shape of the cylinders.

3.3.2 Fiber packing

We introduce a model of fiber packing developed by Altendorf (2011) and published also in Altendorf and Jeulin (2011b,c). It was originally thought for glass or carbon fiber reinforced composites and ultra high performance concrete. This model includes the possibility to achieve high volume densities and bend fibers, still ensuring the realization of the desired orientation distribution. A realization of the model can be seen in Figure 3.4(b).

First of all, we present the model for the fibers. Each fiber is a chain of overlapping balls. The ball chain is generated by a random walk of points $p_i = (x_i, \mu_i, r_i)$, where x_i is the

position of the center, μ_i is the (local) orientation and r_i is the radius. For each fiber, a main orientation μ_0 is drawn according to a β -distribution fitted to the orientation distribution of the observed fiber system. To generate a new point p_{i+1} in the random walk, a new orientation is drawn according to a multivariate von Mises-Fisher distribution with μ_0 and μ_i as parameters, see Section 3.1. Then the radius r_{i+1} is chosen, and thus $x_{i+1} = \frac{r_{i+1}}{2}\mu_{i+1}$. The concentration parameter κ_1 corresponds to the principal orientation and determines the reliability to the main fiber orientation. Instead, the concentration parameter κ_2 corresponds to the local orientation and controls the bending of the fiber. Once a ball chain $\{p_0, \dots, p_l\}$ is generated, the fiber is completely defined and its mean orientation is given by $\bar{\mu} = \frac{x_l - x_0}{\|x_l - x_0\|}$. In general, $\bar{\mu}$ differs from μ_0 . Therefore, in order to respect the global orientation distribution, the fiber is rotated so that $\bar{\mu}$ equals to μ_0 . The rotation being a rigid motion, radius, length and mutual positions of the balls are not affected. The radius and length follow given random distributions. Moreover, the radius can vary within a fiber. Note that the number of balls in each fiber is a compromise between the smoothness of the fiber and reasonable computational time.

Realizations of the fiber packing are obtained through the following steps. At first, each fiber is generated independently from the others and inserted in the observation window in a uniformly distributed position. Of course, this generates a system of overlapping fibers. Now, the second innovative idea of this model comes into play. A hard-core system is obtained by applying two types of forces to the ball centers: a repulsion force to avoid overlapping and a recover force to preserve the fiber structure. This method is adapted from the force-biased approach for sphere packings described by (Mościński et al., 1989). Details on the definitions of the forces and on the convergence of the rearrangement step are found in Altendorf (2011). The fact that collisions are tested and adjusted locally allows a speed up in the computation time of the algorithm.

Compared to the models previously described, the fiber packing has a larger set of parameters. Again, we have the volume fraction, radius, length, and orientation distribution of the fibers. In addition, we need the curvature, expressed by the concentration parameters κ_1 and κ_2 . The number of balls in each fiber and parameters for the forces are considered technical parameters and do not need to be estimated for each sample. As the model itself cannot be described in a compact form, it is not possible to find analytical formulations linking characteristics of the system and of the fiber. The fibers are not overlapping, thus the volume fraction is the sum of the volumes of the inserted fibers divided by the volume of the window (assuming periodic edge treatment). The same holds for the other intrinsic volume densities. However, even to compute the total fiber volume is not trivial as it depends on the overlapping of the balls in the chains. Altendorf (2011) treats the problem of estimating geometric characteristics directly from CT data thoroughly. To estimate the curvature, it is necessary to separate the fibers. Starting from binary images, the idea is to define the probability for each foreground point to belong to a fiber. Then the fibers are reconstructed as chains of balls. From this representation, the parameters of the multivariate von Mises-Fisher distribution can be estimated. This method was validated on synthetic data and applied to a fiber reinforced composite with a fiber volume fraction around 15%. However, the reliability is expected to decrease rapidly for higher volume densities.

3.3.3 Sedimentation

Sedimentation or deposition models exploit a physically motivated approach to generate high density systems of non-overlapping objects. The idea is to imitate the process of particles sedimenting in a medium in order to minimize a potential energy. Models for the sedimentation of spheres date back to Vold (1960). Coelho et al. (1997) investigate the sedimentation of ellipsoidal and polyhedral grains. A model for sedimented fibers is presented in Provatas et al. (2000). Naturally, sedimentation models are best applied when the fiber systems present a girdle orientation distribution. For instance, the production of paper sheets can be interpreted as a sedimentation. The model developed in Lavrykov et al. (2012) embeds the mechanical properties of the pulp fibers to define their shape and simulate the deposition and pressing in order to achieve a realistic fiber configuration. Our focus is however different. We aim at modeling the geometry of the sedimented fibers, independently from the production process. Therefore, the physics of the system is significantly simplified. We propose a model which features the classical principles of sedimentation present also in Coelho et al. (1997) and Provatas et al. (2000), enriched with the definition of fibers as ball chains as in the fiber packing model. A realization can be seen in Figure 3.4(c).

The common features in Coelho et al. (1997) and Provatas et al. (2000) that we will also apply in our sedimentation model are the following:

- The observation window W is oriented so that it makes sense to talk about “top” and “bottom”. For simplicity, the bottom corresponds to the plane $z = 0$. Increasing the value of z yields a higher potential energy. This can be interpreted as the presence of a gravitation field in the z direction.
- Overlapping is not allowed.
- The objects are inserted one by one from the top of the window. They fall until either the object reaches the bottom or collisions with other objects are detected.
- Once the object is sedimented, it is not possible to modify its shape or its position.

The models differ with respect to the packing strategy. In Coelho et al. (1997), in order to minimize the height where the collision occurs, the grains are translated and rotated while falling. This modifies the initial position and orientation of the object, but not its shape. The fibrous objects treated in Provatas et al. (2000), instead, are not rigid: when collision occurs, the shape of the fiber is locally modified to fill up the empty space at lower heights. In this approach, the position of the fiber and the orientation in the xy plane are not modified during the process.

The gravitation field yields a non-stationarity in the z direction. Our aim is to keep stationarity in the xy plane, so that if the model is observed in a planar section (perpendicular to the z axis), it is stationary. The initial position of the object is a point with uniformly distributed (x, y) coordinates and z fixed to the top of the window. To not affect the planar stationarity, translations in the xy -plane are not allowed. Moreover, we aim at preserving the desired orientation distribution. Nevertheless, in this model we can only control the planar distribution. Although the initial planar orientation will not be affected during the process, the final mean orientation will also depend on the bending. The fiber is initially a rigid cylinder with radius and length drawn from arbitrary distributions. The cylinder falls

in the observation window. After a collision is detected, the fiber is interpreted as a chain of overlapping balls. Suppose the i -th ball touches a sedimented fiber, while a ball next to it does not. Now, different strategies can be applied to further move down the neighboring ball. We use a flexibility factor k to control the maximal distance on the z -axis between neighboring balls. While in Provatas et al. (2000) the distance of the centers is compared with a constant factor, we use:

$$|z_i - z_j| \leq kr \quad (3.20)$$

where (x_i, y_i, z_i) and (x_j, y_j, z_j) are the coordinates of neighboring balls in a fiber of radius r . By construction, we fix $(x_i - x_j)^2 + (y_i - y_j)^2 = r^2/2$. A factor $k = 0$ yields rigid fibers, while large k allows more flexibility in the fibers. In this case, higher volume fractions can be obtained, but at the price of more curvature with the possibility of sharp bending.

The model can be refined by initializing the cylindrical fibers with arbitrary (spatial) orientation. In this case, the distance between the centers of neighboring balls depends on the z coordinate also in the plane, thus the criterion in (3.20) must be adapted:

$$(x_i - x_j)^2 + (y_i - y_j)^2 + (z_i - z_j)^2 \leq kr^2 \quad (3.21)$$

With small k , the initial orientation of the fiber significantly influences the shape of the sedimented fiber.

It is possible to base the flexibility criterion on more sophisticated rules. For example, instead of using the distance, one could check the angles formed by three neighboring balls. It is also possible to introduce a global criterion by defining a maximum bending for each fiber. Different structures can be obtained by allowing balls to increase their z coordinate after collision. One could approximate the fiber with a spline, locally or globally, so that the fiber is smoothly curved. Qualitatively, this seems a good approximation for glass fibers. However, this strategy has not been investigated so far.

The definition of the model does not allow an analytical description of its geometric characteristics. The initial orientation distribution can be fitted to the sample as before, however, the structure obtained by sedimentation will have a higher concentration around the equator. The techniques proposed in Altendorf (2011) to estimate the curvature of the fibers can be exploited also for this model.

3.4 Application to cellulose fiber systems

In this section, we analyze a sample of medium density fiber board. During the production of this material, the cellulose fibers are pressed together to obtain a high density composite. MDF boards are widely used for furniture elements and as thermal or acoustic insulators in constructions. The sample is imaged with micro-computed tomography with spacing 1 pixel = 7.857 μm . Visualizations of the cross sections and a volume rendering of the binarized image can be seen in Figure 3.5. The fibers are strongly anisotropic, mainly lying in the xy plane. At this image resolution, the fibers often overlap and are only a few pixels thick. The densities of the intrinsic volumes and the structure model index estimated from the binary image are summarized in Table 3.1.

Although it is not very evident in the image of this sample, wood fibers have typically rectangular cross sections. We will investigate whether significant differences occur in mod-

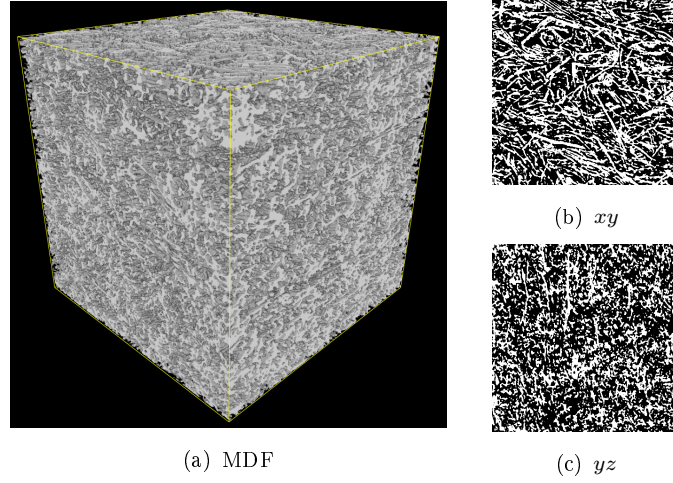


Figure 3.5: Visualizations of the MDF sample. Pixel size $7.857\mu\text{m}$, image size 400^3 pixels = 3.14^3 mm^3 . CT scan by Frank Sieker (GE Measurement & Control phoenix|x-ray, Wunstorf). Binarization by Oliver Wirjadi (Fraunhofer ITWM).

els with cylinders with squared and circular cross sections. Boolean models and Poisson processes of cylinders are fitted to the samples and compared.

3.4.1 Model fitting and validation

The parameters of the model are the intensity and the mean thickness of the fibers, i. e., the diameter for circular cross section and edge length for squared cross section, respectively. Furthermore, in case of squares, we need to assign an orientation distribution of the cross section. Due to the low resolution, we cannot measure the distribution of thickness and length from the image, nor the orientation distribution of the cross section assuming it is squared. Thus, we model the fibers with cylinders of constant thickness and length, and isotropic orientation of the cross section.

We start fitting Poisson processes of cylinders with circular and squared cross sections. Then, the thickness and the intensity of the model can be calculated solving the system of the two Miles formulae valid for anisotropic processes (Equations (3.9)-(3.10) for circles, and Equations (3.9)-(3.18) for squares). They suffice to estimate the mean thickness of the cylinders and the intensity of the model, in both cases of circular and squared cross section. We obtain:

- circular cross section: $\lambda = 0.0358$, radius = 2.08 pixels = $16.32 \mu\text{m}$;
- squared cross section: $\lambda = 0.0281$, edge length = 4.15 pixels = $32.63 \mu\text{m}$.

The estimated thickness of the fibers is about the same in both cases. Realizations in a window of 400^3 pixels = 3.14^3 mm^3 (as the observed sample) contain more than 10 000 cylinders for each model.

We now suppose that the sample is a realization of a Boolean model of cylinders. We need to estimate also the length of the cylinders, thus the two Miles formulae for volume fraction and surface area density Equations (3.4)-(3.5) do not suffice to estimate all the parameters

	V_V	S_V	M_V	χ_V	SMI
MDF	0.384031	0.287468	0.021183	-0.002575	1.18126
Boolean circle	0.387229	0.264318	0.015543	-0.002171	1.03375
Boolean square	0.383708	0.251056	0.010354	-0.001717	0.75637
Poisson circle	0.386536	0.260696	0.014413	-0.002103	0.98370
Poisson square	0.384804	0.246903	0.008902	-0.001666	0.67433

Table 3.1: Characteristics of the MDF sample compared to those of the models estimated on some realizations.

of the model. However, we can suppose that the thickness of the cylinders, whether radius or edge length, estimated in the case of the Poisson cylinder process is a good estimate for the mean thickness of the fibers. Therefore, we can use this information in the Miles' formulae. We obtain in both cases lengths around 150 pixels.

We still need to estimate the orientation distribution of the cylinder axes. The β -distribution is the obvious choice for girdle orientation (Section 3.1). We look at the distribution of the diameters in the 13 discrete directions which is a coarse estimation of the orientation distribution of the fibers. This distribution is uniform around the z -axis and concentrated mainly on the xy plane. To find the value of β we actually proceed via simulations. We generate realizations of the Poisson cylinder processes and Boolean models and compared not only the diameters, but also other geometric characteristics of the union of fibers, as they are all influenced by the orientation. We found that a good fit is obtained with $\beta = 5.0$.

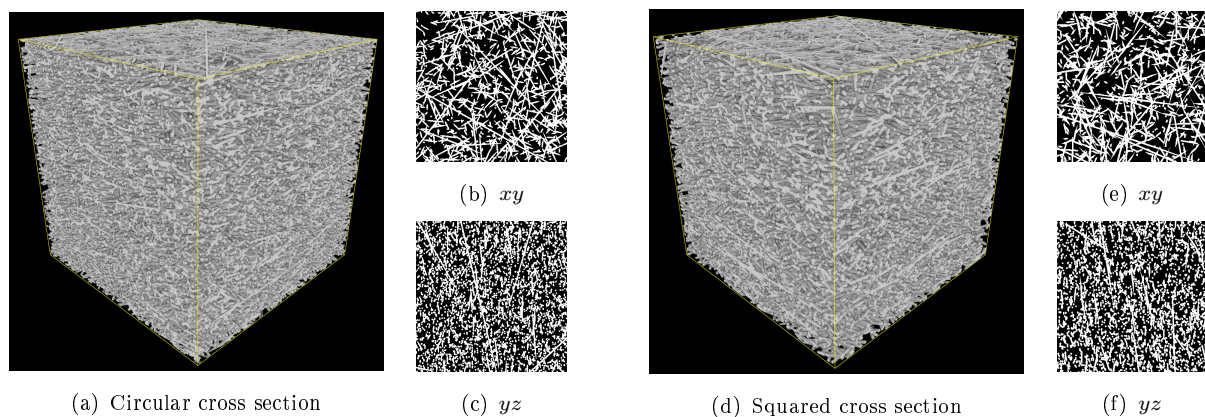


Figure 3.6: Realizations of Poisson cylinder processes fitted to the MDF sample with cylinders with circular cross section (left) and squared cross section (right).

Some realizations are shown in Figures 3.6 and 3.7. As the cylinders are only about 4 pixels thick, it is hard to recognize the shape of the cross sections. In fact, the discretization of a circle of radius 2 pixels ends up being almost indistinguishable from a square of edge length 4 pixels. The intrinsic volume densities estimated on some realizations of the models are shown in Table 3.1. Only V_V and S_V were employed in the model fitting, therefore comparing the other values gives a validation of the model. The density of the integral of

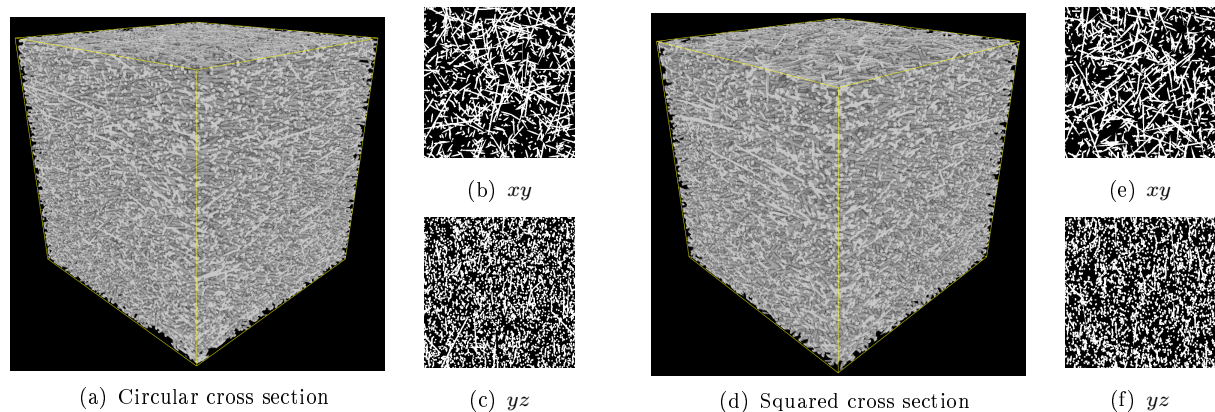


Figure 3.7: Realizations of Boolean models of cylinders fitted to the MDF sample with cylinders with circular cross section (left) and squared cross section (right).

mean curvature M_V of the models is lower than the value estimated from the sample. This can be easily explained by the choice of straight cylinders. In fact, the cellulose fibers are sometimes curved. Moreover, M_V is particularly low for models of cylinders with squared cross sections. This is due to the fact that the surface of the squared cylinders is flat, whereas a cylinder with circular cross section has positive curvature along all directions not parallel to the axis. Of course, the density of the integral of mean curvature causes also the discordance in the values of the structure model index. Also the density of the Euler number is better matched by models with circular cross sections. From these values, the best fitting model is the Boolean model of cylinders with circular cross section.

Further validation of the models is obtained with the spherical granulometry transform. Suppose that the foreground is the component of interest in a given binary image. Then, spherical granulometry assigns to each foreground pixel, the radius of the largest sphere contained in the foreground and covering the pixel. In this way, a map of the local thickness of the structure is obtained. In our case, we can apply it both to the pore space and to the fiber system. The results are shown in Figures 3.8 and 3.9 as empirical cumulative distributions. The trends of the models are similar. For all models, the pore space is locally larger than in the sample, whereas the fibers are locally thinner. There are almost no differences in the granulometry of the Poisson processes and of the Boolean model inside the fibers. This is not surprising as the thickness of the cylinders is the same for each cross section and the length does not affect this measurement. Conversely, the cylinder length affects the granulometry in the pore space. The difference in the local pore size is small, but enough to suggest that Boolean models better fit to the sample. Concerning the shape of the cross section, circles yield a better fit in the local pore size thickness, whereas the granulometry map inside the fibers is fitted better by squared cross sections. This supports the fact that the shape of the fibers is better modeled by cylinders with squared cross section.

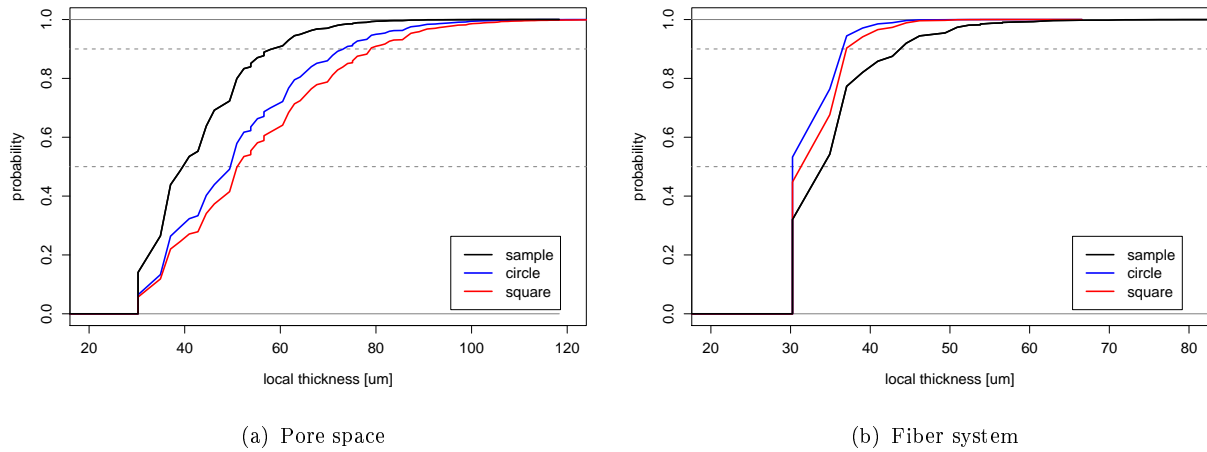


Figure 3.8: Comparison of the spherical granulometry on the pore space (left) and on the fibers (right) estimated from the sample and from realizations of the Poisson process of cylinders with circular and squared cross section.

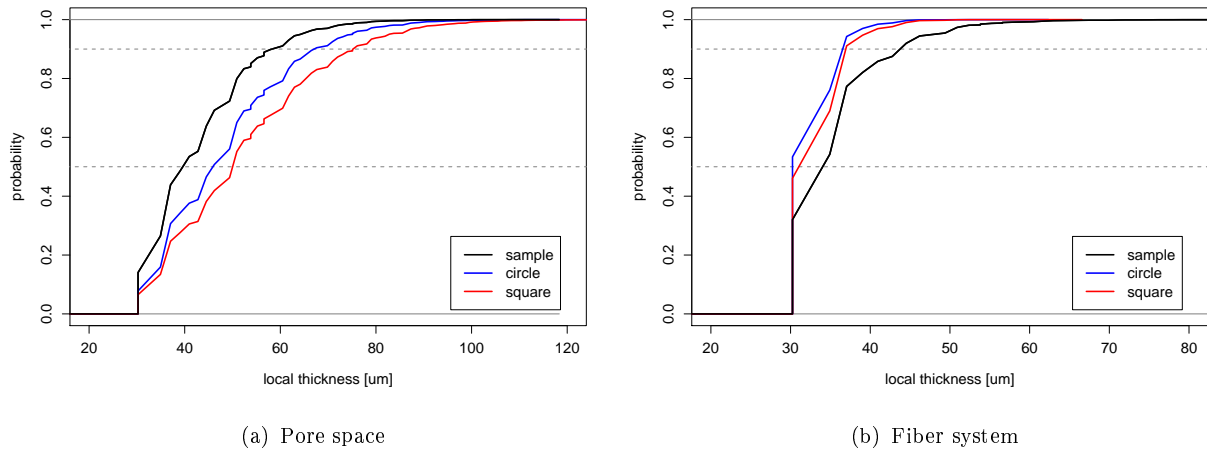


Figure 3.9: Comparison of the spherical granulometry on the pore space (left) and on the fibers (right) estimated from the sample and from realizations of the Boolean model of cylinders with circular and squared cross section.

3.5 Discussion

To characterize fiber systems based on image data, it is rarely possible to estimate geometric characteristics of each fiber. Due to the numerous overlappings appearing in low resolution images, even estimates based on local information are unreliable. In these cases, it is not possible to infer enough information from the samples to fit complex models. However, we showed that the intrinsic volume densities, theoretically, suffice to deduce the parameters of Poisson processes and Boolean models of cylinders with circular cross sections. Moreover, we derived formulae valid also for polygonal cross sections for anisotropic Poisson cylinder processes. Nevertheless, in this case also the orientation distribution of the cross section needs to be estimated. As it is often not possible to estimate it directly from the image data, one can proceed with repeated simulations of the model. Then, the best fitting distribution can be chosen comparing geometric characteristics of the system of fibers and of the realizations, like the intrinsic volume densities and the structure model index. Moreover, one can compare the granulometry map as we did to validate the models fitted to the MDF sample. We showed on this sample how to fit Boolean models and Poisson processes of cylinders with circular and squared cross sections. The same procedure of model fitting can be applied to other samples. If the fibers are more than a few pixel thick, the differences in the characteristics of models with polygonal cross sections and with circular cross sections are more evident.

We gave a short introduction on three models with interaction among the fibers. The parameters of the RSA model can also be estimated from the knowledge of the intrinsic volume densities of the fiber system only. Moreover, this model is well defined for arbitrary objects, e. g., cylinders with arbitrary cross sections, or non-convex fibers. However, an efficient implementation for an arbitrary object is not possible. In fact, testing overlapping in the discretized realization of the model is time consuming, as it would require multiple scanning of a 3d image. Analytical tests for collisions of objects with arbitrary orientation and shape are not trivial.

Modeling the fibers as ball chains, modifying the cross section to convex polygons implies major changes in the definition of the model itself. Many steps of the generation of a realization would be affected, too. Not only the contact between fibers needs to be detected differently, but the strategies to deal with it also have to be adapted. For instance, a cuboid could be rotated around its axis to avoid overlapping, while this is no use for circular cylinders or spheres.

Chapter 4

Models for foams

A foam is a highly porous structure. The material has low volume density and is distributed around a large number of gas or air pores. If the pores, or cells, are interconnected, we talk about *open-cell foams* and the material is completely concentrated in the struts. *Closed-cell foams*, instead, are characterized by the presence of thin films of material between the pores. Both open and closed foams can be observed in nature at different scales, from bone tissue to sea-sponges through milk and soap froth. Manufactured foams have been developed for a wide variety of applications, including medicine, aerospace, and automobile industry. Mainly, manufactured foams are polymer, ceramic, or metal foams. Industrial polymer foams are particularly suitable as sandwich-core materials thanks to their low specific weight and stiffness.

Instead of directly modeling the material, we model the geometry of the pore space of the foam. Letting the volume of the material shrink to zero, the pores tend to be a collection of cells which only intersect on their boundaries and such that their union is the whole window. This is a heuristic definition of a tessellation, i. e. a partition of space.

Definition 4.0.1

A *tessellation* or *mosaic* T in \mathbb{R}^d is a set $T = \{C_i \subset \mathbb{R}^d, i \in \mathbb{N}\}$ such that for all $C_i, C_j \in T$

- (i) C_i is a full dimensional, bounded convex subset of \mathbb{R}^d ,
- (ii) $C_i, C_j \in T$ and $C_i \neq C_j$, then $\overset{\circ}{C}_i \cap \overset{\circ}{C}_j = \emptyset$,
- (iii) $\bigcup_{i \in \mathbb{N}} C_i = \mathbb{R}^d$,
- (iv) for every compact Borel set $W \subset \mathbb{R}^d$, $\#\{C \in T : C \cap W \neq \emptyset\} < \infty$, i. e. T is locally finite.

Matheron (1975) gives a more general definition of random tessellation which allows to consider non-convex cells. An example is the Johnson-Mehl tessellation (Møller, 1992). However, we restrict to convex cells as these are a good approximation when modeling solid foams, for both open and closed cell foams (Fan et al., 2004; Kanaun and Tkachenko, 2006; Redenbach et al., 2012b; Wejrzanowski et al., 2013).

First, we will introduce the concept of random tessellations and highlight how to describe the geometry of a tessellation. Then, we will focus on models based on point processes: Voronoi and Laguerre tessellations. After motivating the choice of the model, we will present

a well established method to fit a stochastic model to samples of foams starting from 3d μ CT images. Strategies to improve this method are discussed and verified on some samples of polymethacrylimide foams in Section 4.3. In the last part of this chapter (Section 4.4), we will deal with the well known problem of short edges occurring in Laguerre tessellations. We will apply a method to reduce the number of short edges usually employed in modeling soap froth (Kraynik et al., 2003). By investigating the geometric characteristics of some samples of closed and open cell foams, we will discuss when the Laguerre tessellation models need to be modified to better feature the edge length distribution of the foams.

Parts of the analysis and results presented in this chapter are also published in Vecchio et al. (2012a,c, 2014). The definitions and notations in this chapter are mainly taken from Lautensack (2007) and Schneider and Weil (2008).

4.1 Random tessellations

A consequence of Definition 4.0.1 is that the cells are convex polytopes, i. e., convex and compact intersections of a finite number of halfspaces generated by hyperplanes (Schneider and Weil, 2008, Lemma 10.1.1). Therefore, in 3d each cell can be characterized by its facets, edges and vertices. In general, we define a k -face of a tessellation T for $k \in \mathbb{N}_0$, $k < d$ as the k -dimensional intersection of adjacent cells. Let

$$F(x) = \bigcap_{C \in T, x \in C} C,$$

for $x \in \mathbb{R}^d$. Then $F(x)$ is a k -dimensional polytope. For $k = 0$, k -faces are the vertices of a tessellation, which are usually called nodes. Furthermore, the set of the k -faces of T is

$$\mathcal{F}_k(T) = \{F(x) : \dim F(x) = k, x \in \mathbb{R}^d\}. \quad (4.1)$$

Definition 4.1.1

A tessellation T in \mathbb{R}^d is called *face-to-face* if the k -faces of T coincide with the k -dimensional faces of the cells, that is,

$$\mathcal{F}_k(T) = \bigcup_{C \in T} \mathcal{F}_k(C),$$

for $k = 0, \dots, d-1$. A face-to-face tessellation is said to be *normal* if every k -face belongs to exactly $d - k + 1$ cells.

For $d = 3$, in normal tessellations nodes are shared by four cells, edges by three and facets by two.

Following Lautensack and Zuyev (2008), we define $\mathcal{P}_k \subset \mathbb{R}^d$ as the set of all k -dimensional polytopes and $c_k : \mathcal{P}_k \times \mathcal{T} \rightarrow \mathbb{R}^d$ the *centroid function*, that is

$$c_k(F + x, T + x) = c_k(F, T) + x$$

for $x \in \mathbb{R}^d$, $F \in \mathcal{P}_k$, $T \in \mathcal{T}$ and such that $c_k(F) \neq c_k(F')$ for $F, F' \in \mathcal{P}_k$, with $F \neq F'$. The point $c_k(F, T)$ is the *centroid* of the k -face F . One can take, for instance, the geometric center or baricenter of F . This choice will not affect the following results.

Random tessellations are defined as point processes with values in the space of tessellations equipped with a suitable σ -algebra. More precisely, let \mathcal{T} be the set of all face-to-face tessellations with convex cells in \mathbb{R}^d and \mathcal{S} the σ -algebra generated by the sets

$$\{T \in \mathcal{T} : \mathcal{F}_k(T) \cap K \neq \emptyset\}$$

for all compact sets $K \subset \mathbb{R}^d$ (Stoyan et al., 1995).

Definition 4.1.2

A random tessellation T is a measurable mapping from a probability space $(\Omega, \mathcal{A}, \mathbb{P})$ with values in \mathcal{T} furnished with the σ -algebra \mathcal{S} . The distribution of T is the induced probability measure \mathbb{P}_T .

We say that a random tessellation is normal if its realizations are almost surely normal. Again, stationarity and isotropy are defined as invariance of the distribution to translations and to rotations, respectively. They are defined with respect to the cells of the tessellation:

$$\begin{aligned} T + x &= \{C + x : C \in T\}, \quad x \in \mathbb{R}^d, \\ \theta T &= \{\theta C : C \in T\}, \quad \theta \in SO(\mathbb{R}^d). \end{aligned}$$

4.1.1 Geometric characterization

We now introduce other processes induced by a random tessellation T which can be exploited to geometrically characterize T .

A random tessellation T implicitly defines the point processes N_k of the centroids of k -faces for $k = 0, \dots, d$. From now on, we will assume to deal only with stationary tessellations. In this case, also the processes of the centroids are stationary. The intensities of the centroid processes are

$$\gamma_k = \mathbb{E} \left[\sum_{F \in \mathcal{F}_k(T)} \mathbf{1}_{[0,1]^d}(c_k(F, T)) \right] \quad (4.2)$$

for $k = 0, \dots, d$. These intensities can be interpreted as characteristics describing the tessellation. In fact, γ_k is the mean number of k -faces per unit volume. Furthermore, we consider the topological numbers of the k -faces. Let $n_{jk} : \mathcal{P}_j \rightarrow \mathbb{N}$ with $k, j = 0, \dots, d$ and such that $n_{jk}(P)$ is the number of k -dimensional faces in the j -dimensional polytope P . For normal tessellations it holds (Lautensack, 2007, Theorem 1.6.5)

$$\gamma_k = \gamma_d \frac{\mathbb{E}_{N_k}[n_{dk}(F_d(0))]}{d - k + 1} \quad (4.3)$$

and

$$(1 - (-1)^k) \gamma_k = \sum_{j=0}^{k-1} (-1)^j \binom{d-j+1}{k-j} \gamma_j. \quad (4.4)$$

Thus for $d = 3$ we get

$$2\gamma_0 = \gamma_1 = 2(\gamma_2 - \gamma_3). \quad (4.5)$$

Recalling the Palm distribution of point processes (Definition 1.2.7), we denote \mathbb{P}_k^0 the Palm distribution of N_k . With respect to \mathbb{P}_k^0 , almost surely there exists a k -face $F_k(0)$ with

centroid in the origin. A random k -dimensional polytope with the same distribution as $F_k(0)$ is the *typical k -face* of the random tessellation T . Heuristically, the typical k -face is a k -face chosen at random such that all the k -faces of the tessellation have the same probability of being taken. Characterizing the typical k -faces of the tessellation is a way to statistically characterize the whole tessellation.

Now, we consider the measures

$$M_k(B) = \sum_{F \in \mathcal{F}_k(T)} \mathcal{H}^k(F \cap B) \quad (4.6)$$

for $B \in \mathcal{B}(\mathbb{R}^d)$, $k = 0, \dots, d$. They are stationary random measures with intensity

$$\mu_k = \mathbb{E} \left[\sum_{F \in \mathcal{F}_k(T)} \mathcal{H}^k(F \cap [0, 1]^d) \right]. \quad (4.7)$$

The intensities μ_k represent the mean k -dimensional volume of the k -faces in a unit volume. In 3d, μ_1 is the total edge length per unit volume and is usually written L_V , whereas $\mu_2 = S_V$ is the surface area density. Note that $\mu_3 = 1$ due to the property of tessellations to be space filling.

There is a relation between the intensities γ_k and μ_k (Lautensack, 2007, Corollary 1.6.4):

$$\mu_k = \gamma_k \mathbb{E}_{N_k} [\mathcal{H}^k(F_k(0))].$$

The parameters γ_k and μ_k completely describe the geometry of a random tessellation. Moreover, thanks to the properties of normal tessellations, in \mathbb{R}^3 only four characteristics are not redundant. A classic choice for the four characteristics is the set of Mecke's parameters: $\gamma_0, \mu_1 = L_V, \mu_2 = S_V$, and γ_3 (Mecke, 1984). Equivalently, one can choose parameters which describe the typical cell C . The advantage is that characteristics of the cells are easier to estimate from images. Cells are compact bodies and thus we can exploit the characterization of Chapter 2.

We denote $N_{jk} = \mathbb{E}[n_{jk}(F_j)]$, that is, the mean number of k -faces in the j -dimensional typical face. Then, N_{32} is the mean number of facets per cell. The Euler formula for polytopes can be expressed as

$$N_{32} - N_{31} + N_{30} = 2.$$

Besides, normality yields

$$\begin{aligned} N_{03} &= 4, & N_{02} &= 6, & N_{01} &= 4, \\ N_{13} &= 3, & N_{12} &= 3, \\ N_{23} &= 2. \end{aligned} \quad (4.8)$$

$$(4.9)$$

From (4.3) and (4.5), it follows

$$N_{32} = 2 \frac{\gamma_2}{\gamma_3} = \frac{2(\gamma_0 + \gamma_3)}{\gamma_3}.$$

N_{32} is the topological number we use to characterize tessellations. It can also be interpreted as a measure of the regularity of the tessellation. Broadly speaking, a large mean number of

facets per cell is found in irregular tessellations. We will see some examples when discussing models and analyzing some samples of foams. In the following, we will alternatively use also the symbol F_C for N_{32} . To complete the set of four characteristics equivalent to Mecke's parameters we choose the mean intrinsic volumes of the typical cell: the mean mean width $\bar{b} = V_1(C)/2$, the mean surface area $\bar{S} = V_2(C)$, and the mean volume $\bar{V} = V_3(C)$. Their relations to Mecke's parameters are

$$\begin{aligned} L_V &= \frac{4\bar{b}}{\bar{V}}, \\ S_V &= \frac{\bar{S}}{2\bar{V}}, \\ \gamma_3 &= \frac{1}{\bar{V}}. \end{aligned}$$

To fit a random tessellation to a sample of foam we will start by fitting the distributions of the four characteristics F_C , \bar{b} , \bar{S} , and \bar{V} . Details are given in Section 4.3.

4.2 Tessellation models

A special foam is soap froth, which deserved the title of “quintessential foam” (Kraynik et al., 2004) for its properties. Plateau (1873) described the geometry of dry soap froth in the mechanical equilibrium limit, that is, when surface energy is minimized. Plateau's laws are the following (Weaire and Hutzler, 1999):

- (i) facets have constant mean curvature,
- (ii) three facets meet in an edge at an angle of 120° ,
- (iii) four edges meet in a node at tetrahedral angles ($\arccos(1/3) \approx 109.47^\circ$).

Therefore, each edge is shared by exactly three cells and each node exactly by four cells (and four edges), which corresponds to the property of normality of tessellations. The first model for soap froth can be historically identified in Kelvin's solution to the problem proposed by himself: a tessellation of space into cells of equal volumes and minimal surface area (Weaire, 1996). The Kelvin cell is a truncated octahedron, that is, a polyhedron with 14 facets, of which 6 are squares and 8 are hexagons. This can be used to partition space. Besides, applying a curvature to the facets, it complies with Plateau's laws. A bit more than a hundred years later, a better solution to Kelvin's problem was proposed by Weaire and Phelan (1994). The Weaire-Phelan structure consists of two cells, an irregular dodecahedron and a polyhedron with 14 hexagonal and pentagonal facets. Plateau's laws are obeyed when the facets are curved. The question of whether this is the best structure to solve Kelvin's problem is still open. Although these deterministic models capture some of the characteristics of soap froth, it has been observed that the number of edges per facet in real soap froth varies considerably (Matzke, 1946). Therefore, random models have been looked at also for this application. The idea proposed in Kraynik et al. (2003) is to generate a random tessellation and then *relax* it in order to obtain a more regular structure that complies with Plateau's laws. More details are given in Section 4.4.1.

The several techniques employed in industrial production influence the physics of the solid foams. However, it is not possible to theoretically predict how far the manufactured product is from Plateau's equilibrium. In general, open cell foams are more regular than closed cell foams. This is due to the fact that the material on the facets had enough time to drain off. For example, the polymer closed foams analyzed in Section 4.3.3 show rather flat walls. We model foams with normal tessellations. Simulations of mechanical properties on such models proved significative for both open and closed cell foams (Kanaun and Tkachenko, 2006; Liebscher et al., 2012; Redenbach et al., 2012b; Wejrzanowski et al., 2013). Moreover, all normal tessellations in \mathbb{R}^d with $d \geq 3$ can be interpreted as Laguerre tessellations (Lautensack and Zuyev, 2008). This is the reason why considering only models based on Laguerre tessellations is not a restricting choice. We will first define the *Voronoi tessellation*, or *Voronoi diagram*. Then, the definition is generalized to obtain *Laguerre tessellations*, or *power Voronoi diagram*. More details and other variations on Voronoi diagrams can be found in Okabe et al. (2000).

4.2.1 Voronoi tessellations

A cell of a Voronoi tessellation is simply defined as the region of points closest to a given point in the generated point process.

Definition 4.2.1 (Voronoi tessellation)

Let Φ be a point process in \mathbb{R}^d , then the *Voronoi tessellation* T_Φ generated by Φ is the collection of cells

$$C_V(x, \Phi) = \{y \in \mathbb{R}^d : \|y - x\| \leq \|y - x'\|, \forall x' \in \Phi\}, \quad x \in \Phi.$$

Consequently, each point in Φ generates a cell and each cell contains its generator point in Φ . It is possible to construct Voronoi tessellations which are not normal. For instance, grid points generate cubical cells, such that each edge is shared by four, and each vertex by eight cells. Such tessellations are considered degenerated (Okabe et al., 2000) and will not be treated further. Moreover, assuming that the points in a realization of Φ are almost surely in *general position* yields that the generated Voronoi tessellation is almost surely normal. Furthermore, it holds that if Φ is stationary, then also T_Φ is stationary. We will restrict to stationary tessellations.

If Φ is a Poisson point process, the tessellation T_Φ generated by Φ is called *Poisson-Voronoi* (PV) tessellation. In this case, Φ , and thus T_Φ , are completely determined by the intensity λ of the Poisson point process. Furthermore, all the model characteristics are determined by the only model parameter λ via analytical formulae. Whereas the complete randomness of Poisson point processes was an advantage to model fiber systems, it is drawback when considering foams. In fact, models generated by PV tessellations yield structures that are often too irregular to embed the geometry of real foams (Fan et al., 2004). For instance, cells can be arbitrarily small (points can be arbitrarily close). Furthermore, the mean number of facets per cell is around 15.5 for PV, while in real foams this number is usually smaller. Nevertheless, we will consider PV tessellations further as the reference model for random tessellations.

Naturally, a more regular point process yields more regular structures. This can be obtained by considering a *hard-core point process*: the distance between each pair of points

is larger or equal to a given positive length. The terminology is analogous to hard-core fiber systems. In fact, one can think of a hard-core point process as the process of the centers of a hard-core system of spheres with constant radii. With this model, it is possible to control the minimal cell size, however, we lose the possibility of an analytical formulation of the geometric characteristics without gaining control on the volume distribution.

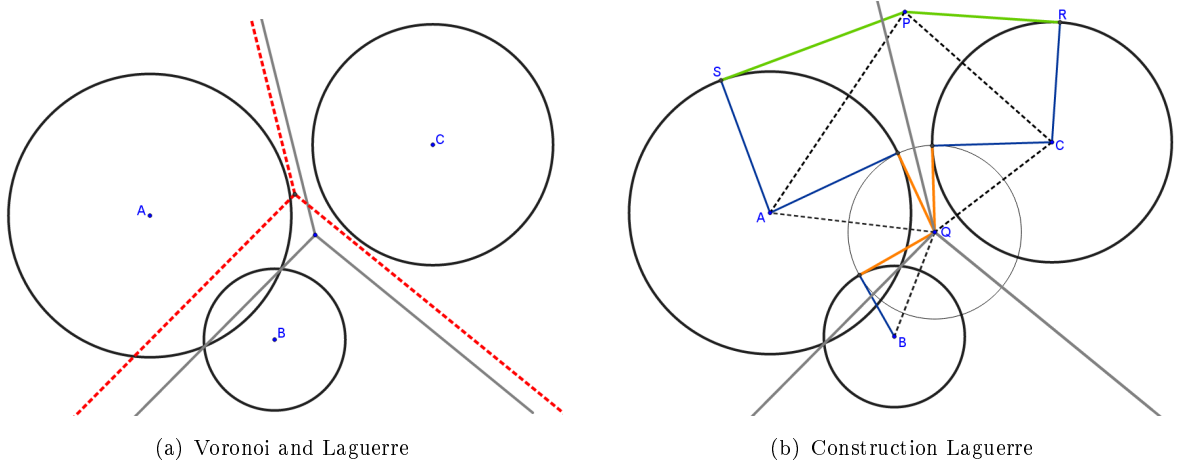


Figure 4.1: Tessellations generated by the system $S = \{A, B, C\}$. Left: comparison between the Voronoi tessellation (dashed red lines) and the Laguerre tessellation (grey lines) for which the region of influence of the generating points is weighted on the radii of the circles centered in the points. Right: construction of the Laguerre tessellation. The point P belongs to the cell generated by C because $\overline{PR} < \overline{PS}$, whereas the point Q is the vertex between the three cells, in fact, the orange segments have the same length.

4.2.2 Laguerre tessellations

An advantage of considering Laguerre tessellations is that the cell volume distribution can be controlled. To achieve this, a *weight* or *power* is assigned to each generating point. The cells, interpreted as regions of influence of the points, are defined accounting for the weights. Instead of using Euclidean distance, we rely on a *power distance* of the point $y \in \mathbb{R}^d$ to the point $x \in \mathbb{R}^d$ with power r (Okabe et al., 2000):

$$d_{pw}(y, x, r) = \|y - x\|^2 - r^2.$$

In Figure 4.1(a), the Voronoi and Laguerre tessellations generated by three points are compared. To generate the Laguerre cells, the power of each point is the radius of the corresponding circle.

Definition 4.2.2 (Laguerre tessellation)

Let Φ be a marked point process in $\mathbb{R}^d \times \mathbb{R}^+$, then the *Laguerre tessellation* T_Φ generated by Φ is the collection of cells

$$C_L((x, r), \Phi) = \{y \in \mathbb{R}^d : \|y - x\|^2 - r^2 \leq \|y - x'\|^2 - r'^2, \forall (x', r') \in \Phi\}, \quad (x, r) \in \Phi.$$

If the mark space is reduced to one point in \mathbb{R}^+ , i. e., all the points have the same weight, then the Laguerre tessellation has realizations identical to those of the Voronoi tessellation of the ground point process.

The definition of the marked point process Φ can be extended to negative marks. The Laguerre tessellation is well defined also in this case. However, restricting to the positive real numbers simplifies the geometric interpretation of the model. In fact, Φ can be seen as a system of spheres. Then, deciding to which cell a point y belongs, is based on a geometric construction shown in Figure 4.1(b). It is possible that some spheres do not generate any cell and also that some spheres do not intersect the cell they generate.

To realize Laguerre tessellations, we do not use the construction depicted in Figure 4.1(b), but we exploit the duality with the Delaunay triangulation (Okabe et al., 2000). The algorithm is outlined in Sugihara (2000). Let us suppose to deal with a finite set of generating points $S = \{(x_0, r_0), \dots, (x_n, r_n)\}$ belonging to a compact convex domain $W \subset \mathbb{R}^d$. For each point, we define a point in \mathbb{R}^{d+1} such that the first d coordinates are those of x and the last coordinate is given by $\|x\|^2 - r^2$. We compute the convex hull of this set of points. By projecting the lower hull onto W , we obtain the Delaunay triangulation generated by S . Thanks to duality, each vertex of the Delaunay triangulation corresponds to a cell of the Laguerre tessellation and each edge to a neighborhood relation, thus the Laguerre tessellation can be completely reconstructed. It is important to notice that once the sphere system is given, the tessellation is completely determined.

As for Voronoi tessellations, particular point patterns yield degenerate tessellations. Nevertheless, if the points are in general position (Okabe et al., 2000), then Laguerre tessellations are normal. Moreover, every normal tessellation in \mathbb{R}^d with $d \geq 3$ can be constructed as a Laguerre tessellation (Lautensack and Zuyev, 2008).

If the ground process Φ_0 is a Poisson point process, we talk about *Poisson-Laguerre tessellations*. The only parameters of this model are the intensity of the point process and the radius distribution. This case is widely treated in Lautensack (2007). Good theoretical results are found concerning the mean characteristics and the Palm distribution corresponding to M_k .

Hard-core sphere systems yield the advantage that each sphere generates a cell in which it is contained. These systems are often found in literature as *random close packings* (RCP) even though generated with different algorithms. The simplest choice to model hard-core spheres is the RSA algorithm (Section 3.3.1). However, volume fractions that can be achieved with arbitrary volume distribution are rather low. Therefore, packing based on global rearrangements are often preferred (Fan et al., 2004; Kraynik et al., 2003; Redenbach, 2009). Following Redenbach (2009), we model the sphere packing with the force-biased (FB) algorithm presented in Bezrukov et al. (2002). It is a variation on the molecular dynamics approach employed for instance in Kraynik et al. (2003). Initially, all the random spheres are generated according to a given radius distribution and are inserted in an observation window in uniformly distributed positions. In each iteration step, the radii of the spheres are modified and centers are shifted to reduce overlapping. The process stops when overlapping is completely avoided or when the desired volume fraction is reached. Up to a scaling factor, the initial size distribution is preserved. There are some technical parameters to be set. However, we fix them according to Redenbach (2009) to obtain rather regular configurations. Some realizations of the sphere packings and the corresponding tessellations are shown in Figure 4.2.

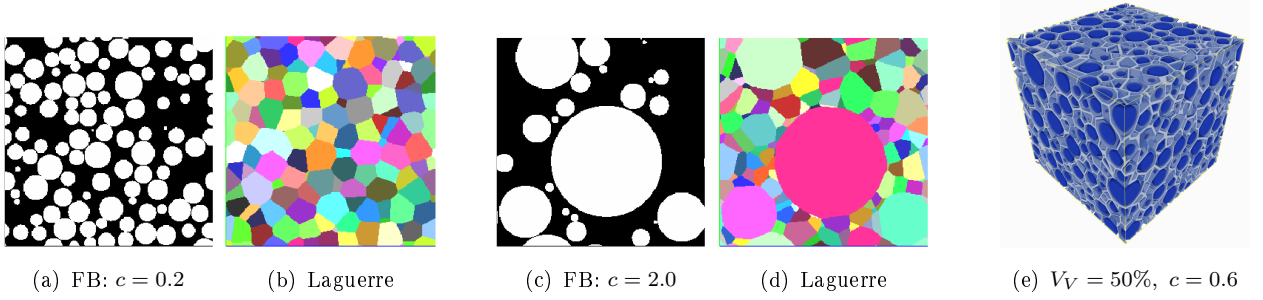


Figure 4.2: (a)-(d): 2d sections of two realizations of force-biased sphere packings in 3d with $V_V = 50\%$ and $c = 0.2$ (left), $c = 2.0$ (center) and corresponding Laguerre tessellations. (e): volume rendering of a force-biased system of spheres with $V_V = 50\%$ and $c = 0.6$ and the edge system of the corresponding Laguerre tessellation.

One advantage of this model is that it depends on only few parameters: the intensity of the spheres, the desired volume fraction V_V , and the radius distribution. The latter depends on the coefficient of variation c and on the mean sphere volume, which is equal to the mean cell volume times the volume fraction. Which distributions are considered and how to estimate the model parameters from images of samples are topics of the next section. A drawback of this model is that there are no analytical expressions for the characteristics of the tessellation obtained from a force-biased packing. Nevertheless, this problem has been overcome by the results published in Redenbach (2009). More details are given in the next section.

Unless otherwise specified, from now on by “model” we will refer to random Laguerre tessellations generated by force-biased sphere packings.

4.3 Model fitting for foams

In this section, we present a well established technique to fit random Laguerre tessellations to samples of foams. Moreover, we investigate the possibility to enrich the set of features classically used in model fitting. In particular, we aim at improving the fit, while still permitting the automatic determination of the parameters of the best-fitting model. The problem of estimating geometric characteristics from the images will be addressed in Section 4.3.3.

When the coefficient of variation of the volumes is close to zero, we talk about *monodisperse* foams. Foams with high variability in the cell size distribution are called *polydisperse*. Two volume distributions are typically employed to model foams' cell size: lognormal, which is also observed in polycrystals (Rhines and Patterson, 1982; Okazaki and Conrad, 1972), and gamma, which corresponds to the volume distribution in PV tessellations. Both gamma and lognormal distributions depend on two parameters which can be controlled by the mean sphere volume and the coefficient of variation c .

The gamma distribution depends on a shape parameter $a > 0$ and a scale parameter $s < 0$ and has the following density

$$f(x) = \frac{x^{a-1} e^{-\frac{x}{s}}}{s^a \Gamma(a)}, \quad x \geq 0. \quad (4.10)$$

The mean is as and the variance is as^2 . The density of a lognormal distribution with mean $\mu \in \mathbb{R}$ and standard deviation $\sigma \geq 0$ is

$$g(x) = \frac{e^{-\frac{(\log x - \mu)^2}{2\sigma^2}}}{\sqrt{2\pi}\sigma x}, \quad x \geq 0. \quad (4.11)$$

Moreover, if the sphere volume has lognormal distribution, then the radius is also lognormally distributed with mean $\frac{1}{3}(\mu + \ln(\frac{3}{4\pi}))$ and variance $\frac{\sigma^2}{9}$. Unfortunately, radii of spheres with gamma distributed volumes cannot be expressed via a known distribution.

The parameters of the volume distributions in terms of the model parameters for gamma distribution are

$$a = \frac{1}{c^2} \text{ and } s = \frac{c^2 V_V}{N_V}$$

and for the lognormal distribution

$$\mu = \frac{1}{2} \log \left(\frac{V_V^2}{N_V^2 (c^2 + 1)} \right) \text{ and } \sigma^2 = \log(c^2 + 1),$$

where N_V is the number of spheres in a unit volume.

Note that the volume distribution is not directly fitted to the empirical distribution estimated from a sample. Instead, the volume distribution is considered an unknown parameter as volume fraction and coefficient of variation of the sphere packing. The parameters generating the best-fitting model are found employing the procedure presented in Lautensack (2007). It is based on the minimization of a distance function between N characteristics estimated on the foam sample \hat{m}_i and the corresponding characteristics of the model m_i :

$$d(\hat{m}, m) = \sqrt{\sum_{i=1}^N \left(\frac{\hat{m}_i - m_i}{\hat{m}_i} \right)^2}. \quad (4.12)$$

The characteristics considered are first and second moments of volume, surface area, mean width, and number of facets per cell of the typical cell, hence $N = 8$.

This approach is independent of the choice of the model. However, it depends on the model whether the characteristics m_i benefit of an analytical expression. If not, it is necessary to proceed by simulations. As mentioned before, for Laguerre tessellations generated by FB sphere packings, it is possible to approximate the characteristics depending on the model parameters (Redenbach, 2009). An analysis based on Monte-Carlo simulations of the model with varying parameters showed that mean values and standard deviations of V , S , \bar{b} , and F_C are well approximated by third degree polynomials in the coefficient of variation, depending on the volume fraction and on the volume distribution. Gamma and lognormal distributions of the volumes and four values of the volume fraction are sampled: $V_V = 30\%, 40\%, 50\%, 60\%$. Therefore, we can write

$$d(\hat{m}, p_{V_V, i}(c)) = \sqrt{\sum_{i=1}^N \left(\frac{\hat{m}_i - p_{V_V, i}(c)}{\hat{m}_i} \right)^2}. \quad (4.13)$$

Now, the minimization of this function with respect to c , V_V and the volume distribution can be done automatically. Thus, also the model fitting is completely automated. The open question is if it is possible to improve this procedure.

Distances other than Euclidean have been analyzed in Lautensack (2007), however, they yield no qualitative difference. Another possibility for improvement is to sample other volume fractions in order to represent the dependency of the characteristics as a two-dimensional manifold depending continuously on (V_V, c) . This idea has not been investigated further because it is not possible to finely control V_V in realizations of the sphere packings. Therefore, we decided to enrich the set of characteristics used to fit the model. Moreover, for Poisson-Voronoi tessellations high correlations between the size features have been observed (Okabe et al., 2000), whereas angles show low correlation with the four characteristics we considered so far. The question we aim to answer is whether it is possible to include angles into this framework for model fitting and what advantages would result. After analyzing the distributions of angles in random Laguerre tessellations, we will introduce a method to estimate these quantities from images of foams (Section 4.3.2).

V_V	c	θ_e				θ_3			
		min	max	mean	sd	min	max	mean	sd
30%	0.2	65.82°	151.21°	120.00°	10.19°	74.30°	146.13°	119.63°	10.28°
30%	2.0	21.52°	179.48°	120.00°	21.66°	28.12°	177.29°	114.07°	21.85°
60%	0.2	66.47°	148.34°	120.00°	11.48°	70.01°	145.74°	119.78°	11.40°
60%	2.0	11.92°	179.36°	120.00°	22.66°	17.52°	178.51°	110.82°	23.73°
PV		21.63°	178.58°	120.00°	23.80°	40.72°	173.65°	118.52°	23.84°

Table 4.1: Statistics for dihedral angles for some parameters of the model with gamma volume distribution.

V_V	c	α_v				α_3			
		min	max	mean	sd	min	max	mean	sd
30%	0.2	0.22°	179.85°	109.89°	16.97°	0.40°	179.70°	109.74°	16.99°
30%	2.0	0.04°	179.97°	109.80°	29.61°	1.09°	179.20°	107.30°	29.63°
60%	0.2	0.25°	179.82°	110.05°	20.13°	0.68°	179.61°	110.08°	19.80°
60%	2.0	0.35°	179.86°	109.09°	27.86°	0.42°	179.26°	104.61°	28.69°
PV		0.79°	179.71°	110.76°	35.74°	3.62°	179.61°	110.90°	35.43°

Table 4.2: Statistics for interior angles for some parameters of the model with gamma volume distribution.

4.3.1 Angles in Laguerre tessellations

In order to investigate angles in random Laguerre tessellations generated by FB sphere packings, we consider here the same simulations as investigated in Redenbach (2009): five realizations with 10000 spheres for each parameter set with $V_V = 30\%, 40\%, 50\%, 60\%$, $c = 0.2, 0.4, \dots, 2.0$ and gamma and lognormal volume distributions.

Let us assume that the tessellation is completely known, that is coordinates of the nodes, edges' and facets' equations, and all neighbor relations are known. For a cell C , the *dihedral angle* θ_e at edge e is the angle between the two facets of C sharing e . Let n and m be the outward unit vectors normal to the two facets in C adjacent to e , then

$$\theta_e = \pi - \arccos(n \cdot m), \quad (4.14)$$

where \cdot is the scalar product. Other interesting angles to measure are the ones between two edges on a facet. We refer to them as *interior* or *bond angles* (Kumar and Kurtz, 1995). We can measure an interior angle via the scalar product of the direction vectors of the adjacent edges.

Angles in tessellations were so far analyzed only for some special cases of Voronoi tessellations (Kumar and Kurtz, 1995; Lorz and Hahn, 1993). For the Poisson-Voronoi tessellation, a probability density function of the distribution of dihedral angles is given in Kumar and Kurtz (1995):

$$f(\theta) = \left(\frac{4}{3\pi}\right)(2\theta(2 + \cos 2\theta) - 3 \sin 2\theta) \sin^2 \theta$$

for $\theta \in [0, \pi]$. Considering the angles between all facet pairs gives a mean value equal to 120° , due to normality (independent of the model), and standard deviation 23.85° . In Lorz and Hahn (1993), instead, only one random angle per cell is taken into account. In this way, the mean value, estimated from simulations, is 118.5° and the standard deviation is about 10° . The mean interior angle with respect to all vertices in each cell is 111.14° , which is not far from the equilibrium angle 109.47° . Although Voronoi tessellations are a special case of Laguerre tessellations, the underlying Poisson point process yields a structure significantly different from the one obtained with non-overlapping spheres and varying radii. PV tessellations cannot be considered as a limit case for the Laguerre tessellations generated by systems of non-overlapping spheres for coefficient of variation going to zero. Tables 4.1 and 4.2 display some statistics of the angles calculated on simulations of Laguerre tessellations with extreme parameters and PV tessellations. Laguerre tessellations with low volume variations have mean values closer to Plateau's equilibrium than PV tessellations.

Following Lorz and Hahn (1993) and Okabe et al. (2000), we define θ_3 to be a randomly chosen dihedral angle per cell, where all the angles can be chosen with the same probability. In other words, θ_3 is the typical angle of a cell. The distribution of θ_3 is very similar to the distribution of θ_e computed on all edges of the tessellation. In Figure 4.3, the distribution of θ_3 for extreme values of the model parameters, V_V and c , is presented. While considering θ_e for all edges gives a mean value always equal to 120° due to normality, the mean values of θ_3 decrease as the tessellation becomes more polydisperse. At the same time, the variance grows. Naturally, a small coefficient of variation yields a more regular structure, thus nearer to Plateau's equilibrium. With a large coefficient of variation, some large cells with many facets occur. These cells typically tend to a spherical shape and are characterized by large angles between facets. However, the amount of small cells with irregular shape and typically smaller dihedral angles is much larger. Therefore, in this case, the mean value of θ_3 is smaller than in regular structures and the variance is higher. The relation between the mean value $\bar{\theta}_3$ and the standard deviation $\sigma(\theta_3)$ depending on the model parameters can be seen in Figure 4.4. The values for each parameter set are obtained by ten independent extractions of θ in each cell. The variances of the repeated extractions are however very small, both for $\bar{\theta}_3$ and $\sigma(\theta_3)$, thus suggesting that these characteristics are stable. Mean value and standard

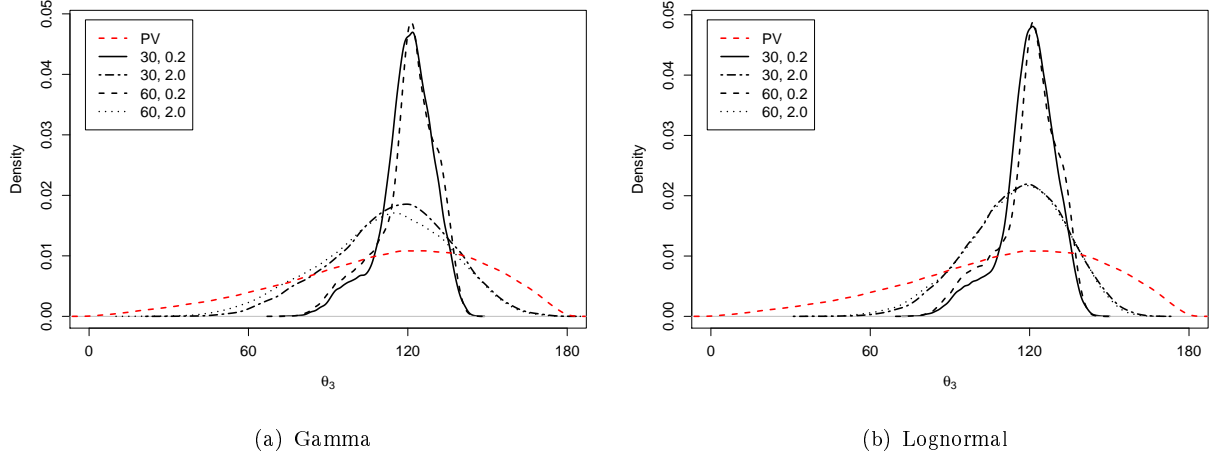


Figure 4.3: Densities of θ_3 for Poisson-Voronoi tessellation and Laguerre tessellation with $V_V = 30\%, 60\%$ and $c = 0.2, 2.0$. Left: gamma volume distribution. Right: lognormal volume distribution.

deviation can be fitted by third degree polynomials in c for each V_V and volume distribution (see Appendix A for the coefficients). Therefore, it is possible to use dihedral angles in the distance function in Equation (4.13) and still minimize it automatically. Note that for coefficients of variation smaller than 1.0, the volume fraction does not influence the mean values.

Proceeding analogously for interior angles, we define α_3 as a randomly chosen interior angle of the typical cell, such that all the interior angles of the cell can be chosen with the same probability. The densities of α_3 for some values of the model parameters are shown in Figure 4.5. Considering that a cell has an average of about 14 facets, which are most likely to have 5 edges, there are about 70 interior angles in a cell. Choosing only one among them might not yield enough information. Again, we considered ten independent extractions of α_3 in each cell. The variance of mean and standard deviation of α_3 were higher than for dihedral angles, especially in the case of the lognormal distribution. Nevertheless, the graphs in Figure 4.6 show that there are close relations to the model parameters. The mean values of interior angles decrease and standard deviations grow as the tessellations become more polydisperse. For the lognormal volume distribution, the range of the mean and standard deviation is very small. For both distributions, it is possible to fit third degree polynomials to $\bar{\alpha}_3$ and $\sigma(\alpha_3)$ (coefficients in Appendix A) and thus employ interior angles in automatic model fitting, too.

Minimizing the distance function in Equation (4.13) with respect to the angles, too, sums up to $N = 12$ characteristics. The next step is to verify if some of the characteristics hold redundant information and thus can be excluded from the model fitting.

Correlation analysis

Figure 4.7 represents the pairwise correlation matrices of V , S , \bar{b} , F_C , θ_3 and α_3 for Laguerre tessellations with $V_V = 60\%$ and coefficient of variation 0.2 and 2.0. Values of the correlations for less dense packings are summarized in Table 4.3 together with the correlation coefficients

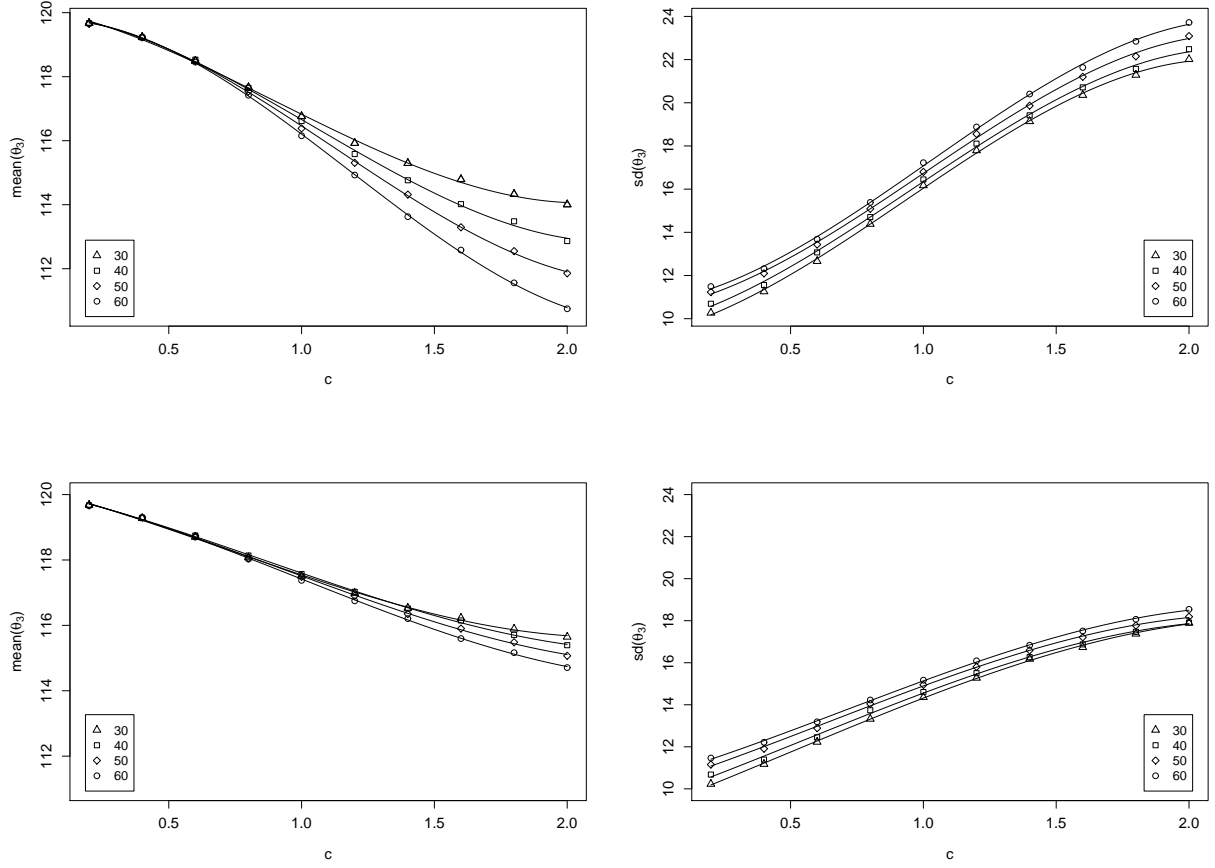


Figure 4.4: Mean (left) and standard deviation (right) of θ_3 versus the coefficient of variation c for volume fraction $V_V = 30\%, 40\%, 50\%, 60\%$ with fitted polynomials. Top: gamma volume distribution. Bottom: lognormal volume distribution.

for Poisson-Voronoi diagrams from Okabe et al. (2000). From the pairwise plots, it is easy to see that the size measures, V , S and \bar{b} , are strongly related, with an approximately linear dependency. The angles, however, plotted against the other characteristics form clouds suggesting low correlations.

The relations among these characteristics can be analyzed more thoroughly by a principal component analysis (PCA). As expected, the angles contain the most variability in the data. Volume and surface area appear redundant. The graphical representation of the principal components shows that all the size features, V , S and \bar{b} , contain similar information which strongly differs from the information carried by θ_3 and α_3 . The number of facets per cell F_C is more related with dihedral angles than with interior angles. The same effect can be seen in Table 4.3: the correlation of dihedral angles with F_C is higher than their correlation with the size characteristics. Intuitively, both dihedral angles and the number of facets per cell contain information about the shape of the polyhedron. Figure 4.8 shows how θ_3 correlates with V and F_C and depends on the model parameters. The trends of the correlations with S and \bar{b} are analogous. The interior angle α_3 has small correlation coefficients with respect to all the other characteristics. Its correlation with the volume, Figure 4.9, varies on the

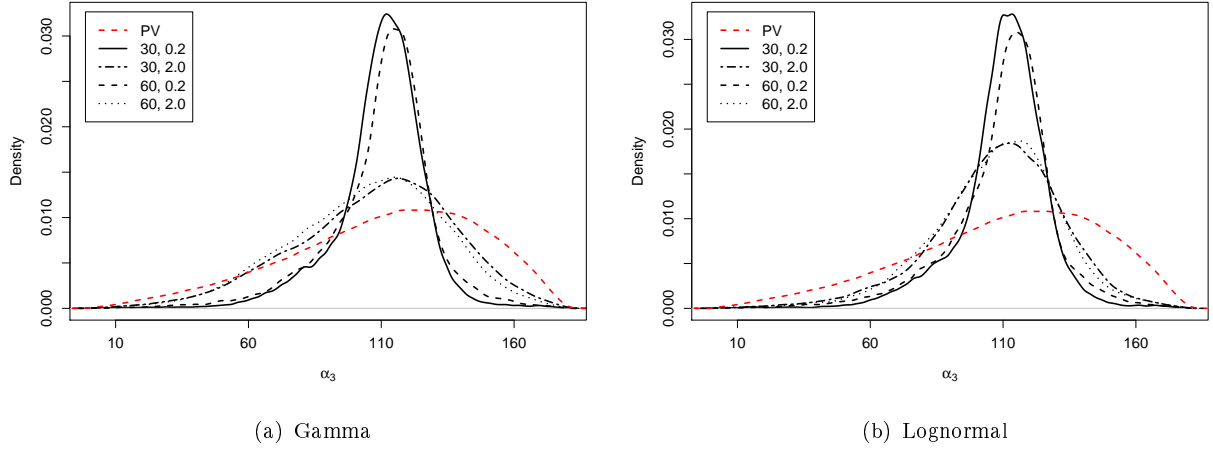


Figure 4.5: Densities of α_3 for Poisson-Voronoi tessellation and Laguerre tessellation with $V_V = 30\%, 60\%$ and $c = 0.2, 2.0$. Left: gamma volume distribution. Right: lognormal volume distribution.

model parameters with the same trend as the correlation between θ_3 and the volume, but with smaller values. These trends can be explained by the structural differences occurring with different coefficient of variation.

V_V	c	V, θ_3	S, θ_3	\bar{b}, θ_3	F_C, θ_3	V, α_3	S, α_3	\bar{b}, α_3	F_C, α_3	θ_3, α_3
30%	0.2	0.209	0.203	0.168	0.278	0.044	0.043	0.033	0.064	0.040
30%	2.0	0.429	0.458	0.459	0.488	0.118	0.132	0.137	0.144	0.041
60%	0.2	0.194	0.192	0.165	0.249	0.043	0.044	0.040	0.061	0.040
60%	2.0	0.487	0.547	0.572	0.573	0.174	0.207	0.226	0.222	0.114
PV		0.187	0.180	0.170	0.247*					

Table 4.3: Correlation coefficients between the characteristics of Laguerre tessellations with gamma volume distribution. Values for Poisson-Voronoi for comparison, from Okabe et al. (2000). *Value for number of edges per cell $N_{13} = 2F_C - 4$.

4.3.2 Estimation of angles from images

In this section, we outline how to extract geometric and topological characteristics of a tessellation from an image. First, we reconstruct the whole topology of the tessellation, then the angles can be calculated. The method we introduce can be applied on images of tessellations obtained as digitalizations of models or as reconstructions from μ CT images of foam samples. We will exploit realizations of Poisson-Voronoi tessellations to validate the proposed method.

We assume that the observed tessellation is face-to-face, normal and with convex polyhedral cells. The tessellation is observed on an image such that each connected component has a unique label and two different labels are separated by a layer of background pixels

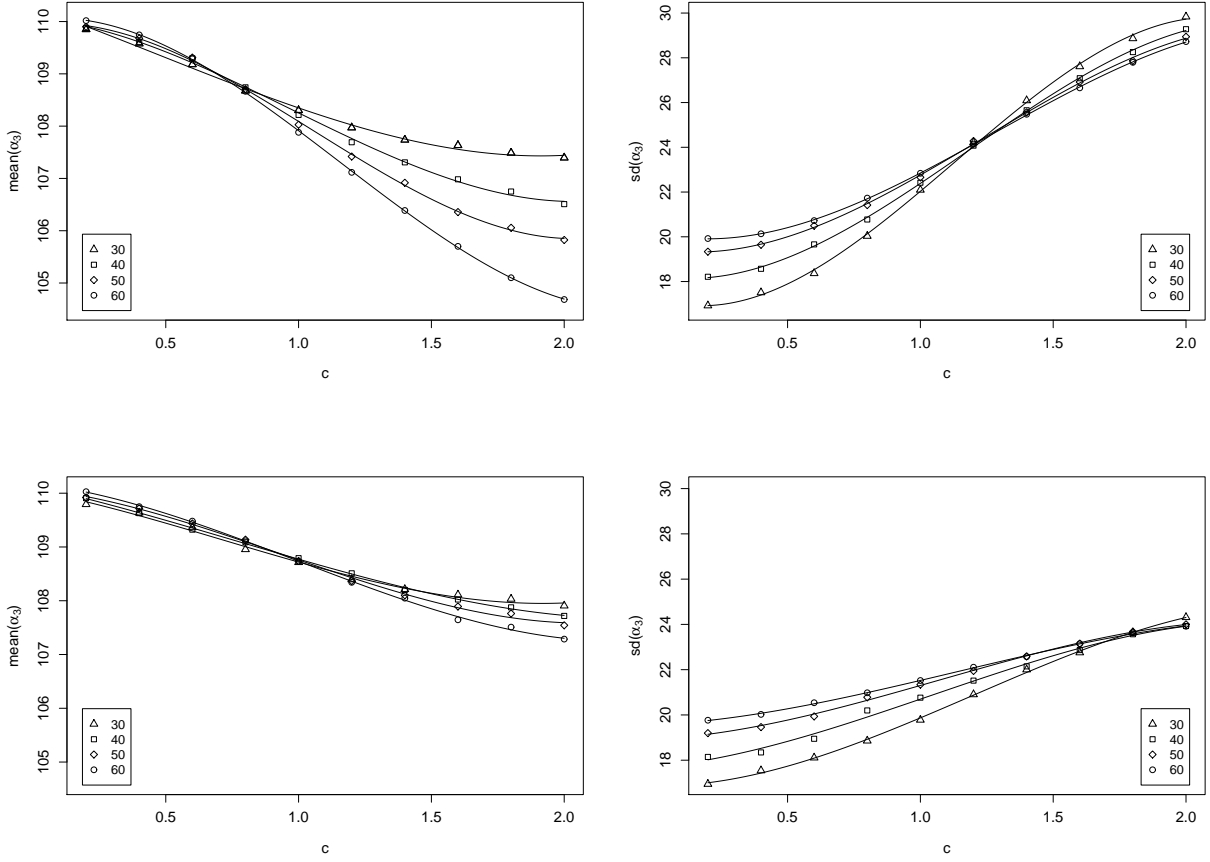


Figure 4.6: Mean (left) and standard deviation (right) of α_3 versus the coefficient of variation c for volume fraction $V_V = 30\%, 40\%, 50\%, 60\%$ with fitted polynomials. Top: gamma volume distribution. Bottom: lognormal volume distribution.

(one pixel thick). Any image that complies with these assumptions can be used in our algorithms, no matter how it is produced. For our applications it is convenient to exploit images generated by the watershed transform as they are already needed for the segmentation of the cells, Figures 4.18(d) and 4.19(d) (details on the cell reconstruction are given in Section 4.3.3). The method can be adapted to image of space filling tessellations with few modifications. Later, we will discuss the consequences of dealing with the image of a tessellation that does not comply with the assumptions of normality and convexity of the cells. Note that the topological reconstruction is strongly based on the identification of neighbors. The neighborhood should be chosen accordingly to the adjacency system employed in the cell reconstruction.

The idea behind the algorithm is the following:

- (i) classify background pixels according to the number of pixels in their neighborhood (Figure 4.10):
 - two neighbors \rightarrow facet pixel,
 - three neighbors \rightarrow edge pixel,

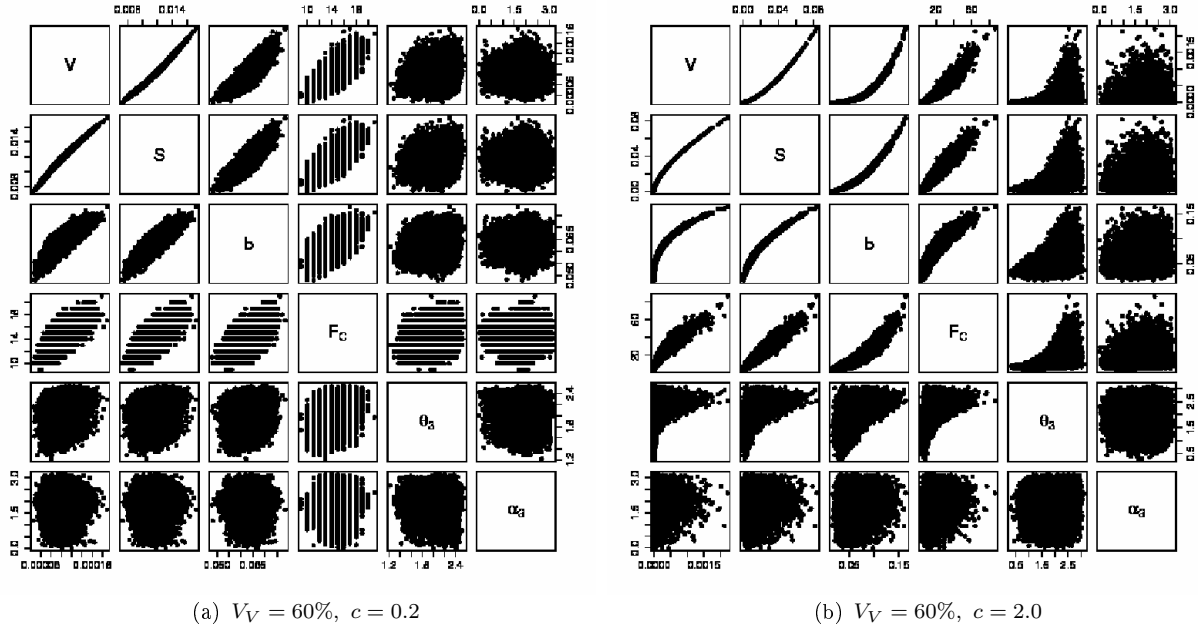


Figure 4.7: Pairwise correlation between volume (V), surface area (S), mean width (b), number of facets per cell (F_C), dihedral angle (θ_3) and interior angle (α_3) for volume fraction $V_V = 60\%$, coefficient of variation $c = 0.2$ (left) and $c = 2.0$ (right), with gamma volume distribution. Note that F_C has only discrete values and the range for tessellations with $c = 0.2$ is much smaller than with $c = 2.0$.

- four (or more) neighbors \rightarrow node pixel;
- (ii) from the knowledge of nodes (coordinates) and their neighboring cells, define facets and edges of the tessellation:
 - a facet between two neighboring cells,
 - an edge between two nodes sharing three neighboring cells;
- (iii) compute the direction vector of each edge and the normal to each facet;
- (iv) compute angles as in the case of analytically known tessellations.

The skeleton classification in step (i) relies strongly on the property of normality of the structure. Alternative algorithms, as the one presented in Saha and Chaudhuri (1996), are based on the analysis of $3 \times 3 \times 3$ pixel configurations: the positions of other skeleton pixels in the neighborhood determine how to classify the pixel. An analogous procedure is applied in Arganda-Carreras et al. (2010) to analyze biological tissues. Here however, we deal with complex structures with a high number of intersections and loops that may reduce the efficiency and reliability of these methods. Therefore, to analyze foams it is wiser to use the additional information of neighboring cells.

Although we assumed to observe normal tessellations, Plateau's laws apply only for dry soap froth. The algorithm is designed to detect pixels with more than four different neighboring cells. These are first identified as nodes, however, it is necessary to look at the

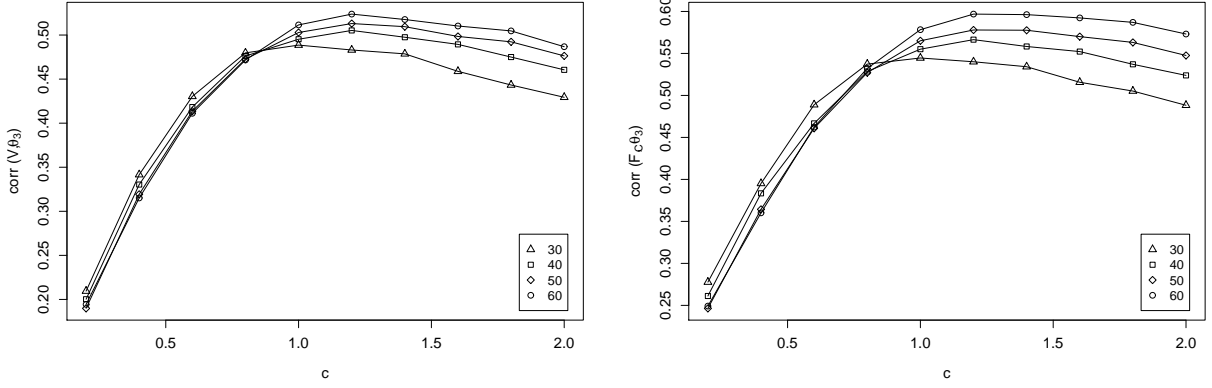


Figure 4.8: Correlation of θ_3 with V (left) and F_C (right) for Laguerre tessellation with varying parameters and gamma volume distribution.

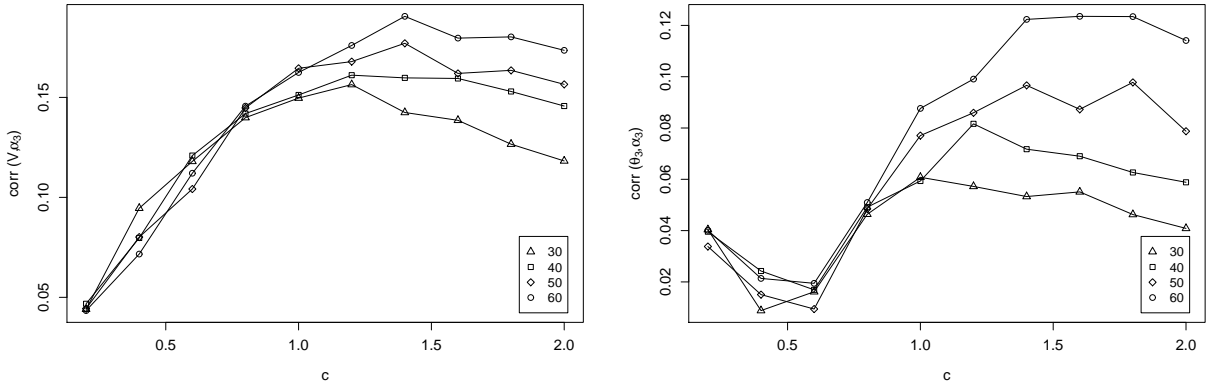


Figure 4.9: Correlation of α_3 with V (left) and θ_3 (right) for Laguerre tessellation with varying parameters and gamma volume distribution.

image to correctly classify the structure locally. Often, a node belonging to more than four cells is due to discretization of short edges and can occur in images of normal tessellations, too. In case the tessellation is not normal, an edge could belong to four cells, thus its pixels would be classified as nodes. Nevertheless, the extreme points of such an edge belong to five cells and thus are identified by our algorithm and the local non-normality of the foam is detected.

It is common to find several pixels for only one node in the tessellation. This is again due to discretization. A robust method to recognize such clusters of nodes consists in looking at the neighboring labels. Thus, we identify a “node-cluster” with all the pixels sharing the same set of neighboring cells. The coordinates of the node are obtained as average of the pixels’ coordinates in the cluster. The idea is that the real node lies in the center of the pixels classified as nodes. It is not necessary to modify the values of the classified pixels in the image. In fact, for the following steps only the nodes’ coordinates and their neighboring cells are necessary. Applying the rules due to normality expressed in step 2, the whole

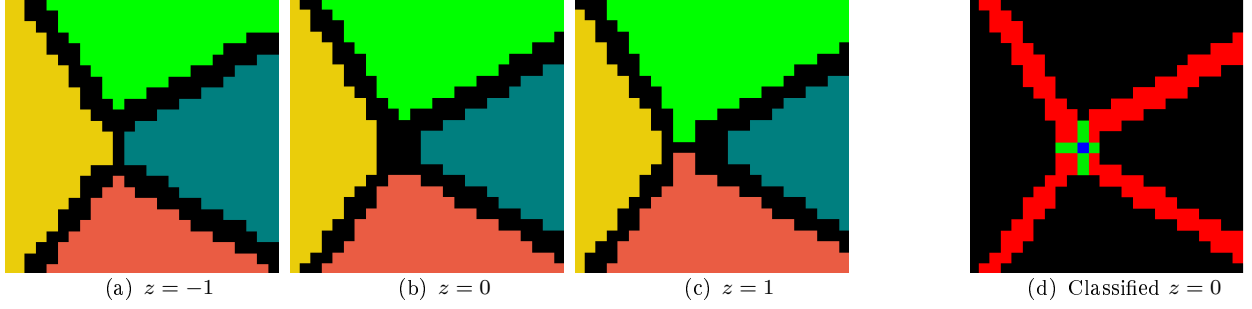


Figure 4.10: Three sequential 2d sections of reconstructed cells with watershed and classified skeleton corresponding to the middle one. Classification depends on the N26-neighborhood: red for facet pixels, green for edge and blue for node.

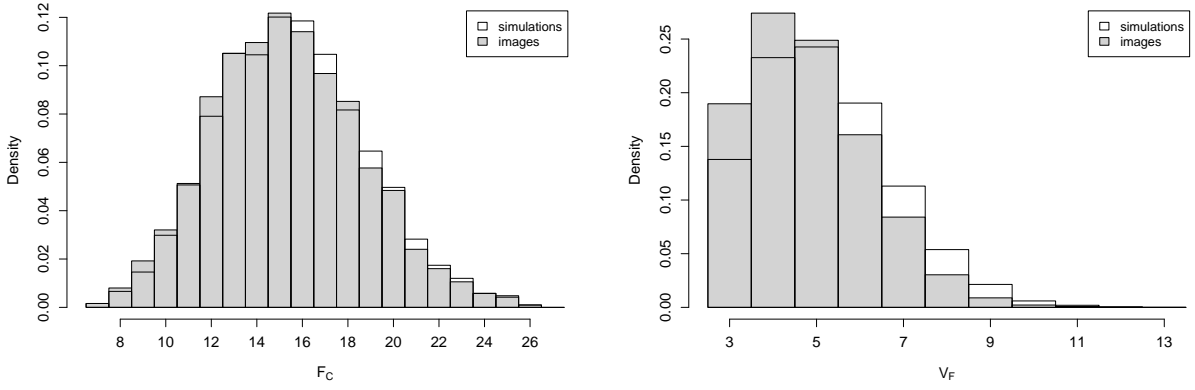


Figure 4.11: Validation on Poisson-Voronoi tessellation. Comparison of number of facets per cell (left) and number of vertices per facet (right) computed analytically and estimated from the images.

tessellation can be reconstructed, i. e., assign facets and edges to each cell, vertices to edges and to facets, edges to facets and vice versa.

The computation of the normals to the facets in step 3 is also affected by discretization. In general, three vertices suffice to compute the normal: consider the unit vectors corresponding to the edges between one vertex and the other two, their cross product gives the direction of the perpendicular to the plane determined by the points. However, here we have to account for the fact that the nodes of a real foam are not coplanar, hence the vertices detected from the image, in general, do not lie in a plane. For this reason, we take all triplets of vertices, compute the corresponding normals, and then average.

We remark that since we assumed the convexity of the cells, we could exploit an alternative approach to reconstruct the cells in the tessellations. After extracting the nodes from the image as above, we can define a cell as the convex hull of its nodes. Then, we only need to compute dihedral and interior angles of the convex hull. Nevertheless, with this approach, additional facets and edges are generated due to the fact that the vertices of a facet are not always coplanar. This causes a bias in the distribution of the dihedral angles, namely a peak close to 180° . Unfortunately, there is no information in the convex hull that allows us

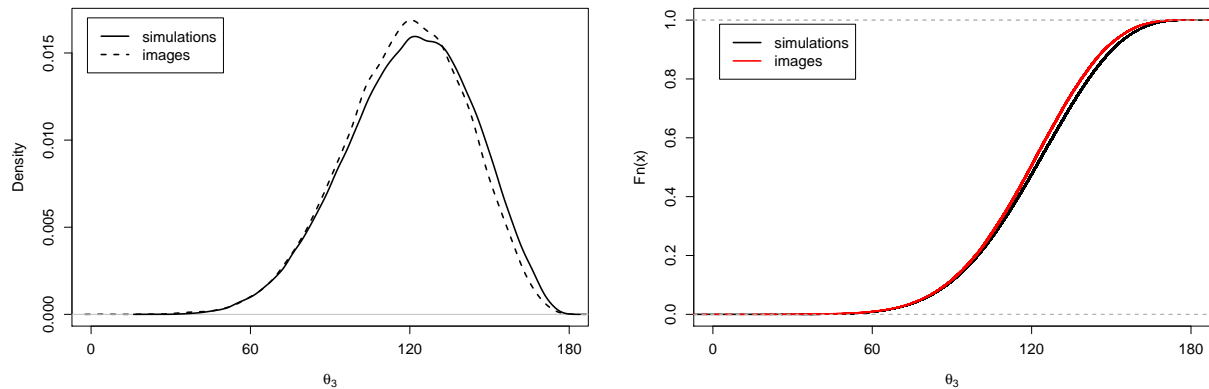


Figure 4.12: Validation on Poisson-Voronoi tessellation. Comparison of θ_3 computed analytically and estimated from the images. Left: density, right: empirical cumulative distribution function.

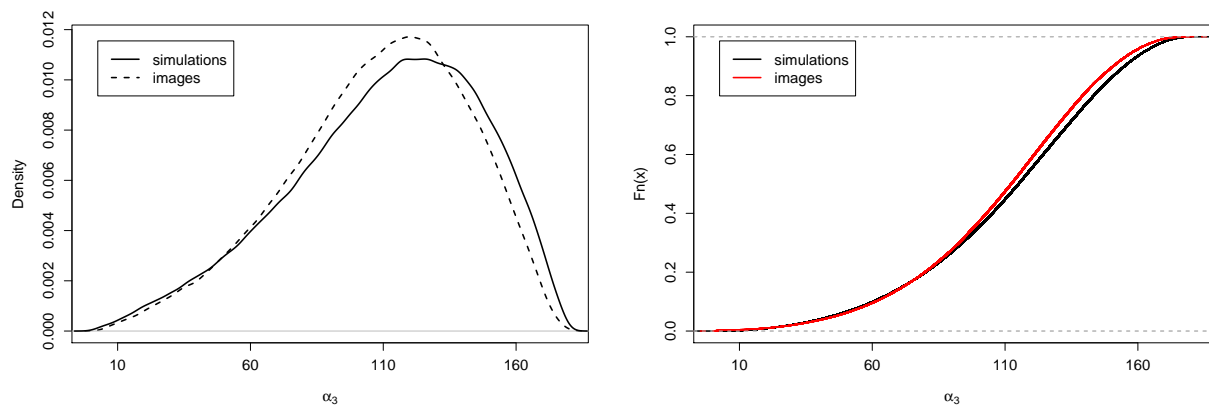


Figure 4.13: Validation on Poisson-Voronoi tessellation. Comparison of α_3 computed analytically and estimated from the images. Left: density, right: empirical cumulative distribution function.

to recognize the additional facets, therefore the reconstruction based on neighbors is more reliable. Moreover, this is computationally cheaper than generating the convex hull for each cell.

Validation

First, we analyze our estimation method on discretized realizations of Poisson-Voronoi tessellations. We generate five realizations with 1000 cells each. We compare characteristics calculated from the simulations, i. e., with the knowledge of the analytical coordinates of the nodes and edges' and facets' equations, and the characteristics estimated from images of the tessellations. In this case, edges and facets are reconstructed by a watershed transform to simulate the cell reconstruction from μ CT images. The periodicity in the model realizations is lost with cell reconstruction. Therefore, to avoid edge effects, we apply minus sampling

(Ohser and Schladitz, 2009). Cells lying outside the minus sampling window are counted as neighbors but are not analyzed. The same approach is used when dealing with images of real samples.

As expected, the estimation of angles can be improved by increasing the image size, i. e., increasing resolution. However, for samples of 1000 cells, it is sufficient to use images of 600^3 pixels. With images of 800^3 pixels, the enhancement in the estimations is so little that is not worth the additional computational effort. Discretization errors are also due to the skeleton pixels in the images: tessellations are by definition space-filling, thus background pixels are artificial and are only an approximation of the real zero-dimensional boundaries.

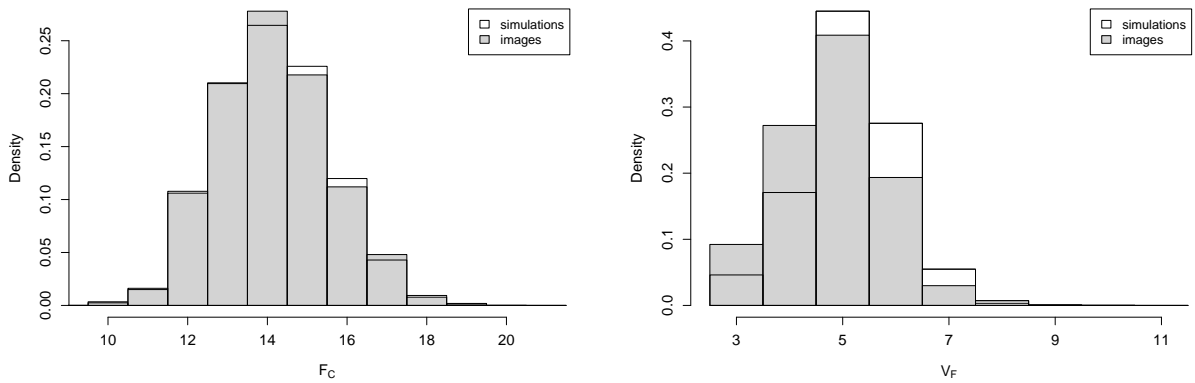


Figure 4.14: Comparison of number of facets per cell (left) and number of vertices per facet (right) computed analytically and estimated from the images. $V_V = 60\%$, $c = 0.2$ and gamma volume distribution.

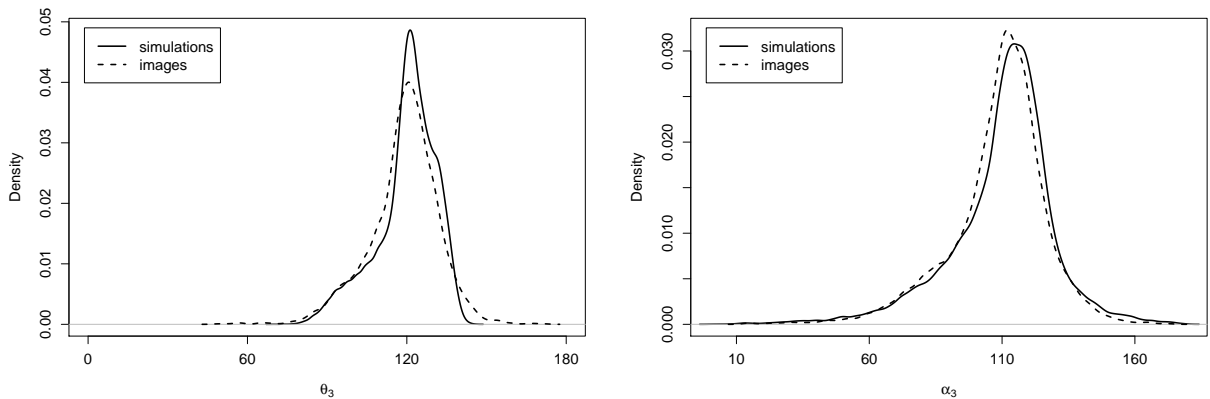


Figure 4.15: Comparison of θ_3 (left) and α_3 (right) computed analytically and estimated from the images. $V_V = 60\%$, $c = 0.2$ and gamma volume distribution.

The estimations of some topological numbers are presented in Figure 4.11. The number of facets per cell F_C is estimated very well from the images. However, the number of vertices per facet N_{20} is underestimated in the images. This suggests that some vertices are not found by the analysis of the skeleton. A closer look at the images shows that some vertices

are not correctly classified by our algorithm because the watershed skeleton is locally “too large”: around positions where there should be a node of the tessellation, no background pixel has four different labels in its neighborhood. Nevertheless, by comparing the number of vertices and number of edges reconstructed, it is possible to correct the estimation of N_{20} . However, we can only correct the number of vertices, but cannot know their positions. Since N_{20} is not a characteristic necessary for model fitting, this correction is not carried out.

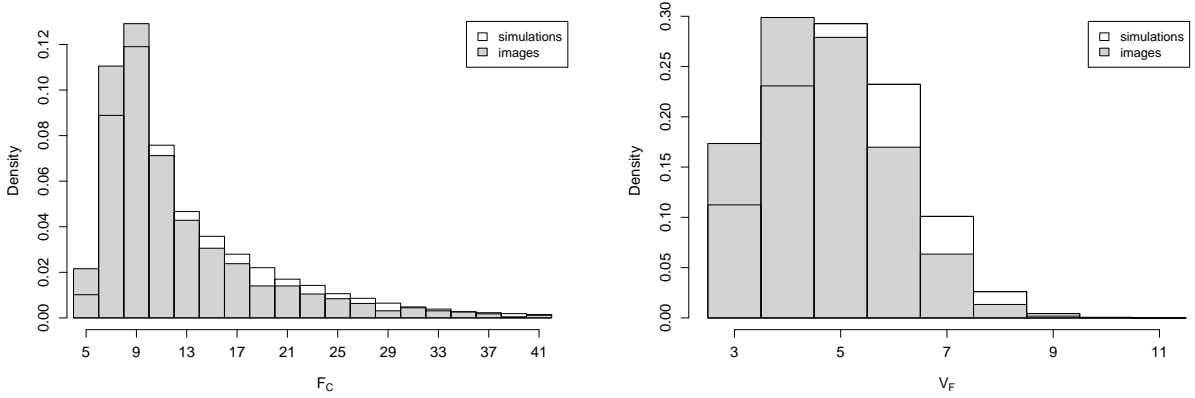


Figure 4.16: Comparison of number of facets per cell (left) and number of vertices per facet (right) computed analytically and estimated from the images. $V_V = 60\%$, $c = 2.0$ and gamma volume distribution.

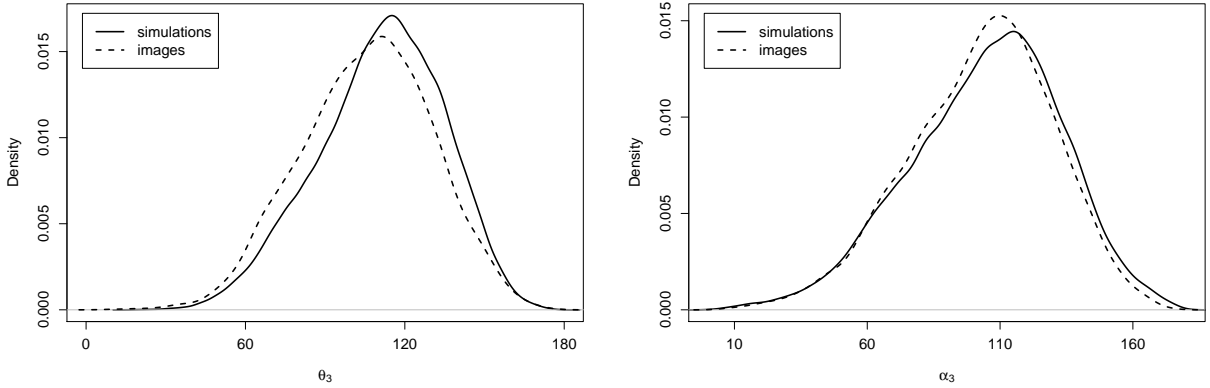


Figure 4.17: Comparison of θ_3 (left) and α_3 (right) computed analytically and estimated from the images. $V_V = 60\%$, $c = 2.0$ and gamma volume distribution.

In Figure 4.12, the distribution of the dihedral angles is presented. The distribution calculated based on the simulations is almost indistinguishable from the probability density function presented in Kumar and Kurtz (1995). The distribution estimated from images of the realizations is satisfactory. Figure 4.13 shows the interior angles. As a consequence of the discretization, these are slightly underestimated.

Now, we analogously investigate discretized Laguerre tessellations. We consider the simulations analyzed in the previous section for volume fraction 60% and coefficients of variation

0.2 and 2.0. Comparing Figure 4.14 and Figure 4.16, we see that the estimation of the number of facets per cell from the image is very good for small coefficients of variation and slightly worsens as c grows. A wider range of F_C has been observed for random polydisperse foams, in fact the maximum is 22 for $c = 0.2$ and 81 for $c = 2.0$. For the number of vertices per facet, the same as remarked for PV tessellations holds in this case, too. Figures 4.15 and 4.17 display the densities of the angles. Again, the angles are underestimated from the cell reconstruction. The goodness of the estimations does not seem to depend on the model parameters. This means that our algorithm for estimating angles from images of tessellations is not influenced by structural differences.

4.3.3 Application to closed cell foams

Now, we model the geometric structures of some samples of closed-cell polymer foams, namely, Rohacell[®] polymethacrylimide (PMI) foams. These foams are characterized by low specific weight as well as high stiffness, therefore they are broadly used as sandwich-core materials. We consider two samples to which we refer as WIND-F and RIST. The microstructures are imaged with μ CT with pixel size about $2.7\,\mu\text{m}$.

First, we will go through the main steps necessary to extract the geometric characteristics of the cells. Then, the model fitting introduced in the previous section is applied to these samples. Finally, we will exploit these datasets to investigate which characteristics mostly influence the choice of the model parameters and thus, which are sufficient for model fitting.

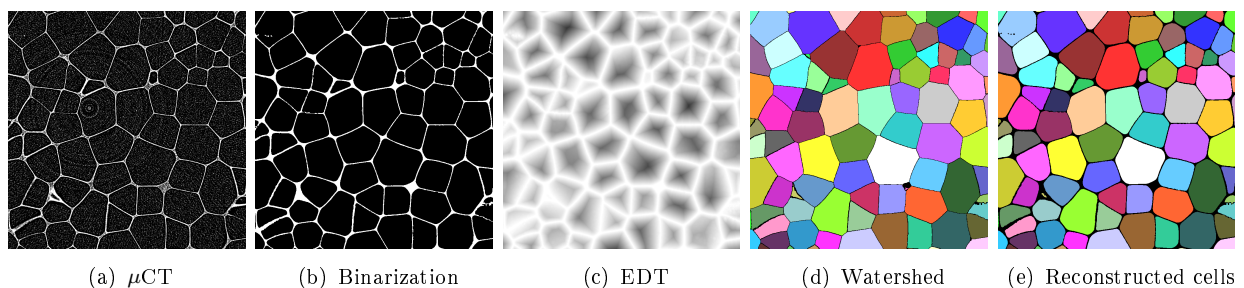


Figure 4.18: Sample WIND-F RC 100: 2d sections of the cell reconstruction steps.

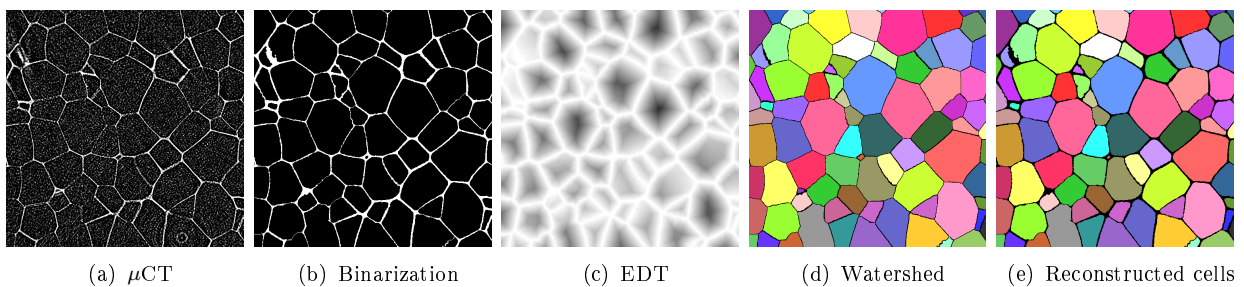


Figure 4.19: Sample RIST RC 71: 2d sections of the cell reconstruction steps.

Wall system and cell reconstruction

The first step is to binarize the wall system of a foam, i. e., the material. Due to thin structures, often threshold binarization does not suffice to correctly identify all the walls. Therefore, some smoothing and morphological closing are also applied. From the binarized wall system, we can estimate the volume fraction of the material and the structure model index.

For the model fitting, however, we also need geometric characteristics for each cell. Labeling of the pore space, even with closed-cell foams, is not enough to separate each cell. Therefore, we need more sophisticated techniques to reconstruct the cells. A well established method is based on Euclidean distance transform and watershed transform, see for instance Lautensack (2008). First, we calculate the EDT on the pore system (see Definition 2.1.4). This is inverted so that pixels with lowest values are about the centers of the cells. The idea of the watershed transform is to interpret the grey values as altitudes and let water flood from the valleys. Smoothing like preflooding or h -minima transform is necessary before applying the watershed to samples images Ohser and Schladitz (2009). A study on PMI foams showed that for these foams the parameter of the h -minima transform can be chosen automatically depending on characteristics estimated from the binarization of the wall system (Schwarz, 2012). The result is an image of labeled cells separated by one-pixel thick walls. The main steps of the cell reconstruction of our samples are shown in Figures 4.18 and 4.19.

	S	\bar{b}	F_C	θ_3	α_3		S	\bar{b}	F_C	θ_3	α_3
V	0.990	0.961	0.790	0.296	0.105	V	0.987	0.950	0.864	0.306	0.127
S		0.989	0.809	0.310	0.117	S		0.987	0.884	0.317	0.138
\bar{b}			0.808	0.320	0.128	\bar{b}			0.880	0.320	0.144
F_C				0.354	0.139	F_C				0.344	0.163
θ_3					0.110	θ_3					0.082
WIND-F RC 100						RIST					

Table 4.4: Correlation coefficients between the characteristics of the samples.

Model fitting

Once the cells are reconstructed, each cell is a compact connected body, thus the geometric characteristics can be easily estimated with the methods introduced in Section 2.1.1 and references therein. Volume, surface area and mean width are estimated on the dilated cells. In this way, the characteristics are comparable with those of the model, which is space-filling. To avoid edge effects, cells intersecting the boundaries of the observation window are excluded from the geometric analysis by minus sampling (Ohser and Schladitz, 2009). The topological numbers and angles are estimated on an image of the labeled cells with the watershed skeleton.

The observed PMI foams are stationary and isotropic. The moments of the main characteristics are summarized in Table 4.6. The distributions of dihedral and interior angles for each sample are represented in Figures 4.22, 4.23. As expected, the foams are not in

characteristics		gamma			lognormal		
WIND-F RC 100		\bar{d}_{min}	V_V	c	\bar{d}_{min}	V_V	c
0	$V, S, \bar{b}, F_C, -, -$	0.076	60	0.798	0.108	60	0.852
1	$V, S, \bar{b}, F_C, \theta_3, \alpha_3$	0.117	50	0.886	0.144	60	0.880
2	$V, S, \bar{b}, F_C, \theta_3, -$	0.100	60	0.817	0.132	60	0.872
3	$V, S, \bar{b}, F_C, -, \alpha_3$	0.107	60	0.808	0.132	60	0.860
4	$V, -, \bar{b}, F_C, \theta_3, \alpha_3$	0.129	60	0.833	0.159	60	0.874
RIST RC 71		\bar{d}_{min}	V_V	c	\bar{d}_{min}	V_V	c
0	$V, S, \bar{b}, F_C, -, -$	0.075	60	0.853	0.100	60	0.927
1	$V, S, \bar{b}, F_C, \theta_3, \alpha_3$	0.093	60	0.879	0.120	60	0.955
2	$V, S, \bar{b}, F_C, \theta_3, -$	0.101	60	0.876	0.129	60	0.951
3	$V, S, \bar{b}, F_C, -, \alpha_3$	0.070	60	0.857	0.093	60	0.931
4	$V, -, \bar{b}, F_C, \theta_3, \alpha_3$	0.101	60	0.874	0.130	60	0.940

Table 4.5: Model fitting for the samples. Values of the mean minimal distance with corresponding parameters for gamma and lognormal sphere volume distribution.

Plateau's equilibrium. In fact, the production process of solid foams does not allow the structures to reach the minimal energy Borovinšek et al. (2008). The pairwise correlations between the characteristics are shown in Table 4.4. Comparing these values with Table 4.3, one can see that they are similar to the correlations in random Laguerre tessellations.

Now, we have all the information needed for model fitting by minimizing the distance function with respect to the model parameters. The angles are alternatively removed to investigate their influence on the choice of the model. The volume is always included as its mean value is fitted by choosing the number of cells observed in a window of given volume. Note that by including a characteristic, we include mean value and standard deviation. A summary of the results is shown in Table 4.5. To allow comparison, the value of the distance is normalized according to the number of features included, so that the value of \bar{d}_{min} can be interpreted as the mean distance of the characteristics of the sample to those of the model.

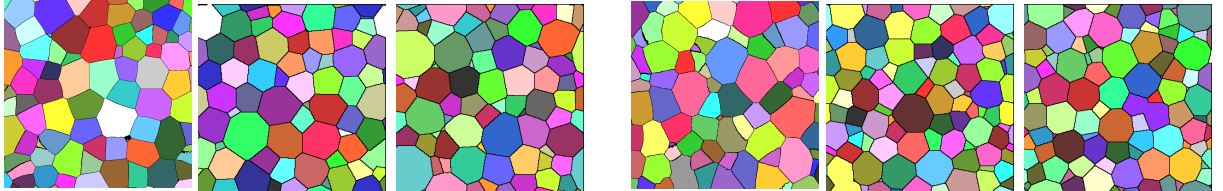


Figure 4.20: 2d sections of the samples and the corresponding fitted model 0 and model 1. WIND-F (left) and RIST (right).

In all cases, the minima are found with gamma distributed volumes. For coefficients of variation smaller than 1.0, the characteristics have similar mean values for all volume fractions, see also Redenbach (2009). This can explain some of the jumps in V_V . Both with gamma and lognormal volume distribution, including the angles induces larger mean distance. This suggests that the moments of the angles in the samples and in the model

are farther than the other features. Alternating θ_3 and α_3 we observed that one angle alone affects mostly the value of the distance, hence the choice of the model parameters. Whether it is the dihedral or the interior angle depends on the sample. For the RIST, inserting only the interior angles yields the same results as without any angle. The analysis in Lautensack (2007) showed that V , \bar{b} , and F_C alone do not suffice to determine the parameters of the best-fitting model. However, if we add the information contained in the angles, then it is possible to exclude the surface area from the model fitting without affecting the choice of the model.

We generate Laguerre tessellations with the parameters minimizing the distance function with respect to V , S , \bar{b} , and F_C (model 0) and to this quadruple and the two angles (model 1). For each sample, we realize ten models in cubes of edge length 2 mm for the PMI foams. Visualizations of the models can be seen in Figures 4.20 and 4.21. In Table 4.6, the mean values and standard deviations of the characteristics of the samples and the models are summarized. For both models, there is a good agreement with the observed characteristics. The differences between the characteristics of the two fitted models are very small. While for the sample WIND-F the moments of both angles are fitted better with model 1, for the other sample only the values of the dihedral angle improve. In Figures 4.22 and 4.23, the distributions of the angles of the samples can be compared to those of the two fitted models. The fit obtained with the angles in the model fitting improves only slightly the distribution of angles. The same result was found by analyzing two samples of open-cell foams in Vecchio et al. (2014). Therefore, we can conclude that the angles are already fitted well by minimizing the distance function with respect to the moments of the four characteristics V , S , \bar{b} , and F_C . The computational effort of computing angles in images is not necessary to improve the model fitting. Nonetheless, angles proved to validate the choice of Laguerre tessellations generated by systems of non-overlapping spheres to model rigid foams.

	\bar{V}	$\sigma(V)$	\bar{S}	$\sigma(S)$	\bar{b}	$\sigma(\bar{b})$	F_C	$\sigma(F_C)$
WIND-F	0.021	0.011	0.413	0.154	0.383	0.078	14.34	3.78
model 0	0.021	0.013	0.395	0.151	0.364	0.067	13.78	3.68
model 1	0.021	0.015	0.392	0.170	0.362	0.074	13.70	4.11
RIST	0.014	0.009	0.318	0.130	0.347	0.071	14.09	3.66
model 0	0.014	0.010	0.302	0.126	0.318	0.063	13.74	3.99
model 1	0.014	0.010	0.302	0.129	0.317	0.065	13.71	4.06
					$\bar{\theta}_3$	$\sigma(\theta_3)$	$\bar{\alpha}_3$	$\sigma(\alpha_3)$
WIND-F					116.01°	19.87°	105.11°	28.92°
model 0					117.69°	15.29°	108.84°	21.32°
model 1					116.79°	16.06°	108.60°	21.91°
RIST					115.49°	20.65°	106.99°	23.49°
model 0					116.99°	16.12°	107.95°	22.78°
model 1					116.62°	16.40°	108.46°	21.95°

Table 4.6: Characteristics of the foams and of the best-fitting models w. r. t. V , S , \bar{b} , and F_C for “model 0” and θ_3 and α_3 , too, for “model 1”. Size features in mm.

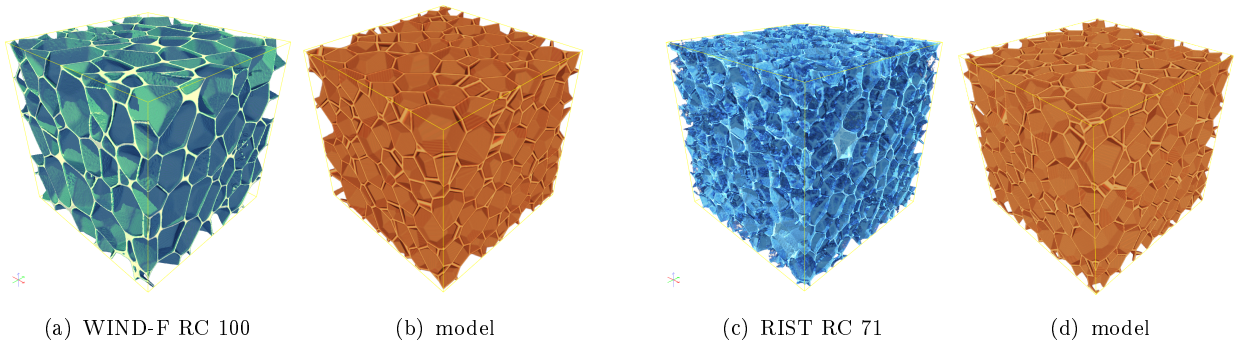


Figure 4.21: Volume renderings of the wall system of the samples of PMI foams and corresponding models fitted w.r.t. V , S , \bar{b} , and F_C . WIND-F: window size 600^3 pixels= $1630^3 \mu\text{m}^3$, model with 380 cells and periodic edge conditions. RIST: window size 600^3 pixels= $1668^3 \mu\text{m}^3$, model with 564 cells and periodic edge conditions.

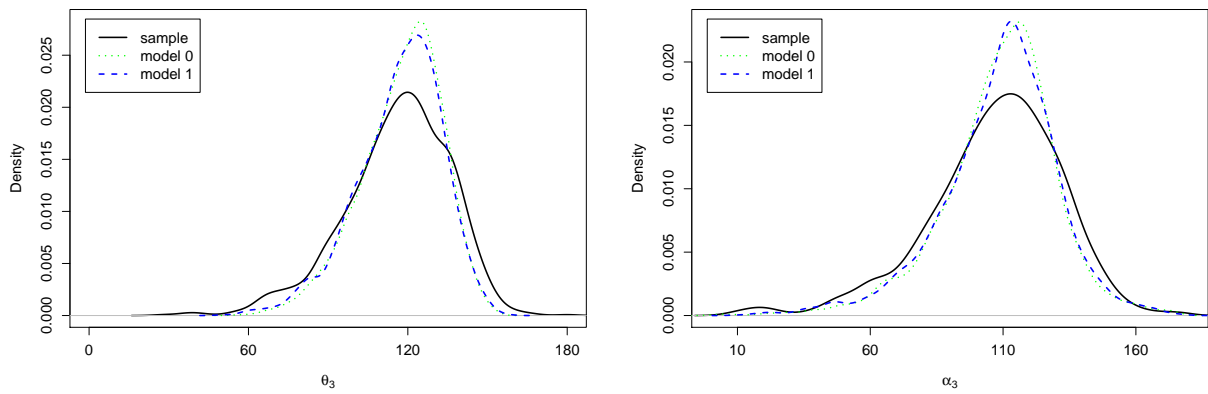


Figure 4.22: Sample WIND-F RC 100: dihedral angles (left) and interior angles (right) distribution estimated on the reconstructed cells. Comparison with the angles distribution of the fitted models.

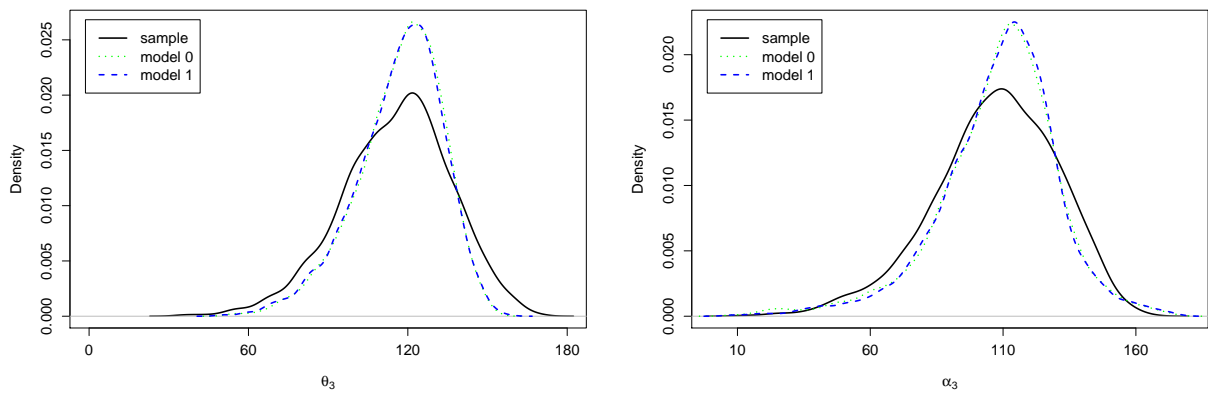


Figure 4.23: Sample RIST RC 71: dihedral angles (left) and interior angles (right) distribution estimated on the reconstructed cells. Comparison with the angles distribution of the fitted models.

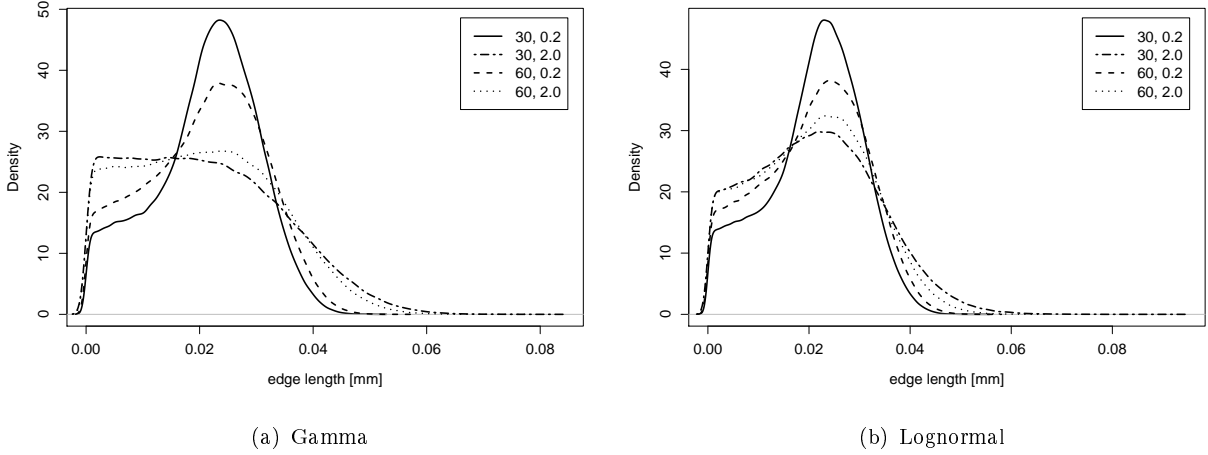


Figure 4.24: Edge length distribution in Laguerre tessellations generated by force-biased sphere packings with $V_V = 30\%, 60\%$ and $c = 0.2, 2.0$. Left: gamma volume distribution. Right: lognormal volume distribution.

4.4 Edge length distribution

A geometric characteristic that we have not regarded so far is the edge length distribution. Figure 4.24 displays the edge length of some realizations of Laguerre tessellations with varying parameters of the force-biased sphere packings. Namely, the graphics regard the same simulations as analyzed in the previous section: five realizations with 10 000 cells for each parameter set with periodic conditions in a window of 1 mm^3 . Due to the fact that a small coefficient of variation yields a more regular structure, the peak is higher in this case. However, a rather large amount of short edges occur in all the plotted curves. This yields that, by only modifying the model parameters, it is not possible to significantly improve the goodness of fit of the edge length distribution. Therefore, instead of using the moments of this distribution in the model fitting as done with the angles (Section 4.3.1), we take a different approach inspired by the rich literature on models for soap froth.

Compared to soap froth, random Laguerre tessellations show a much higher number of short edges (Kraynik et al., 2003). To model the mechanical equilibrium, Laguerre tessellations generated by dense packings of spheres are relaxed with the software Surface Evolver (Brakke, 1992). Following this approach, we investigate relaxed Laguerre tessellations fitted to samples of open and closed cell foams. Our goal is to inspect how the geometry of the models is affected by the relaxation and whether the relaxed models better fit to the samples or not.

4.4.1 Surface Evolver and relaxation

Surface Evolver is an open source software developed by Brakke (1992) to minimize the energy of a surface under constraints. It has been used in several application fields, from rheology to architecture. It is implemented in C and can be easily integrated with user

defined functions. The surfaces, i. e., two-dimensional bodies in 3d, are expressed through a simplicial representation. Each simplex on a surface is a subset of a hyperplane, therefore curvature is obtained by non-coplanar neighboring simplices.

For our scope, we follow the work of Kraynik et al. (2003), see also Jang et al. (2008); Kraynik et al. (2004). The cells of a tessellation are interpreted as thin films of liquid soap. Then, the *relaxation* process simulates the transition to dry soap froth, hence to the mechanical equilibrium in which Plateau's laws apply. Relaxation consists in several topological transitions. At each step, a short edge is shrunk to zero length, thus causing modifications in the neighbors and topology of the cells containing the edge. This is supplemented with *annealing cycles*: the foam is subjected to large homogeneous deformations on the three axes of the reference system. In this way, additional topological transitions and structure rearrangements are induced. The constraint for minimization is the cell size distribution, which is kept constant. The process is stopped when either there are no major changes in the structure after annealing, or when all the short edges have been removed. Depending on the number of cells and the meshing of the surface, the relaxation requires long computational time.

4.4.2 Analysis of solid foams

As mentioned in Section 4.2, it is basically impossible to completely physically motivate the geometry of solid foams, as there are too many parameters controlling the production process. Therefore, we study empirically the geometry of different types of foams. We consider the following samples:

- Rohacell® PMI closed cell foam (WIND-F RC100),
- Rohacell® PMI closed cell foam (RIST RC71),
- Airex® polyvinyl-chloride (PVC) closed cell foam (Airex T92-100),
- polymer open cell foam,
- aluminum open cell foam (Al),
- Duocel® copper open cell foam (Cu).

The PMI samples are those analyzed in the previous chapter. A complete analysis of the samples of aluminum foam and the open polymer foam are found in Redenbach (2009) and Vecchio et al. (2014), where also the angles are investigated. The sample of copper foam is analyzed and modeled in Liebscher et al. (2012). These three samples of open cell foams feature an anisotropy that has been corrected before further analyses. The anisotropy of the foams is detected by comparing the mean width of the cells in different directions, for instance, the 13 discrete direction induced by the lattice. Modifying the spacing of the image in order to have uniform distribution of the mean width allows to correct the anisotropy. From now on, we analyze the corrected isotropic foams.

In Table 4.7, the moments of the characteristics of the samples and the parameters of the best fitting models are summarized. Models are fitted with the procedure outlined in Section 4.3 with respect to mean value and standard deviation of V , S , \bar{b} , and N_{32} . We

recall that the topological number N_{32} can be interpreted as a measure of regularity of the foam. Compared to the PMI closed cell foams, the metal foams have a lower mean number of facets per cell. This is not surprising, in fact open foams are typically more regular. However, despite being a closed cell foam, the sample of Airex does not comply with this trend. For this sample, N_{32} is 13.3 and its standard deviation is 5.9, which is much larger than in the open foams. So, although on average it seems more regular, it contains so much variability in the cell size that the mean value alone does not suffice to describe the sample.

	\bar{V}	$\sigma(V)$	\bar{S}	$\sigma(S)$	\bar{b}	$\sigma(\bar{b})$	N_{32}	$\sigma(N_{32})$	(V_V, c)
WIND-F	0.021	0.011	0.413	0.154	0.383	0.078	14.34	3.78	(60%, 0.798)
RIST	0.021	0.013	0.395	0.151	0.364	0.067	13.78	3.68	(60%, 0.853)
Airex	0.019	0.024	0.363	0.301	0.348	0.154	13.35	5.97	(60%, 1.742)
Open poly	60.565	11.363	86.855	10.826	5.689	0.384	13.65	1.90	(30%, 0.311)
Al foam	21.437	2.855	43.720	3.859	3.807	0.171	13.83	1.21	(60%, 0.166)
Cu foam	49.234	9.591	79.777	10.285	5.083	0.322	13.91	1.48	(60%, 0.286)

Table 4.7: Characteristics of the foams and parameters of the best-fitting models. Size features in mm.

The edge length distribution in the samples is estimated with the algorithm proposed to estimate angles (Section 4.3.2). In fact, when the topology of the foam is reconstructed and the coordinates of the nodes are known, also the edge length can be easily calculated. The distributions thus obtained are shown in Figure 4.26.

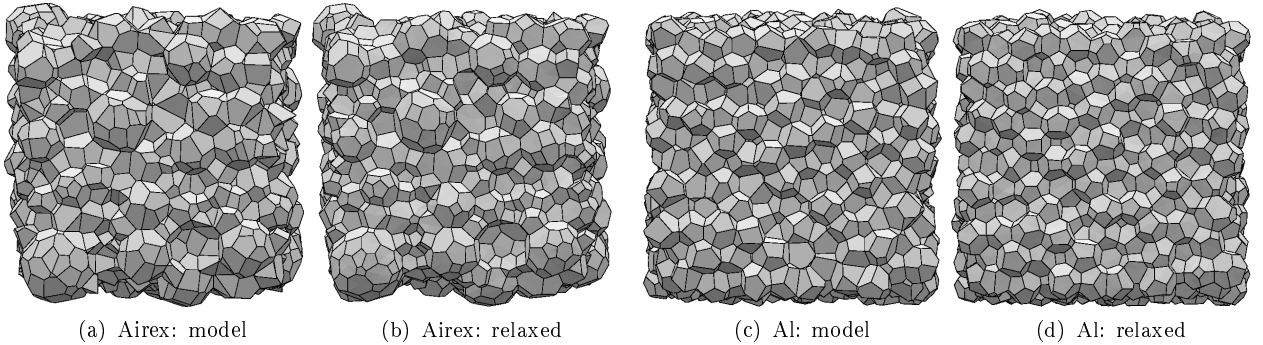


Figure 4.25: Visualizations of the models and the corresponding relaxed ones for the samples of Airex (left) and for the aluminum foam (right). Model parameters: $(V_V, c) = (60\%, 1.742)$ for Airex, $(V_V, c) = (60\%, 0.166)$ for aluminum. Visualizations with Surface Evolver.

For each sample, we generate three realizations of random Laguerre tessellations generated by a force-biased sphere packing with 1000 cells each. Each realization is relaxed with Surface Evolver. In Figure 4.25, the models and the corresponding relaxed ones for two samples are shown. The high polydispersity of the Airex sample can be easily recognized by the large cells, whereas the model for the aluminum foam is almost monodisperse. Comparing the volume rendering, one can see that the geometry of the cells is modified only locally and that overall the relaxed models look more regular. There are no short edges to be seen and the facets have fewer small angles. The Laguerre tessellation has been meshed adding one point in the center of each facet. While relaxing, the triangles in a facet change orientations

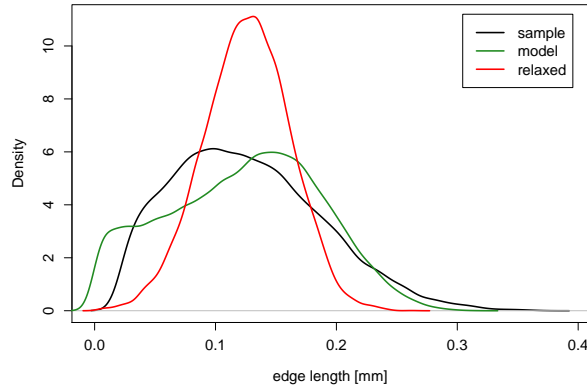
to simulate the curved surfaces typical of soap froth. We chose a rough mesh because we are mainly interested in characteristics that are independent of the curvature of the facets. In fact, we investigate edge length and topological numbers, which are also the characteristics mainly affected by the relaxation.

The edge length distribution in the samples and in the models is represented in Figure 4.26. As expected, the number of short edges in all the samples is lower than in the fitted Laguerre tessellations. In both PMI foams, however, the edge length distribution is wide and shows rather short edges that are swept off completely by the relaxation. The high peak of the edge length distribution in the relaxed models does not fit better to the sample than the original Laguerre model. There are little differences in the number of facets per cell (Figure 4.27), whereas the number of edges per facet is affected more by the relaxation (Figure 4.28). However, even in this case it does not improve the fit to the samples WIND-F and RIST.

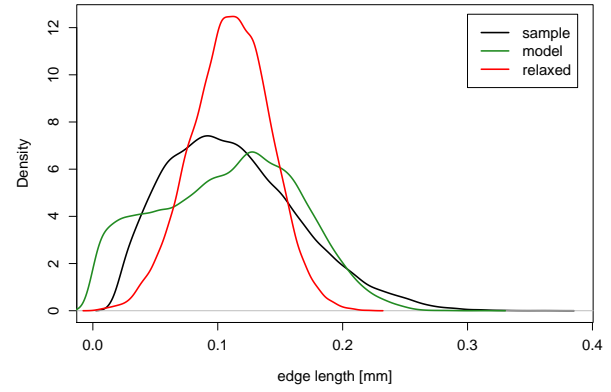
The three samples of open cell foams we considered behave similarly. The edge length distributions show high peaks and no short edges. Consequently, they are fitted much better by the relaxed models than by the Laguerre tessellations, as can be seen also in the distributions of the topological numbers. Of course, there is still a gap between the edge length distribution in the samples and in the relaxed foams. In fact, the samples are solid foams, thus they are not in Plateau's equilibrium.

The sample of Airex shows a hybrid behavior. The edge length distribution has a high peak, but the shape of the distribution is different than in the relaxed models and leans towards short edges. As this sample is highly polydisperse, also the distributions of the topological numbers are qualitatively different than in the other samples, especially the number of facets per cell. The distributions of both N_{32} and N_{20} are not much affected by the relaxation, thus it is not clear which model fits better.

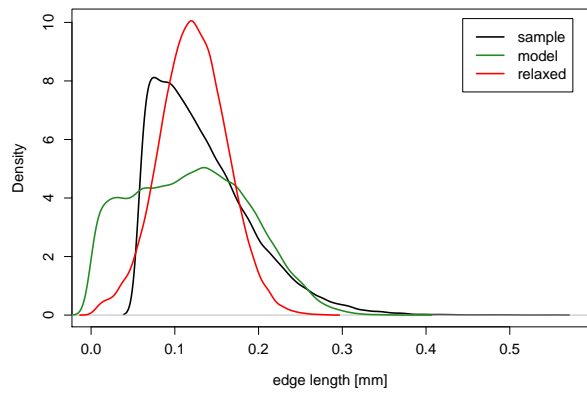
The analysis of the characteristics of the relaxed models show that the edge length distribution is at most modified by the relaxation. This yields that our model fitting procedure is still valid also for the relaxed tessellations, in fact, it is based on other characteristics. Therefore, it is possible to fit relaxed Laguerre tessellations to samples of solid foams without user interaction. In fact, one can proceed exactly as described in Section 4.3, thus finding the parameter of the best fitting random Laguerre distribution generated by a system of non-overlapping spheres. Then, insert the model in the Surface Evolver and relax it. The open question is when exactly relaxation yields a better fit. This depends mainly on the regularity of the foam. Low mean and standard deviation of the number of facets per cell usually occur in regular foams. Higher variance is typically related with higher polydispersity, i. e., a larger coefficient of variation. In these cases, the edge length distribution should not show the high peak typical of relaxed models, thus random Laguerre tessellation models are a better choice. Highly polydisperse foams are solidified rather far away from the equilibrium. Thus, we have to conclude that for these foams, it is hard to predict the distributions of the geometric characteristics and which between Laguerre tessellations and relaxed models are better models.



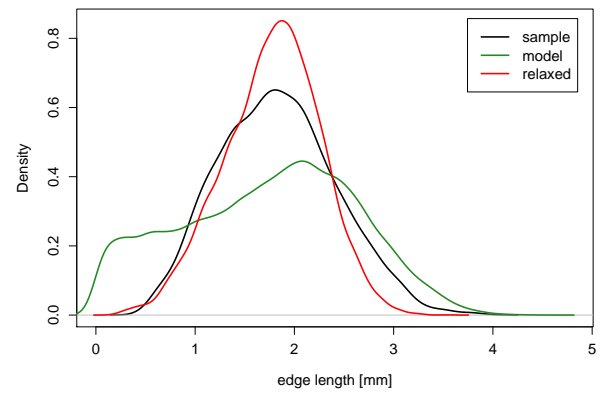
(a) WIND-F



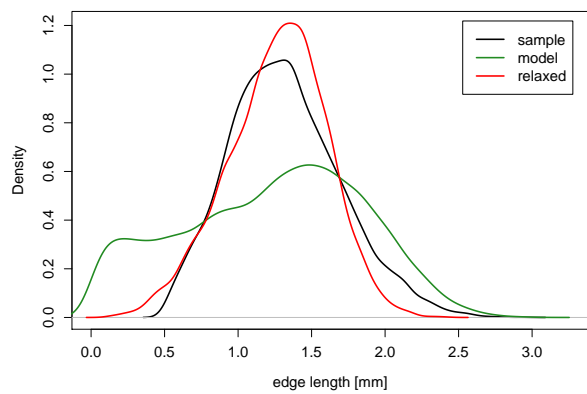
(b) RIST



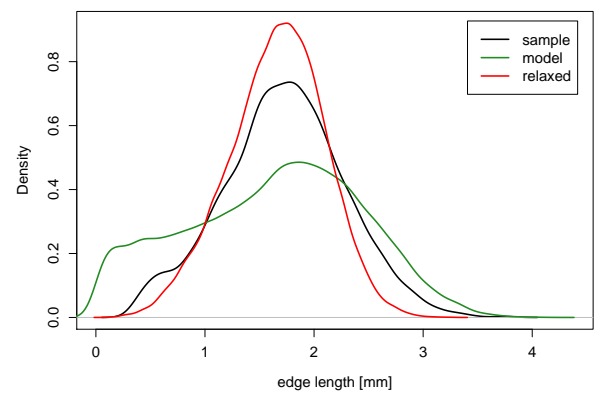
(c) Airex



(d) Open polymer

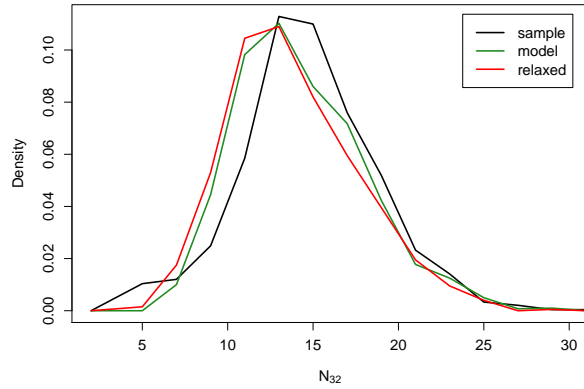


(e) Al foam

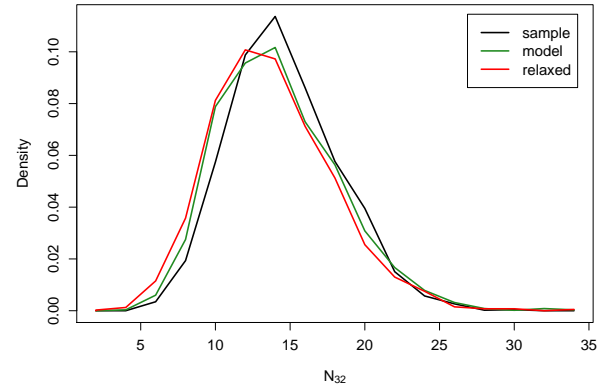


(f) Cu foam

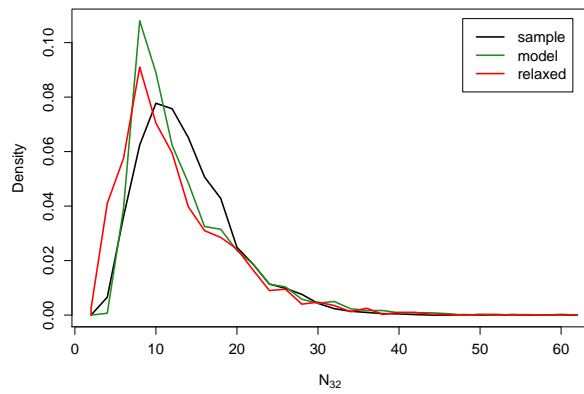
Figure 4.26: Edge length distribution estimated from the samples compared with the edge length distribution in the fitted models and in the relaxed models.



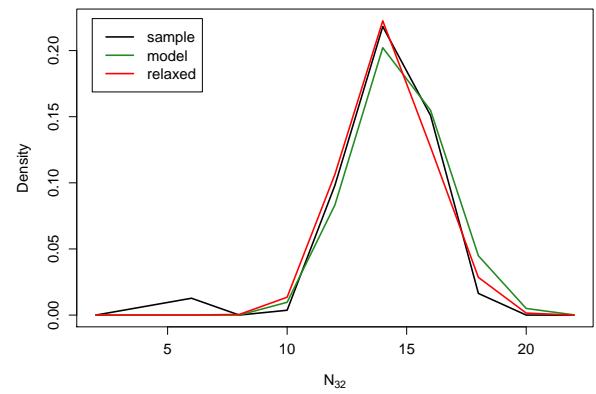
(a) WIND-F



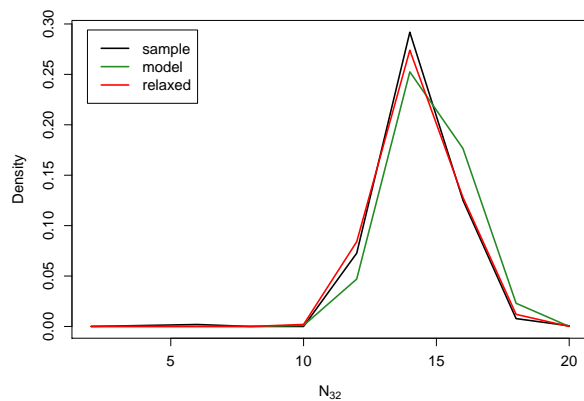
(b) RIST



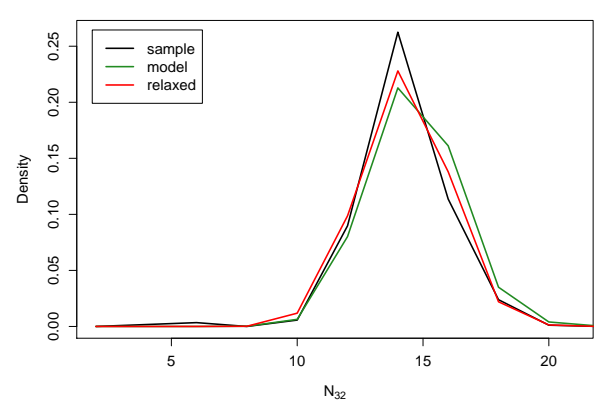
(c) Airex



(d) Open polymer

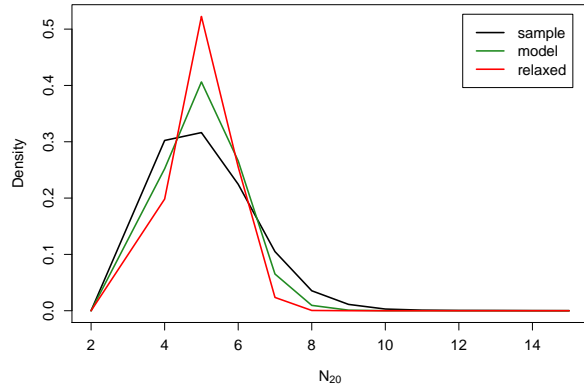


(e) Al foam

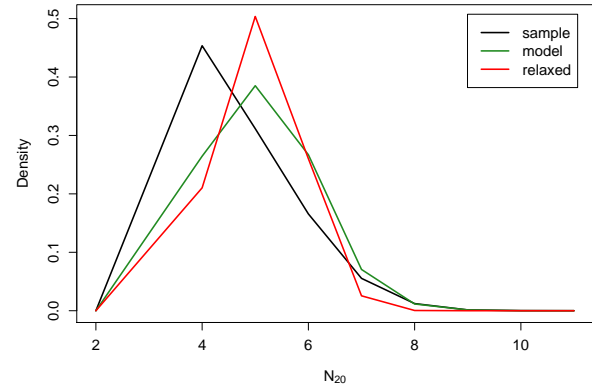


(f) Cu foam

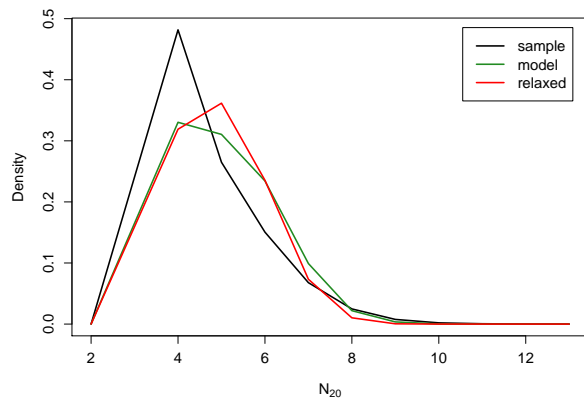
Figure 4.27: Distribution of the number of facets per cell estimated from the samples compared with the number of facets per cell in the fitted models and in the relaxed models.



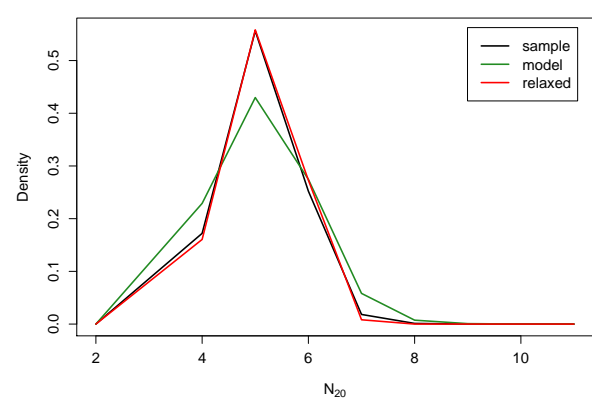
(a) WIND-F



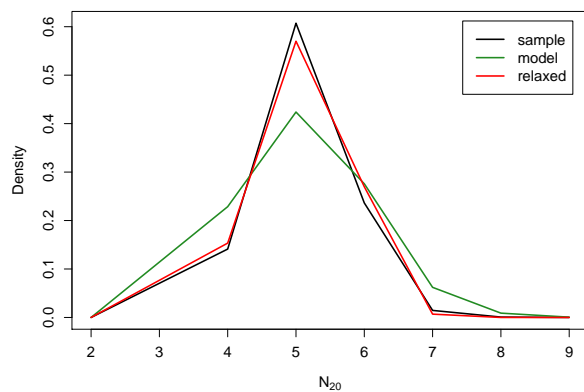
(b) RIST



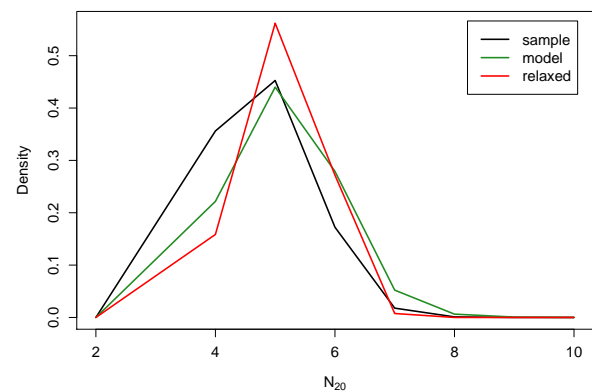
(c) Airex



(d) Open polymer



(e) Al foam



(f) Cu foam

Figure 4.28: Distribution of the number of edges per facet estimated from the samples compared with the number of edges per facet in the fitted models and in the relaxed models.

4.5 Discussion

We introduced random tessellations based on point processes. We motivated, geometrically and physically, why random Laguerre tessellations are suitable models for the pore systems of real rigid foams. The procedure for model fitting based on image data was outlined and applied on several samples. Moreover, for the first time, angles in Laguerre tessellations were investigated. Introducing an algorithm to estimate angles in images of foams, we showed that the models are able to capture the angle distributions observed in the samples.

Furthermore, a method developed for modeling soap froth was adapted to model solid foams. Combining this with the model fitting procedure optimized for Laguerre tessellations generated by force-biased sphere packings, it is possible to automatically model a sample of foam also with relaxed tessellations. Analyzing six samples of different types of foams, we showed that relaxed models fit better to open cell foams, but worse to some closed cell foams. We suggested how to relate this result to the geometric characteristics of the foams. In this context, it would be interesting to investigate how the mechanical properties of the foams are influenced by the relaxation.

Now we are able to model the geometry of the pore system, including angles and edge length distribution, the open question is how to model the material distribution on the struts and on the walls of foams. In fact, the material is not uniformly distributed around the pores. However, to analyze the material distribution of samples, even higher definition images are needed. For instance, the images of the PMI foams are taken with resolution of about $2.7\ \mu\text{m}$ and yet, walls are sometimes only one or two pixels thick.

Conclusions

The current norms for inspection of dirt particles in the context of technical cleanliness are based on the analysis of microscopic two-dimensional images. We generalized the characterization in order to be applied to three-dimensional images of particles. We defined a set of features to describe compact bodies in \mathbb{R}^3 and outlined efficient algorithms to estimate them from the digital representation of the bodies. The characterization can be easily applied to describe size and shape of any object. In fact, also in this work, we employed some of the geometric parameters to characterize the cells of foams. We showed how to exploit the features to infer a classification of particles based on the standards of technical cleanliness. This classification is based on thresholding. However, it is possible to employ the features to induce a more sophisticated classification of objects, for instance, with hierarchical methods.

Analyzing systems of fibers, we highlighted which are the main difficulties in the characterization of the structures and modeling. We illustrated how to fit Boolean models and Poisson processes of cylinders with circular and polygonal cross section starting from the intrinsic volume densities estimated from binary images of samples. Methods to estimate the orientation distribution of the fibers' cross section still need to be developed. In the overview on models with interaction, we presented models featuring non-overlapping and bent fibers. Generalizing these models to allow polygonal cross sections requires a revision of the definition of the models. This might be computationally demanding, but could significantly enhance the goodness of fit for some composite materials.

Random Laguerre tessellations are widely used to model rigid foams. However, some features have not been studied in detail before. Our analysis of dihedral and interior angles showed that these models are able to encompass the same angle distributions observed in foams. As the moments of the angles do not influence the selection of the parameters of the best fitting model, there is little room for improvement following this approach.

We addressed the well known problem of short edges in Laguerre tessellations. Inspired by models for soap froth, we adapted the same procedure to model rigid foams. While we examined the geometric characteristics of some samples, the investigation of mechanical properties is still an open question. Moreover, models for the cell systems of foams need to be supplemented by a model for the material distribution. A challenging open problem is the development of a stochastic model for the wall systems of closed cell foams.

List of symbols

\oplus	Minkowski sum
\ominus	Minkowski subtraction
$\mathbf{1}_A$	indicator function of the set A
$\overset{\circ}{A}$	interior of the set A
∂A	boundary of the set A
B_r	ball of radius r centered in the origin
$\mathcal{B} = \mathcal{B}(\mathbb{R}^d)$	Borel σ -algebra on \mathbb{R}^d
\mathcal{C}	compact subsets of \mathbb{R}^d
\mathcal{F}	closed subsets of \mathbb{R}^d
\mathcal{G}	open subsets of \mathbb{R}^d
\mathcal{H}^d	Hausdorff measure in \mathbb{R}^d
\mathcal{K}	convex subsets of \mathbb{R}^d
\mathbb{L}^d	d -dimensional point lattice
\mathbb{N}	natural numbers
\mathbb{N}_0	$\mathbb{N} \cup \{0\}$
\mathbb{R}^+	positive real numbers
\mathcal{R}	convex ring
$SO(\mathbb{R}^d) = SO_d$	rotation group of \mathbb{R}^d
\mathcal{S}	extended convex ring
V_k	k -dimensional intrinsic volume
$V_{V,k}$	k -dimensional intrinsic volume density
κ_d	volume of the d -dimensional unit ball
ν_d	Lebesgue measure in \mathbb{R}^d
ω_d	surface area of the d -dimensional unit ball

Appendix A

Coefficients for angles in random Laguerre tessellations

We report the coefficients of the polynomials fitted to the moments of dihedral and interior angles in random Laguerre tessellations depending on the parameters of the force biased sphere packing, see Section 4.3.1. See Table A.1 for gamma and Table A.2 for lognormal volume distribution.

V_V	1	x	x^2	x^3	SSE
<hr/>					
mean(θ_3)					
30	2.0969	-0.026	-0.0504	0.0184	1.3715e-05
40	2.0937	-0.008	-0.0727	0.0230	1.5643e-05
50	2.0917	0.0027	-0.0876	0.0258	6.3641e-06
60	2.0898	0.0154	-0.1073	0.0302	4.7877e-06
$\sigma(\theta_3)$					
30	0.1633	0.0530	0.0989	-0.0353	2.7916e-05
40	0.1702	0.0535	0.0948	-0.0333	4.0510e-05
50	0.1827	0.0384	0.1063	-0.0355	3.4320e-05
60	0.1876	0.0342	0.1133	-0.0371	3.4075e-05
<hr/>					
mean(α_3)					
30	1.9248	-0.0314	-0.008	0.0057	8.9077e-06
40	1.921	-0.0071	-0.0374	0.0128	7.5300e-06
50	1.9188	0.0098	-0.0615	0.0194	4.6682e-06
60	1.9205	0.0119	-0.0686	0.0197	9.4529e-07
$\sigma(\alpha_3)$					
30	0.3016	-0.0730	0.2209	-0.0651	4.1113e-05
40	0.3192	-0.0388	0.1536	-0.0432	1.2699e-05
50	0.3402	-0.0395	0.1323	-0.0358	2.0459e-05
60	0.3519	-0.0461	0.1256	-0.0326	2.3283e-06
<hr/>					

Table A.1: Coefficients of the polynomials fitted to mean values and standard deviations of the angles depending on c . Values for gamma volume distribution.

V_V	1	x	x^2	x^3	SSE
$\text{mean}(\theta_3)$					
30	2.0977	-0.0372	-0.0169	0.0079	5.4449e-06
40	2.0964	-0.0314	-0.0202	0.0077	4.2953e-06
50	2.0966	-0.0314	-0.0224	0.0081	5.4296e-06
60	2.0960	-0.0278	-0.0282	0.0094	4.7155e-06
$\sigma(\theta_3)$					
30	0.1603	0.0849	0.0140	-0.0093	8.7111e-06
40	0.1679	0.0790	0.0178	-0.0107	2.9217e-05
50	0.1784	0.0709	0.0221	-0.0115	1.2502e-05
60	0.1850	0.0658	0.0252	-0.0118	7.5025e-06
$\text{mean}(\alpha_3)$					
30	1.9208	-0.0165	-0.0127	0.0059	7.7238e-06
40	1.9222	-0.0190	-0.0085	0.0038	1.5116e-06
50	1.9214	-0.0093	-0.0216	0.0077	4.7260e-06
60	1.9231	-0.0100	-0.0230	0.0077	2.6833e-06
$\sigma(\alpha_3)$					
30	0.2943	-0.0019	0.0754	-0.0210	1.5007e-05
40	0.3087	0.01960	0.0485	-0.0156	6.3868e-05
50	0.3303	0.01050	0.0450	-0.0141	1.2254e-05
60	0.3414	0.01030	0.0340	-0.0100	3.3385e-06

Table A.2: Coefficients of the polynomials fitted to mean values and standard deviations of the angles depending on c . Values for lognormal volume distribution.

Appendix B

Curriculum Vitae

- 12/2010 - 07/2014 PhD Student in Mathematics
Fraunhofer ITWM, Image Processing, Kaiserslautern, Germany
Technische Universität Kaiserslautern, Kaiserslautern, Germany
- 11/2009 - 11/2010 ProSAT (Project Study in Advanced Technology)
Fraunhofer ITWM, Image Processing, Kaiserslautern, Germany
Technische Universität Kaiserslautern, Kaiserslautern, Germany
- 09/2007 - 10/2009 M.Sc. in Applied Mathematics
Università degli Studi di Milano, Italy
- 09/2004 - 10/2007 B.Sc. in Applied Mathematics
Università degli Studi di Milano, Italy
- 09/1999 – 06/2004 Diploma Liceo Scientifico Galileo Galilei, Erba, Italy

Lebenslauf

- 12/2010 - 07/2014 PhD im Fach Mathematik
Fraunhofer ITWM, Bildverarbeitung, Kaiserslautern, Germany
Technische Universität Kaiserslautern, Kaiserslautern, Germany
- 11/2009 - 11/2010 ProSAT (Project Study in Advanced Technology)
Fraunhofer ITWM, Bildverarbeitung, Kaiserslautern, Germany
Technische Universität Kaiserslautern, Kaiserslautern, Germany
- 09/2007 - 10/2009 M.Sc. in Angewandte Mathematik
Università degli Studi di Milano, Italien
- 09/2004 - 10/2007 B.Sc. in Angewandte Mathematik
Università degli Studi di Milano, Italien
- 09/1999 – 06/2004 Abitur Liceo Scientifico Galileo Galilei, Erba, Italien

Bibliography

- Hellen Altendorf. *3D Morphological Analysis and Modeling of Random Fiber Networks*. PhD thesis, École Nationale Supérieure des Mines de Paris, Technische Universität Kaiserslautern, 2011.
- Hellen Altendorf and Dominique Jeulin. 3D directional mathematical morphology for analysis of fiber orientations. *Image Analysis & Stereology*, 28(3), 2011a.
- Hellen Altendorf and Dominique Jeulin. *Stochastic Modeling of a Glass Fiber Reinforced Polymer*, volume 6671 of *Lecture Notes in Computer Science*. Springer Berlin Heidelberg, 2011b.
- Hellen Altendorf and Dominique Jeulin. Random-walk-based stochastic modeling of three-dimensional fiber systems. *Phys. Rev. E*, 83, Apr 2011c.
- Ignacio Arganda-Carreras, Rodrigo Fernández-González, Arrate Muñoz Barrutia, and Carlos Ortiz-De-Solorzano. 3D reconstruction of histological sections: Application to mammary gland tissue. *Microscopy Research and Technique*, 73(11):1019–1029, 2010.
- ASTM D4791. Standard test method for flat particles, elongated particles, or flat and elongated particles in coarse aggregate, 2010.
- ASTM F1877. Standard practice for characterization of particles, 2003.
- A. Banerjee, I. S. Dhillon, J. Ghosh, and S. Sra. Clustering on the unit hypersphere using von Mises-Fisher distributions. *Journal of Machine Learning Research*, 6:1345–1382, Sep 2005.
- Gill Barequet and Sarel Har-Peled. Efficiently approximating the minimum-volume bounding box of a point set in three dimensions. *J. Algorithm*, 38:82–91, 2001. ISSN 0196-6774.
- Alexander Bezrukov, Monika Bargieł, and Dietrich Stoyan. Statistical analysis of simulated random packings of spheres. *Particle & Particle Systems Characterization*, 19(2):111–118, 2002.
- M. Borovinšek, M. Vesenjāk, M. Jože, and Z. Ren. Computational reconstruction of scanned aluminum foams for virtual testing. *Journal of the Serbian Society for Computational Mechanics*, 2(2):16–28, 2008.
- K. A. Brakke. The surface evolver. *Experimental Mathematics*, 1(2):141–165, 1992.

- D. Coelho, J.-F. Thovert, and P. M. Adler. Geometrical and transport properties of random packings of spheres and aspherical particles. *Phys. Rev. E*, 55:1959–1978, Feb 1997.
- M. de Berg, O. Cheong, M. van Kreveld, and M. Overmars. *Computational Geometry: Algorithms and Application*. Springer, 2008.
- Robert Ehrlich and Bernhard Weinberg. An exact method for characterization of grain shape. *Journal of Sedimentary Research*, 40(1):205–212, 1970.
- A. Elsner, A. Wagner, T. Aste, H. Hermann, and D. Stoyan. Specific surface area and volume fraction of the cherry-pit model with packed pits. *The Journal of Physical Chemistry B*, 113(22):7780–7784, 2009. doi: 10.1021/jp806767m.
- M. Faessel, C. Delisée, F. Bos, and P. Castéra. 3D modelling of random cellulosic fibrous networks based on x-ray tomography and image analysis. *Composites Science and Technology*, 65(13):1931–1940, 2005. ISSN 0266-3538.
- Z. Fan, Y. Wu, X. Zhao, and Y. Lu. Simulation of polycrystalline structure with Voronoi diagram in Laguerre geometry based on random closed packing of spheres. *Computational Materials Science*, 29:301–308, 2004.
- Jens Feder. Random sequential adsorption. *Journal of Theoretical Biology*, 87(2):237–254, 1980. ISSN 0022-5193.
- N. I. Fisher, T. Lewis, and B.J.J. Embleton. *Statistical analysis of spherical data*. Cambridge University Press, 1987.
- Fraunhofer ITWM, Department of Image Processing. MAVI – modular algorithms for volume images. <http://www.mavi-3d.de>, 2005.
- Fraunhofer ITWM, Department of Image Processing. MAVIparticle – modular algorithms for volume images – particle analysis. <http://www.mavi-3d.de>, 2012.
- H. Freeman and R. Shapira. Determining the minimum-area encasing rectangle for an arbitrary closed curve. *Commun. ACM*, 18:409–413, July 1975. ISSN 0001-0782.
- Gerd Gaiselmann, Dieter Froning, Christian Tötze, Christian Quick, Ingo Manke, Werner Lehnert, and Volker Schmidt. Stochastic 3D modeling of non-woven materials with wet-proofing agent. *International Journal of Hydrogen Energy*, 38(20), 2013.
- Einar L. Hinrichsen, Jens Feder, and Torstein Jøssang. Geometry of random sequential adsorption. *Journal of Statistical Physics*, 44(5-6):793–827, 1986. ISSN 0022-4715.
- Lars M. Hoffmann. Intersection densities of nonstationary Poisson processes of hypersurfaces. *Advances in Applied Probability*, 39(2):pp. 307–317, 2007a.
- Lars M. Hoffmann. On weak stationarity and weak isotropy of processes of convex bodies and cylinders. *Advances in Applied Probability*, 39(4):pp. 864–882, 2007b.
- K. Huebner, S. Ruthotto, and D. Kragic. Minimum volume bounding box decomposition for shape approximation in robot grasping. In *IEEE International Conference on Robotics and Automation*, pages 1628 –1633, May 2008.

- ISO 16232. Road vehicles – Cleanliness of components of fluid circuits, 2007.
- Wen-Yea Jang, Andrew M. Kraynik, and Stelios Kyriakides. On the microstructure of open-cell foams and its effect on elastic properties. *International Journal of Solids and Structures*, 45(7–8):1845–1875, 2008.
- Dominique Jeulin. Modelling random media. *Image Analysis & Stereology*, 21(4), 2011.
- S. Kaminski, D. Kaminska, and J. Trzcinski. Grain size and three-dimensional particle shape - automatic analysis with application of optical electronic awk 3d analyzer. In *11th Baltic Sea Geotechnical Conference*, Gdansk, Poland, September 2008.
- S. Kanaun and O. Tkachenko. Mechanical properties of open cell foams: Simulations by Laguerre tessellation procedure. *International Journal of Fracture*, 140(1-4):305–312, 2006.
- E. Karaca, N. Kahraman, S. Omeroglu, and B. Becerir. Effects of fiber cross sectional shape and weave pattern on thermal comfort properties of polyester woven fabrics. *Fibres & Textiles in Eastern Europe*, 92(3):67–72, 2012.
- T. Köpplmayr, I. Milosavljevic, M. Aigner, R. Hasslacher, B. Plank, D. Salaberger, and J. Miethlinger. Influence of fiber orientation and length distribution on the rheological characterization of glass-fiber-filled polypropylene. *Polymer Testing*, 32(3):535–544, 2013.
- Andrew M. Kraynik, Douglas A. Reinelt, and Frank van Swol. Structure of random monodisperse foam. *Physical Review E*, 67(3), 2003.
- Andrew M. Kraynik, Douglas A. Reinelt, and Frank van Swol. Structure of random foam. *Physical Review Letters*, 93, Nov 2004.
- S. Kumar and S.K. Kurtz. Monte-Carlo study of angular and edge length distributions in a three-dimensional Poisson-Voronoi tessellation. *Materials Characterization*, 34(1):15–27, 1995.
- Michael E. Landry, Cheryl R. Blanchard, Jay D. Mabrey, Xiaodu Wang, and C. Mauli Agrawal. Morphology of in vitro generated ultrahigh molecular weight polyethylene wear particles as a function of contact conditions and material parameters. *Journal of Biomedical Materials Research*, 48(1):61–69, 1999.
- C. Lantuéjoul and F. Maisonneuve. Geodesic methods in quantitative image analysis. *Pattern Recognition*, 17(2):177 – 187, 1984.
- C. Lautensack. *Random Laguerre Tessellations*. PhD thesis, Universität Karlsruhe, Weiler bei Bingen, 2007.
- C. Lautensack and S. Zuyev. Random Laguerre tessellations. *Advances in Applied Probability*, 40(3):630–650, 2008.
- Claudia Lautensack. Fitting three-dimensional Laguerre tessellations to foam structures. *Journal of Applied Statistics*, 35(9):985–995, 2008.

- Sergiy Lavrykov, Stefan B Lindström, K. M. Singh, and Bandaru Ramarao. 3d network simulations of paper structure with fines and fillers. *Nordic Pulp and Paper Research Journal*, 27(2):256–263, 2012.
- A. Liebscher, C. Proppe, C. Redenbach, and D. Schwarzer. Uncertainty quantification for metal foam structures by means of image analysis. *Probabilistic Engineering Mechanics*, 28:143–151, 2012.
- C.L. Lin and J.D. Miller. 3D characterization and analysis of particle shape using x-ray microtomography (XMT). *Powder Technology*, 154(1):61–69, 2005.
- Daniel N. Livsey, Alexander R. Simms, Warren G. Clary, Julia S. Wellner, John B. Anderson, and John P. Chandler. Fourier grain-shape analysis of antarctic marine core: The relative influence of provenance and glacial activity on grain shape. *Journal of Sedimentary Research*, 83(1):80–90, 2013.
- U. Lorz and U. Hahn. Geometric characteristics of spatial Voronoi tessellations and planar sections. Technical Report 93-05, Fachbereich Mathematik, TU Bergakademie Freiberg, 1993.
- J. Lux, C. Delisée, and X. Thibault. 3d characterization of wood based fibrous materials: an application. *Image Analysis & Stereology*, 25(1):25–35, 2006.
- George Matheron. *Random Sets and Integral Geometry*. Wiley, New York, 1975.
- Edwin B. Matzke. The three-dimensional shape of bubbles in foam – An analysis of the role of surface forces in three-dimensional cell shape determination. *American Journal of Botany*, 33(1):58–80, 1946.
- Calvin R. Maurer, Jr., Rensheng Qi, and Vijay Raghavan. A linear time algorithm for computing exact Euclidean distance transforms of binary images in arbitrary dimensions. *IEEE Trans. Pattern Anal. Mach. Intell.*, 25(2):265–270, Feb 2003.
- Rayner M. Mayer. *Design with reinforced plastics: A Guide for Engineers and Designers*. Springer, 1993.
- Paul Meakin and Remi Jullien. Random sequential adsorption of spheres of different sizes. *Physica A: Statistical Mechanics and its Applications*, 187(3–4):475–488, 1992.
- J. Mecke. Parametric representation of mean values for stationary random mosaics. *Math. Operationsforsch. Stat., Ser. Stat.*, 15:437–442, 1984.
- L. A. Merson-Davies and F. C. Odds. A morphology index for characterization of cell shape in candida albicans. *Journal of General Microbiology*, 135(11):3143–3152, 1989.
- R. E. Miles. Estimating aggregate and overall characteristics from thick sections by transmission microscopy. *Journal of Microscopy*, 107(3):227–233, 1976.
- Jesper Møller. Random Johnson–Mehl tessellations. *Advances in Applied Probability*, 24(4):814–844, 1992.

- Raul S. Montero and Ernesto Bribiesca. State of the art of compactness and circularity measures. *International Mathematical Forum*, 4(25–28):1305–1335, 2009. ISSN 1312–7594.
- J. Mościński, M. Bargieł, Z. A. Rycerz, and P. W. M. Jacobs. The force-biased algorithm for the irregular close packing of equal hard spheres. *Molecular Simulation*, 3(4):201–212, 1989.
- W. Nagel. Orientation-dependent chord length distributions characterize convex polygons. *Journal of Applied Probability*, 30(3):730–736, 1993. ISSN 00219002.
- J. Ohser and F. Mücklich. *Statistical Analysis of Microstructures in Materials Science*. Wiley, Chichester, New York, 2000.
- J. Ohser and K. Schladitz. *3d Images of Materials Structures – Processing and Analysis*. Wiley VCH, Weinheim, 2009.
- J. Ohser, W. Nagel, and K. Schladitz. The Euler number of discretized sets – on the choice of adjacency in homogeneous lattices. In K. R. Mecke and D. Stoyan, editors, *Morphology of Condensed Matter*, volume 600 of *LNP*, pages 275–298, Berlin, 2002. Springer.
- J. Ohser, W. Nagel, and K. Schladitz. Miles formulae for Boolean models observed on lattices. *Image Analysis & Stereology*, 28(2):77–92, 2009a.
- J. Ohser, C. Redenbach, and K. Schladitz. Mesh free estimation of the structure model index. *Image Analysis & Stereology*, 28(3):179–186, 2009b.
- Joachim Ohser, Konrad Sandau, Jürgen Kampf, Irene Vecchio, and Ali Moghiseh. Improved estimation of fiber length from 3-dimensional images. *Image Analysis & Stereology*, 32(1), 2013.
- Atsuyuki Okabe, Barry Boots, Kokichi Sugihara, and Sung Nok Chiu. *Spatial tessellations: Concepts and applications of Voronoi diagrams*. Probability and Statistics. Wiley, NYC, 2nd edition, 2000.
- Kenji Okazaki and Hans Conrad. Grain size distribution in recrystallized alpha-titanium. *Transactions of the Japan Institute of Metals*, 13(3):198–204, 1972.
- Joseph O’Rourke. Finding minimal enclosing boxes. *International Journal of Parallel Programming*, 14:183–199, 1985. ISSN 0885-7458.
- Estelle Parra-Denis, Cecile Barat, Dominique Jeulin, and Christophe Ducottet. 3D complex shape characterization by statistical analysis: Application to aluminium alloys. *Materials Characterization*, 59(3):338 – 343, 2008. ISSN 1044-5803.
- C. Petres, Y. Pailhas, Y. Petillot, and D. Lane. Underwater path planing using fast marching algorithms. In *Oceans 2005 – Europe*, volume 2, pages 814–819, June 2005.
- Charles Peyrega. *Prédiction des Propriétés Acoustiques de matériaux fibreux hétérogènes à partir de leur microstructure 3D*. PhD thesis, École Nationale Supérieure des Mines de Paris, 2010.

- Charles Peyrega and Dominique Jeulin. Estimation of tortuosity and reconstruction of geodesic paths in 3D. *Image Analysis & Stereology*, 32(1), 2013.
- Joseph Plateau. *Statique expérimentale et théorique des liquides soumis aux seules forces moléculaires*. Gauthier-Villars, Paris, 1873.
- N. Provatas, M. Haataja, J. Asikainen, S. Majaniemi, M. Alava, and T. Ala-Nissila. Fiber deposition models in two and three spatial dimensions. *Colloids and Surfaces A: Physicochemical and Engineering Aspects*, 165(3):209–229, 2000.
- C. Redenbach and I. Vecchio. Statistical analysis and stochastic modelling of fibre composites. *Composites Science and Technology*, 71:107–112, 2011.
- C. Redenbach, A. Rack, K. Schladitz, O. Wirjadi, and M. Godehardt. Beyond imaging: on the quantitative analysis of tomographic volume data. *International Journal of Materials Research*, 103(2):217–227, 2012a.
- C. Redenbach, I. Shklyar, and H. Andrä. Laguerre tessellations for elastic stiffness simulations of closed foams with strongly varying cell sizes. *International Journal of Engineering Science*, 50:70–78, 2012b.
- Claudia Redenbach. Microstructure models for cellular materials. *Computational Materials Science*, 44(4):1397–1407, 2009.
- F. N. Rhines and B. R. Patterson. Effect of the degree of prior cold work on the grain volume distribution and the rate of grain growth of recrystallized aluminum. *Metallurgical Transactions A*, 13A, 1982.
- P.A. Rikvold and G. Stell. Porosity and specific surface for interpenetrable-sphere models of two-phase random media. *Journal Name: J. Chem. Phys.*, Jan 1985.
- Katharina Robb, Oliver Wirjadi, and Katja Schladitz. Fiber orientation estimation from 3D image data: Practical algorithms, visualization, and interpretation. In *HIS*, pages 320–325, 2007.
- P.K. Saha and B.B. Chaudhuri. 3D digital topology under binary transformation with applications. *Computer Vision and Image Understanding*, 63(3):418 – 429, 1996.
- JC Santamarina and GC Cho. Soil behaviour: The role of particle shape. *Advances in geotechnical engineering: The skempton conference*, 1:604–617, 2004.
- Laurent Savary, Dominique Jeulin, and Alain Thorel. Morphological analysis of carbon-polymer composite materials from thick sections. *Acta Stereologica (Slovenia)*, 18(3): 297–303, 1999.
- K. Schladitz, S. Peters, D. Reinelt-Bitzer, A. Wiegmann, and J. Ohser. Design of acoustic trim based on geometric modeling and flow simulation for non-woven. *Computational Materials Science*, 38:56–66, 2006.
- R. Schneider and W. Weil. *Stochastic and Integral Geometry*. Probability and Its Applications. Springer, Heidelberg, 2008.

- Rolf Schneider. *Convex Bodies: The Brunn-Minkowski Theory*. Encyclopedia of Mathematics and its Applications. Cambridge University Press, 1993. ISBN 9780521352208.
- Gaby Schwarz. Automatische bildanalytische Zellrekonstruktion für PMI-Hartschäume. Master's thesis, Technische Universität Kaiserslautern, 2012.
- J. Serra. *Introduction à la Morphologie Mathématique*. Cahiers du Centre de Morphologie Mathématique, Booklet No. 3, E.N.S.M.P., Fontainebleau, 1969.
- Pierre Soille. *Morphological image analysis: principles and applications*. Springer, 1999.
- Malte Spiess and Evgeny Spodarev. Anisotropic Poisson processes of cylinders. *Methodology and Computing in Applied Probability*, pages 1–19, September 2010. ISSN 1387-5841.
- Evgeny Spodarev. Cauchy-kubota-type integral formulae for the generalized cosine transforms. *Journal of Contemporary Mathematical Analysis*, 37(1):52–69, February 2002.
- D. Stoyan and H. Stoyan. *Fractals, Random Shapes and Point Fields*. Wiley, 1994.
- D. Stoyan, W. S. Kendall, and J. Mecke. *Stochastic Geometry and Its Applications*. Wiley, Chichester, second edition, 1995.
- T. Stückerath, G. Völker, and J. Meng. Classification of shape and underwater motion properties of rock. In *Third Chinese – German joint symposium on coastal and ocean engineering*, Tainan, China, November 2006.
- Kokichi Sugihara. Three-dimensional convex hull as a fruitful source of diagrams. *Theoretical Computer Science*, 235(2):325–337, 2000.
- I. Vecchio, K. Schladitz, and C. Redenbach. Laguerre tessellations: fitting a model to rigid closed-cell polymer foams. In *Proceedings Cellular Materials*, Dresden, 2012a. Deutsche Gesellschaft für Materialkunde.
- Irene Vecchio, Katja Schladitz, Michael Godehardt, and Markus Heneka. 3D geometric characterization of particles applied to technical cleanliness. *Image Analysis & Stereology*, 31(3), 2012b.
- Irene Vecchio, Katja Schladitz, and Claudia Redenbach. Fitting Laguerre tessellations to the microstructure of cellular materials. In *1st International Conference on 3D Materials Science*, pages 153–158. John Wiley & Sons, Inc., 2012c. ISBN 9781118686768.
- Irene Vecchio, Claudia Redenbach, and Katja Schladitz. Angles in Laguerre tessellation models for solid foams. *Computational Materials Science*, 83:171–184, 2014. ISSN 0927-0256.
- A. Velichko, C. Holzapfel, A. Siefers, K. Schladitz, and F. Mücklich. Unambiguous classification of complex microstructures by their three-dimensional parameters applied to graphite in cast iron. *Acta Materialia*, 56(9):1981 – 1990, 2008.
- Marjorie J. Vold. The sediment volume in dilute dispersions of spherical particles. *The Journal of Physical Chemistry*, 64(11):1616–1619, 1960.

- D. Weaire and R. Phelan. A counter-example to Kelvin's conjecture on minimal surfaces. *Philosophical Magazine Letters*, 69(2):107–110, 1994.
- Denis Weaire. *The Kelvin Problem: Foam structures of minimal surface area*. Taylor and Francis, London, 1996.
- Denis Weaire and Stefan Hutzler. *The Physics of Foams*. Oxford University Press, Oxford, 1999.
- Wolfgang Weil. Point processes of cylinders, particles and flats. *Acta Applicandae Mathematicae*, 9:103–136, 1987. ISSN 0167-8019.
- Wolfgang Weil. Densities of mixed volumes for Boolean models. *Advances in Applied Probability*, 33(1):pp. 39–60, 2001.
- T. Wejrzanowski, J. Skibinski, J. Szumbariski, and K.J. Kurzydowski. Structure of foams modeled by Laguerre–Voronoi tessellations. *Computational Materials Science*, 67(0):216–221, 2013.
- O. Wirjadi, K. Schladitz, A. Rack, and T. Breuel. Applications of anisotropic image filters for computing 2D and 3D-fiber orientations. In *European Congress of Stereology and Image Analysis*, North America, 2008.
- Na Zhang. *Fibre Processes and their Applications*. PhD thesis, Technische Universität Kaiserslautern, 2013.
- Theodor Zingg. *Beitrag zur Schotteranalyse*. PhD thesis, ETH Zürich, 1935.